PHOTOPHYSICS AND SKIN PENETRATION OF ACTIVE AGENTS IN A COMMERCIAL SUNSCREEN AND INSECT REPELLENT

by

DONALD PRETTYPAUL

A Dissertation submitted to the

Graduate School-Newark

Rutgers, The State University of New Jersey

In partial fulfillment of the requirements

for the degree of

Doctor of Philosophy

Graduate Program in Chemistry

written under the direction of

Professor Richard Mendelsohn

Professor Piotr Piotrowiak

and approved by

_____

_____

_____

_____

_____

Newark, New Jersey

October 2018

ABSTRACT OF DISSERTATION

PHOTOPHYSICS AND SKIN PENETRATION OF ACTIVE AGENTS IN A COMMERCIAL SUNSCREEN AND INSECT REPELLENT

By DONALD PRETTYPAUL

Dissertation co-Directors:
Professor Richard Mendelsohn
Professor Piotr Piotrowiak

This dissertation is focused on active agents in commercial sunscreen and insect repellent products. It consists of two parts, the first focusing on the photophysics of a sunscreen active agent and the second on the permeation and spatial distribution of the sunscreen active and an insect repellent active when these agents are applied to ex-vivo human skin.

In the photochemistry study, ultrafast spectroscopy was used to study the excited state dynamics of the sunscreen molecule, Bemotrizinol. The work focused on the dissipation rates of the electronic excitation energy in different solvents. To complement the results from time-resolved femtosecond spectroscopy, Hartree-Fock UH/UHF 6-31G* calculations were used to characterize the ground and excited states potential energy surfaces. The results indicate that the excited state deactivation pathway follows a proton coupled electron transfer process which

proceeds via a concerted mechanism. The dependencies on solvent polarity, viscosity, and H/D isotope effects, were investigated.

Sunscreen products have been developed to protect skin from ultraviolet (UV) radiation; to achieve adequate protection, the sunscreen must be evenly applied and remain on the surface of the skin. However, skin itself presents a major challenge for application of a uniform film because of its undulating surface. Due to these inherent contours, sunscreen filters may not be distributed evenly during application. Confocal Raman microscopy was utilized to investigate the film properties of a sunscreen formulation when applied to ex-vivo human skin. The results indicate that the presence of a film-forming polymer causes the sunscreen active, Bemotrizinol, to be distributed more homogeneously and to temporally persist on the skin surface.

DEET is the most efficacious and widely-used active ingredient formulated into insect repellent. Confocal Raman microscopy was used to investigate the effect of polymers on the spatial distribution and permeation of DEET following its application to ex-vivo human skin. The results confirm that DEET permeates into the skin; furthermore, it is demonstrated that polymers do affect the permeation process in a variety of potentially important ways.

Acknowledgements

I am extremely thankful to Professor Richard Mendelsohn and Professor Piotr Piotrowiak for providing me the opportunity to pursue my Ph.D. study. My success was only possible because of their understanding, support and guidance.

To my committee members, Prof. Huskey, Prof. Lalancette and Prof. Michniak-Kohn; I am fortunate to have you on my committee and thankful for the time spent reviewing my thesis.

I would like to thank Dr. Carol Flach for her support, guidance and her time spent reading and correcting my thesis.

I am also thankful to former group members especially Qihong Zhang and Jianhua Bao for their help and support.

I would like to thank Ashland's leaders, especially Linda Foltis and Hani Fares, for their constant support and encouragement. Many thanks to my colleagues Ritamarie Guerrero, Diane Kennedy, Larry Senak and Roger McMullen for their advice and encouragement.

I would like to thank my family for their support and encouragement, especially my father for his guidance and wisdom.

Most importantly, I would like to dedicate this thesis to my wife Trena, our son Shaun and our daughter Aryanna for their constant love, understanding, and support. I am truly grateful to all of you.

Table of Contents

Lists of Tables

List of Illustrations

Chapter 1 Introduction

1.1 Function and Structure of the Skin

Skin, the outermost layer of the human body forms a protective barrier between the body and the environment. As such its principal functions are (1) to protect the body by preventing pathogens and exogenous substances from entering the body and (2) to regulate water loss from the body[1]. In addition, the skin also maintains the body's core temperature by exchanging heat with the environment[2]. Another essential function of the skin is to detect sensations such as heat, cold, pressure and pain through a complex network of nerves[3]. Morphologically, the skin, Figure 1-1, is a complex structure consisting of three main components, the epidermis, dermis and the hypodermis, also known as the subcutaneous tissue.

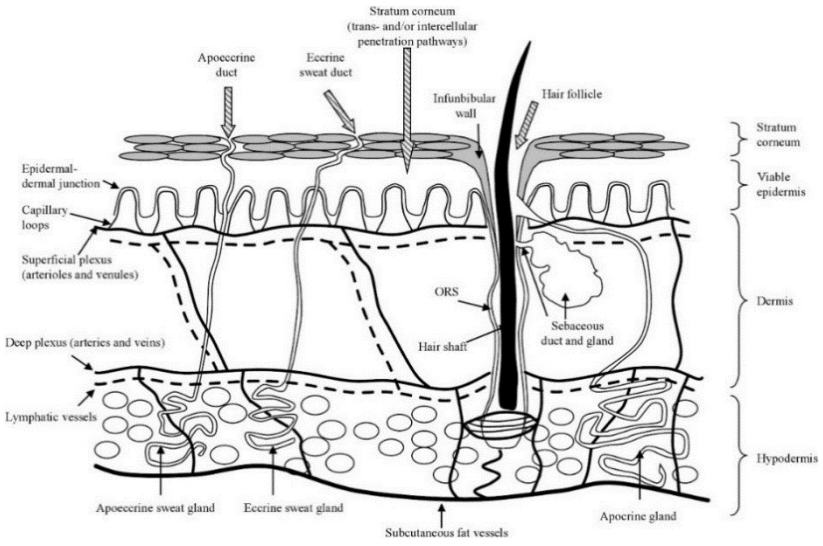

Figure 1-1. Schematic overview of human skin[4].

The epidermis consists primarily of keratinocyte cells of various forms and is further divided into four strata which separates them based on their level of differentiation, as shown in Figure 1-2. The stratum basale (stratum germinativum) is the lowest layer of the epidermis which consists of a single layer of primarily keratinocyte cells joined together by junctions known as desmosomes and are anchored to the dermal-epidermal junction by hemidesmosomes. Melanocytes and Merkel cells are also interspersed in this layer. Melanocytes produce melanin which is responsible for skin pigmentation.

The cells at the lower level of the stratum spinosum most closely resemble the cells in the stratum basale. They differentiate by becoming flatter as they approach the stratum granulosum. The stratum spinosum contains more desmosomes with multiple linkages between the keratinocytes. As these cells further differentiate, lamellar granules appear which are secretory organelles that carry lipids and enzymes. This layer of the epidermis also contains the most abundant supply of Langerhans cells that are responsible for the immune system.

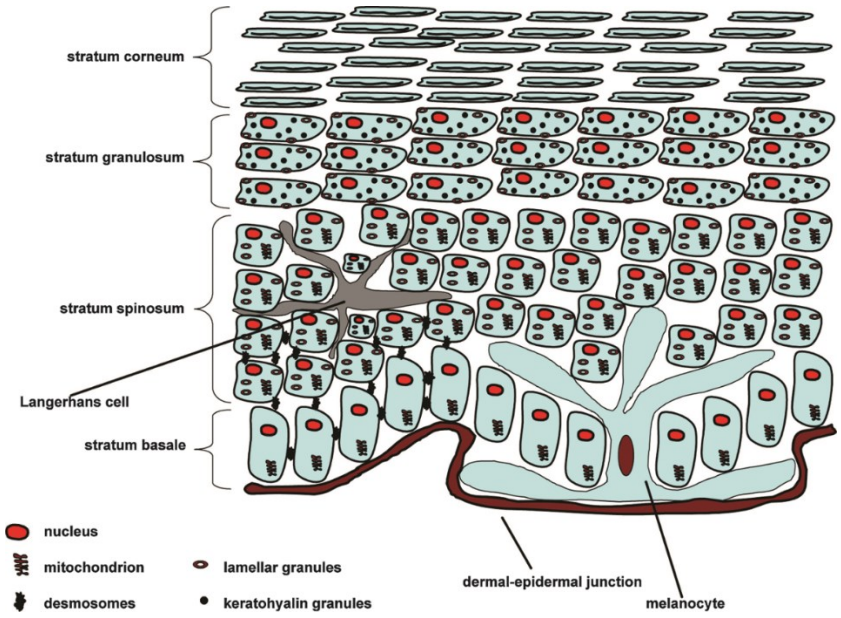

Figure 1-2 Diagram showing layers of the epidermis. Originally published in Roger L. McMullen, *Antioxidants and the Skin*, Allured Books: Carol Stream, IL (2013). Reprinted with permission from Roger L. McMullen, copyright (2013).

The stratum granulosum [SG] is only several layers of cells thick and forms the transition region between the viable and fully differentiated epidermis. The SG is the point between the appearance of new cellular components and the occurrence of programmed apoptosis. The cells start to accumulate keratohyalin granules, a dense material that makes the keratinocyte appear granular and assume a flattened structure. The keratinocyte goes through several transformations transitioning from a granular to a cornified cell[5]. The ribosomes, mitochondria, and nuclei start to disintegrate and the plasma membrane is no longer able to survive and is replaced by a thick cornified cell envelope. The cell envelope is formed inside the boundaries of the plasma membrane and is rich in proteins. At this point the cell envelope is reinforced by cross-linked lysine isopeptides and is insoluble and impermeable to polar substances[6].

The stratum corneum [SC] contains the cornified cell envelope and is completely void of organelles, referred to as corneocytes. Within the SC, the corneocytes are embedded in a lipid matrix forming the “Bricks and Mortar” structure in which the corneocytes correspond to the bricks and the lipids to the mortar, Figure 1-3. These lipids form neatly arranged lipid layers stacked on top of each other and oriented approximately parallel to the skin surface with the corneocytes forming the bricks and mortar arrangement throughout the epidermis. The corneocytes of SC at this stage are considered dead but the process is dynamic as the cell evolves through the mechanism of apoptosis[7-8] and desquamation[9]. The corneocytes of the SC are almost impermeable to most substances which leaves the SC lipid domain open as the barrier for compound penetration[10]. The lipid matrix of the SC is composed of ceramides, cholesterol and free fatty acids in equimolar amounts[11-12].

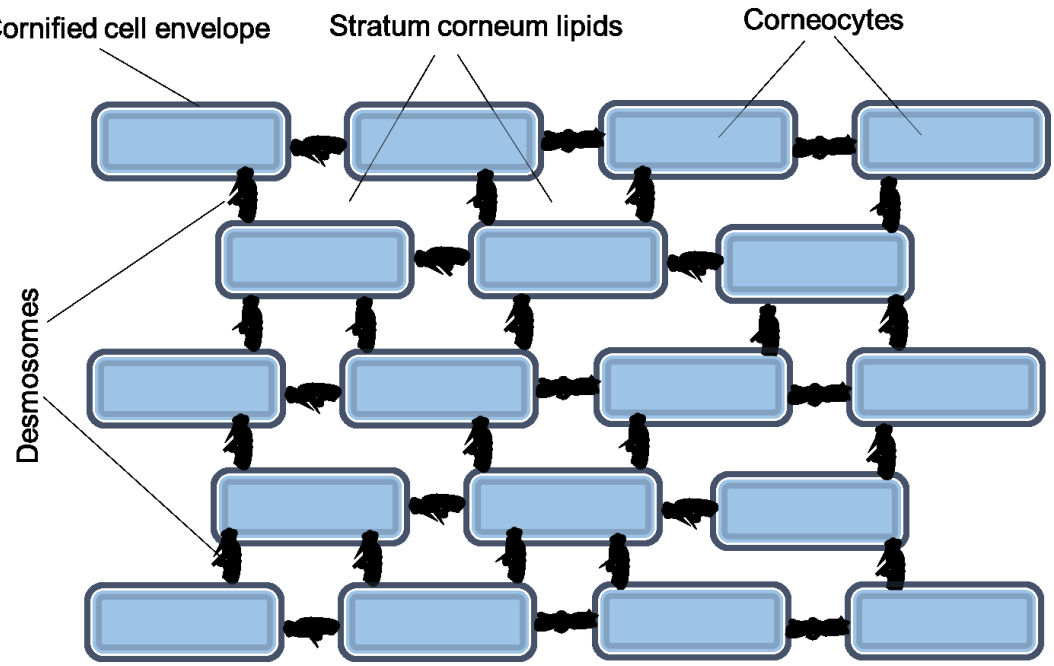

Figure 1-3. Bricks and mortar structure of the stratum corneum.

The SC lipids lie within the intercellular space of the corneocytes and the organization of these lipids is essential in forming the protective barrier of the skin. The SC lipids form lamellar sheets that are stacked on top of each other between the corneocytes as shown in Figure 1-4[13-14]. Two types of lipid lamellar phases are observed in the human SC and they are differentiated by their periodicities or repeat distance. The lipids in the long periodicity phase (LPP) have a repeat distance of approximately 13 nm while the short periodic phase (SPP) has a repeat distance of 6.4 nm[15-16]. Many studies have been done investigating these two lamellar phases and it was shown that the LPP lipids play an essential role in the barrier function of the skin[17].

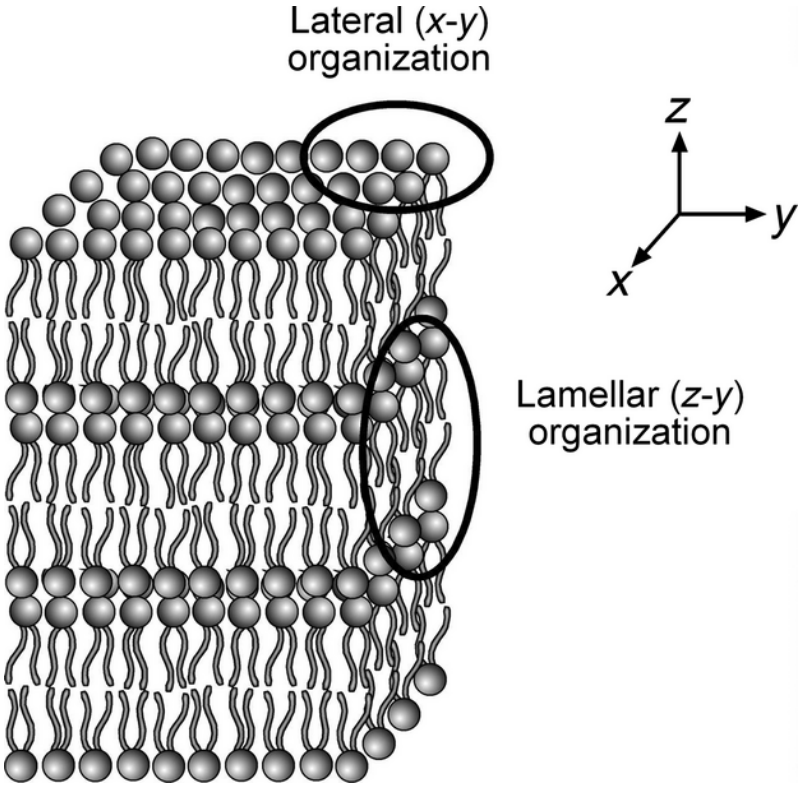

Figure 1-4. Schematic illustration of the three-dimensional structure of the lipid lamellae indicating the lateral organization and the lamellar organization[18].

The lipid arrangement or packing within the lamellae is termed “lateral organization”[12]. This packing refers to how close in space and organized the lipids are to each other. The lateral organization incorporates three categories termed liquid, hexagonal and orthorhombic packing. The lipids chains in the liquid lateral organization are disordered and loosely packed; they become more ordered and densely packed through the hexagonal to the orthorhombic lateral organization[12]. The SC lipids in healthy human skin at physiological temperatures are mostly arranged in an orthorhombic phase with small amounts in the hexagonal and liquid forms [19-20].

1.2 Permeation Pathway

There are basically two pathways for substances to pass through the skin. One is by diffusion through the SC; the other is by the appendageal pathways such as hair follicles or glands[21-22]. Based on the composition of the SC, there are two possible routes for diffusion through skin, the intercellular route and the transcellular route[23]. The intercellular route requires passing through the lipid bilayer avoiding the corneocytes. One would assume that this route is longer, but compared to diffusion through the corneocytes, this route is relatively fast. The liquid crystalline structures of the lipid matrix allow it to form hydrophobic and hydrophilic domains; therefore, both hydrophobic and hydrophilic materials can pass via this pathway. The transcellular pathway requires passing through both the solid corneocytes and the lipid bilayers. Diffusion through the solid corneocytes is slow which makes this pathway more difficult. The follicular route has received much attention lately because this pathway has been shown to be important for percutaneous absorption and can be used for drug delivery[21, 24].

Products are routinely applied to the skin for cosmetic purposes or as a drug to treat diseases. For cosmetic applications, the material is expected to remain on the surface whereas drugs are expected to penetrate the skin barrier. Therefore, it is important to understand the penetration process and to investigate ingredients that can enhance and/or prevent permeation. Pharmaceutical companies have been using skin to deliver drugs for many years. Chemical or

physical approaches to compromise the barrier of the SC are applied. The chemical approach uses ingredients known as chemical penetration enhancers (CPE) to modify the skin barrier properties. Since the skin barrier can easily be compromised by different chemicals, there are growing concerns over the toxicity associated with daily use products such as sunscreens, mosquito repellents, agrochemical, and household cleaning chemicals penetrating the SC.

Researchers have relied on different methods to measure diffusion of active agents into skin. Common techniques include the Franz diffusion cell[25-26] and radiolabeled-based techniques to measure skin permeation in-vitro[27] and the tape stripping method for in-vivo measurements. With growing advances in the optical technologies, there are various Raman techniques to measure such penetration in-vivo[28] and in-vitro.

The Franz diffusion cell method typically uses either human or pig skin. The skin sample is mounted in a Franz diffusion cell filled with a buffer solution with the bottom of the skin section touching the buffer. The surface of the skin is then treated with product. The cell is sealed and incubated at fixed temperature over time. The receptor solution is exchanged at different time intervals and analyzed for the active material.

The tape stripping method has been used to study skin penetration for decades. It is a simple approach that uses adhesive film to remove layers of skin. Each tape strip is expected to remove corneocytes layer by layer; however, there

are many disadvantages using this method[29-30]. The first major problem is the presence of furrows and wrinkles in the skin. This makes the surface irregular, so that the first couple of strips are only removing the stratum corneum (SC) of the hills followed by the SC of the furrows and wrinkles[31]. Therefore, if you are tracking topically-applied material, you may not get an accurate indication of the depth of penetration or thickness of the film. There are also concerns that the initial tape strips may not remove SC, but the material that is applied; therefore, the number of removal strips may not correlate with the assumed depth[30].

Raman microscopy allows researchers to measure penetration kinetics non-invasively. Using this technique, it is now easier and more efficient to investigate the penetration of active ingredient by in-vitro and in-vivo[32-33] approaches. For in-vivo studies, it is required that the ingredients of interest have a Raman signal that does not overlap with any Raman signal from the skin. If the molecule does not have Raman signals well separated from those skin, then the molecule can be deuterated and the investigation can be carried out using in-vitro Raman experiments. In both cases, the product is applied to the surface of the skin. The process allows the scanning of the skin surface to different depths with a resolution of 1-2 μm. This technique allows us to track topically applied product as it penetrates the SC over time; therefore, it offers advantages for kinetics measurements since the same skin barrier can be measured several times.

1.3 Exposure to UV Radiation

Exposure of human skin to ultraviolet (UV) radiation is known to induce damage in DNA and can lead to skin cancer[34-35]. Some skin cancers are linked to genetic factors, but the most common risk factor for skin cancer is indeed exposure to UV [36]. Sunscreen products are formulated with ingredients that either absorb or block UV radiation. Sunscreens exist in many different forms such as creams, lotions, sprays, etc. In the US, sunscreen is considered as an OTC drug and, as such is regulated by the FDA. The maximum use level for each sunscreen molecule is set by the FDA[37]. In other parts of the world, sunscreen is either regulated by the government or by the geographical region. For example, countries in the European Union follow the same regulations whereas usage in Australia, Canada and Japan is regulated by the government[38]. Each of these countries also has different approved sunscreen ingredients with different maximum use level.

The protection provided by a sunscreen is expressed by its sun protection factor (SPF). Each region of the world used a different method to measure the in-vivo SPF[39]. In the past, while most of these standards were similar, they used different parameters; therefore, it was necessary to unify these into a single method so that you get the same SPF value for a single product without regards to the country in which it was tested. This resulted in a single in-vivo method which is the international standard, ISO 24442. The SPF value listed for finished sunscreen products are determined by in-vivo methods following the ISO 24442

guidelines. It is the ratio of the least amount of UV energy required to produce a minimal erythema[40-41] (reddening of the skin caused by UV radiation) on sunscreen protected skin to the amount of UV energy required to produce the same erythema on unprotected skin[42-44]. The SPF number can be interpreted as how much longer a skin covered with sunscreen takes to burn compared to unprotected skin.

The in-vivo method for SPF determination is expensive and time consuming, therefore an in-vitro method was developed for laboratory purposes so that formulators can optimize the SPF value of their final formulation before doing the in-vivo test. A final sunscreen formulation is very complex. Since each ingredient either absorbs in the UVA or UVB region, the formulator can use different combinations and concentrations to get the maximum protection[45]. Therefore, at least two UV ingredients are used in a sunscreen product to get the maximum protection from UV radiation: one with λ_{max} in the UVA region, the other with λ_{max} in the UVB region[46].

The in-vitro SPF method is based on the sunscreen transmission and follows the concept shown in equation 1, in which E(λ) is the erythema action spectrum[47], I(λ) is the spectral irradiance received from the UV source[48-50] and $A_o(\lambda)$ is the absorbance of the test product film. Similar to the in-vivo method before its harmonization, several in-vitro methods exist. While they all follow the principle of equation 1, variation is induced by instrumentation, substrate types, application amounts and procedures.

$$\text{SPF}_{\text{in-vitro}} = \frac{\int_{\lambda=290}^{\lambda=400} E(\lambda)*I(\lambda)d\lambda}{\int_{\lambda=290}^{\lambda=400} E(\lambda)*I(\lambda)*10^{-A_0(\lambda)}d\lambda} \quad (1)$$

UV radiation can be divided into three subtypes (Figure 1-5) of which UVA rays possess the longest wavelength measuring from 320 to 400 nm. UVA rays are not absorbed by the ozone layer and can penetrate deep into the skin through the epidermis and into the dermis. Exposure to UVA rays results primarily in premature skin aging. UVB rays are of shorter wavelength than UVA and range from 290 to 320 nm. Some of the UVB energy is absorbed by the ozone layer. UVB rays penetrate through the stratum corneum into the layer of the epidermis. Exposure to UVB creates a tan by increasing melanin production. Overexposure to UVB radiation results in the erythema swelling and pain, which are signs of sunburn. UVC rays are from 100 to 280 nm and are absorbed by the ozone layer[36].

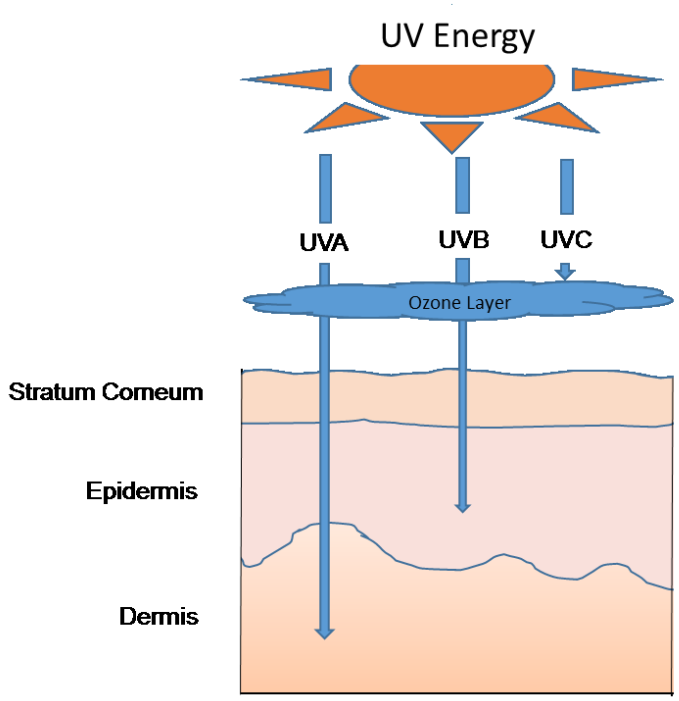

Figure 1-5. Schematic overview of UV radiation as it passes through the atmosphere and the effect on human skin.

1.4 Mechanism of UV absorption

The electromagnetic spectrum spans a frequency range that encompasses many orders of magnitude. The spectrum ranges from low-energy radio frequencies to high frequency gamma-rays. Electromagnetic rays interact with matter in different ways. Figure 1-6 shows the electromagnetic spectrum from x-rays to microwaves depicting the different types of molecular response to each respective radiation. For example, molecules respond to microwaves by rotating, then vibrating as the radiation frequency increases to the infrared (IR). Electronic transitions occur as the frequency is further increased into the visible and UV region.

In terms of the energy required for molecules to respond to each type of radiation, the x-rays region is the highest in energy and ranges from 10^3 to 10^6 eV. The energy decreases as you go to longer wavelength, for example the microwave region energy ranges from 10^{-6} to 0.01 eV.

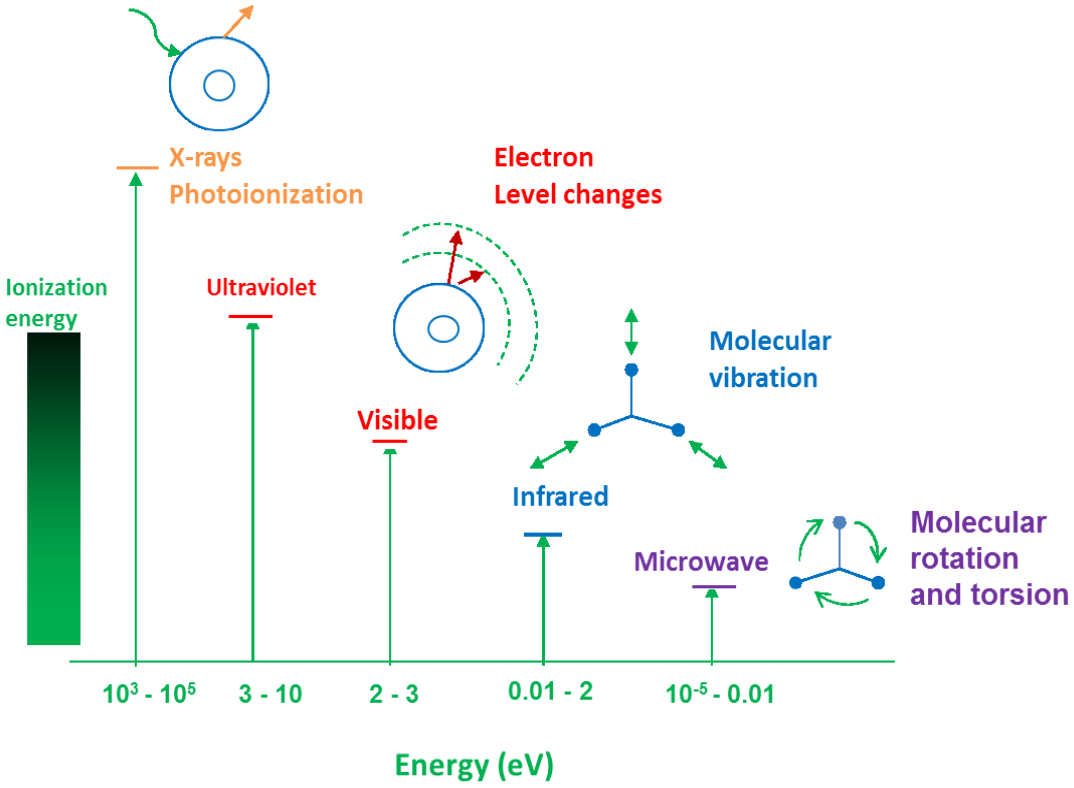

Figure 1-6. Regions of the electromagnetic spectrum showing the effect of different types of radiation on molecules.

When a molecule is exposed to UV radiation, it absorbs a photon if the energy of the photon is equal to the difference in energy between the lowest unoccupied molecular orbital (LUMO) and the highest occupied molecular orbital (HOMO) of the molecule. A schematic representation is shown in Figure 1-7 indicating that

for absorption to take place, the energy of the photon is equal to the difference in energy of the excited state E_1 and the energy of the ground state E_0. It is common for the ground electronic state of a molecule to be a singlet state. This means that all the electrons in the ground state are paired; it is referred to as the S_o or "singlet-zero" state. When the molecule absorbs a photon, the electron is promoted to the excited state. This is termed first excited singlet state (S_1), since the electron is promoted from the ground electronic state (S_0). All transitions from one electronic state to another originate from the lowest vibrational level of the initial electronic state. A more detailed description is shown in the Jablonski diagram in Figure 1-8[51]. The electron can go from the ground state to any singlet excited state, but returns to the S_0 state through internal conversion.

The energy in the S_1 state can be deactivated by a series of events. The simplest is either vibrational relaxation or through fluorescence back to the ground state. Under certain conditions, the singlet excited state can go through an intersystem crossing resulting in a triplet excited state (T_1). The energy in the triplet state can be dissipated back to the ground state through phosphorescence or it can be transferred to other receptor molecules. Chemical bonds in the molecule can also break apart during a photochemical event.

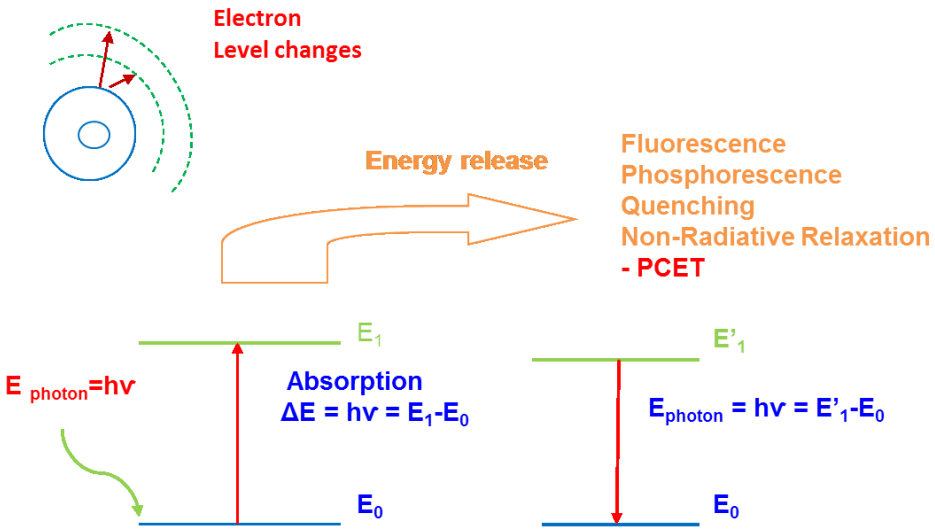

Figure 1-7. Schematic showing the absorption process.

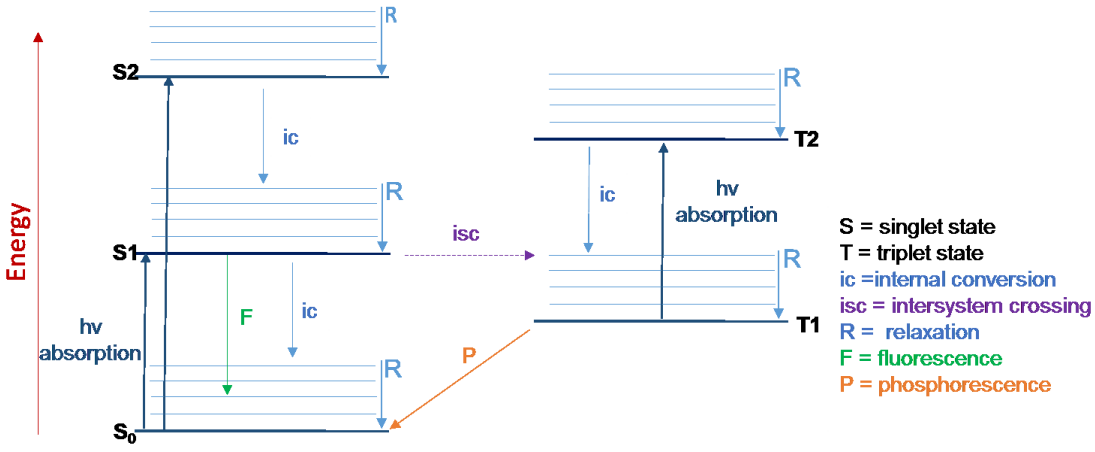

Figure 1-8. Jablonski diagram showing the possible sequence of events following absorption of a photon.

1.5 Proton-coupled Electron Transfer Reaction

Proton-coupled electron transfer (PCET) involves the transfer of electrons and protons[52-53]. It is an important pathway for charge transfer in a variety of systems[54]. The theory of PCET is challenging because it involves a wide range of time scales and requires understanding of the quantum mechanical behavior of both electrons and transferring protons. There are different theories with the earliest developed by Cukier[52] followed by Soudackov and Hammes-Schiffer[55-56]. From the general definition of PCET, the mechanism can be either sequential or concerted and the electron and proton can transfer in different directions or in the same direction, either between the same sites or between different sites[53]. Figure 1-9A shows a general scheme for a PCET reaction involving one proton and one electron, where H represents the transferring proton, D_e and A_e represent a general electron donor and acceptor, with D_p and A_p representing the proton donor and acceptor respectively. A schematic of this representation showing the sequential and concerted processes is shown in Figure 1-9B. There are two paths in the sequential mechanism. One is when the proton transfer occurs prior to the electron (i.e., 1a to 1b then to 2b) or when the electron transfers before the proton (i.e., 1a to 2a then to 2b). During the concerted mechanism the electron and proton transfer simultaneously (i.e., 1a to 2b)[57]. PCET concerted and sequential mechanisms can be distinguished by the presence of a stable intermediate for the sequential process. This is easily

determined if the reaction intermediate can be isolated. However, this may not be possible for excited states - PCET reactions that occur on very fast timescales.

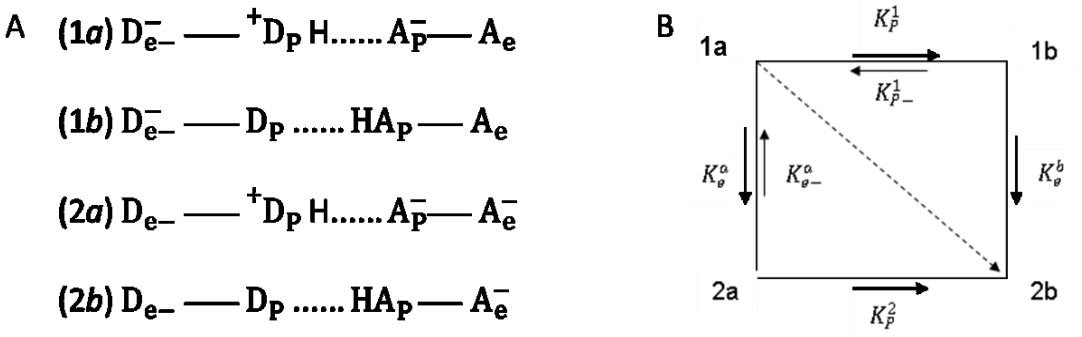

Figure 1-9. (A) General Scheme of PCET. (B) Schematic representation showing sequential and concerted processes.

1.6 Confocal Raman Microscopy

As mentioned previously, we know that as electromagnetic radiation interacts with a molecule, it can be absorbed if the energy difference between the excited state and ground state of the molecule matches the energy of the incident photon, which results in electronic transition such as UV interaction. Similarly, when a molecule interacts with IR radiation, 400 to 4,000 cm^{-1}, it may result in a vibrational transition. In most cases the radiation does not match any transition and the radiation is scattered. When the scattered photons have the same energy as the incoming photons, this is termed elastic scattering known as Rayleigh scattering. However, sometimes the molecule changes its vibrational state upon interaction with the incoming photon resulting in a process where the energy of

the scattered photon equals the difference between the incident photon frequency and the frequency of the vibrational transition[58]. This is termed inelastic scattering, also known as Raman scattering described by Raman and Krishnan in 1928[59]. If the scattered photons have lower energy than the incident photons, the process is termed Stokes scattering and the photons are found at longer wavelengths compared to the incident light. On the other hand, if the scattered photons have higher energy than the incident photons, the process is termed anti-Stokes scattering. These different types of scattering are depicted schematically in Figure 1-10 (A).

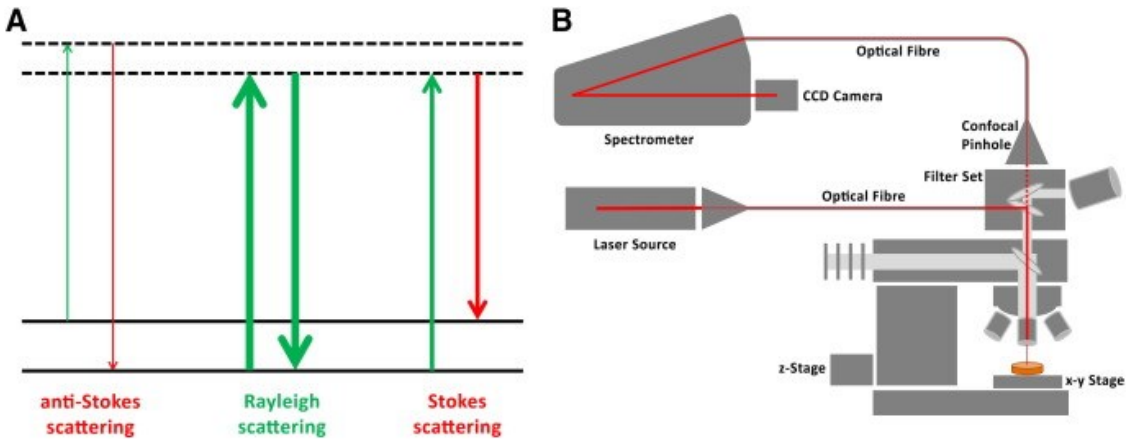

Figure 1-10. (A) Energy level diagram showing different types of scattering. (B) Schematic of the confocal Raman microscope setup[60].

Current confocal Raman microscopes use a laser of fixed wavelength to induce Raman scattering. The laser beam is focused onto the sample using a microscope objective and the Raman scattered light is typically collected with the same objective. The collected light passes through a series of spatial filtering

using the principle of confocal microscopy[61]. Using this technique, scattered light is collected from an image spot and is then focused onto an aperture (pinhole) in front of the detector. The size of the pinhole determines how much light reaches the detector; and the size of the pinhole can be adjusted so that only rays that come from the focal plane reach the detector. Resolution in confocal Raman microscopy typically ranges from 300 nm to 2 μm in the lateral (x~y) direction and 1-6 μm in the z direction, depending on the laser wavelength and the numerical aperture of the objective lens[58, 61]. The collected light is then detected and analyzed by the spectrometer and a charge-coupled device (CCD) unit. A schematic of a typical confocal Raman setup is shown in Figure 1-10 (B).

Confocal Raman microscopy (CRM) offers many advantages over conventional microscopy mainly because it is a noninvasive optical method. It allows us to obtain detailed information of the sample being investigated while preserving the sample as close as possible to its native state. It can provide a spectroscopic fingerprint of the molecule being studied along with the environment of the molecule. Researchers have been utilizing Raman microscopy for imaging the internal structure of biological cells because of its potential to overcome the limitations of label-based fluorescence techniques. Using a label-free method gives one the opportunity to obtain information of cells in their native states since most fluorophores used in fluorescence techniques are harmful to the cells[58].

Since Raman spectroscopy is a noninvasive method, it can be used to obtain information on ex-vivo and in-vivo samples. Paudney et. al.[62] successfully tracked the delivery of trans-retinol penetration into in-vivo skin of the volar forearm of volunteers when applied as a cream. They were able to distinguish the difference in the penetration profile of trans retinol when a different solvent combination was used in the cream formulation. Forster et. al.[63] used similar techniques for retinol delivery using different solvents. Casper et. al.[32] were able to determine the relative water concentrations in in-vivo stratum corneum as a function of the distance to the skin surface using confocal Raman. Their results were also in agreement with previously published in-vitro x-ray analysis.

1.7 Commercial Sunscreen and Insect Repellent

Exposure of human skin to ultraviolet (UV) radiation is known to induce damage in the DNA and can lead to skin cancer[34-35]. To protect the skin from such damage, a variety of sunscreen products have been developed. Sunscreen products are formulated with ingredients that either absorb or block UV radiation. To achieve adequate protection, international standards specified that the sunscreen must be evenly applied at a level of 2mg/cm^2 over the surface of the skin[39, 64]. However, the skin itself presents a major challenge for application of a uniform film because its surface appears undulating with peaks and valleys[65]. Because of these contours, sunscreen filters may not be distributed evenly during application. Creams will fill the valleys and glyphs first while leaving the peaks

with a thinner film, so that overall the skin will not be evenly protected from UV radiation[64, 66]. The performance of a sunscreen product is not only related to spreading and distribution of the film but also to the photostability of the sunscreen actives[67-69]. Therefore, the first part of this thesis will focus on understanding the photochemistry of the sunscreen ingredient, Bemotrizinol, in common solvents. The second goal is to evaluate the permeation and spreading of Bemotrizinol in the SC when applied using a typical sunscreen formulation. We also want to investigate the effect of polymers on the spreading of the sunscreen on the skin since some polymers also give an increase in the SPF value[70-71].

Since confocal Raman microscopy (CRM) has the capability to non-invasively map the chemical properties of a sample by providing depth profiles along with molecular structure information from both the skin and the exogenous formulation, our third goal is to utilize this approach to investigate the permeation of DEET (N,N-diethyl-m-toluamide) in the SC when applied from a commercial insect repellent product. Then we plan to investigate the effect of polymers on the permeation when added to the commercial formulation and applied to ex-vivo human skin.

1.8 References I

1. Madison, K. C., Barrier function of the skin: "la raison d'etre" of the epidermis. *The Journal of investigative dermatology* **2003,** *121* (2), 231-41.
2. Blatteis, C. M., Age-dependent changes in temperature regulation - a mini review. *Gerontology* **2012,** *58* (4), 289-95.
3. Schmelz, M., Neuronal sensitivity of the skin. *European journal of dermatology : EJD* **2011,** *21 Suppl 2*, 43-7.
4. Reprinted from Advanced Drug Delivery Reviews, 65 /2, Jepps, O. G.; Dancik, Y; Anissimov, Y. G.; Roberts, M. S.; Modeling the human skin barrier — Towards a better understanding of dermal absorption, 152-168., 2013, with permission from Elsevier.
5. Candi, E.; Schmidt, R.; Melino, G., The cornified envelope: a model of cell death in the skin. *Nature reviews. Molecular cell biology* **2005,** *6* (4), 328-40.
6. Nemes, Z.; Steinert, P. M., Bricks and mortar of the epidermal barrier. *Experimental & molecular medicine* **1999,** *31* (1), 5-19.
7. Hengartner, M. O., The biochemistry of apoptosis. *Nature (London)* **2000,** *407* (6805), 770-776.
8. Teraki, Y.; Shiohara, T., Apoptosis and the skin. *European journal of dermatology : EJD* **1999,** *9* (5), 413-25; quiz 426.
9. Milstone, L. M., Epidermal desquamation. *J Dermatol Sci* **2004,** *36* (3), 131-40.
10. Baroni, A.; Buommino, E.; De Gregorio, V.; Ruocco, E.; Ruocco, V.; Wolf, R., Structure and function of the epidermis related to barrier properties. *Clinics in dermatology* **2012,** *30* (3), 257-62.
11. Proksch, E.; Brandner, J. M.; Jensen, J. M., The skin: an indispensable barrier. *Experimental dermatology* **2008,** *17* (12), 1063-72.
12. Boncheva, M., The physical chemistry of the stratum corneum lipids. *Int J Cosmet Sci* **2014,** *36* (6), 505-15.
13. Janssens, M.; van Smeden, J.; Gooris, G. S.; Bras, W.; Portale, G.; Caspers, P. J.; Vreeken, R. J.; Hankemeier, T.; Kezic, S.; Wolterbeek, R.; Lavrijsen, A. P.; Bouwstra, J. A., Increase in short-chain ceramides correlates with an altered lipid organization and decreased barrier function in atopic eczema patients. *Journal of lipid research* **2012,** *53* (12), 2755-66.
14. Thakoersing, V. S.; Gooris, G. S.; Mulder, A.; Rietveld, M.; El Ghalbzouri, A.; Bouwstra, J. A., Unraveling barrier properties of three different in-house human skin equivalents. *Tissue engineering. Part C, Methods* **2012,** *18* (1), 1-11.
15. Janssens, M.; van Smeden, J.; Gooris, G. S.; Bras, W.; Portale, G.; Caspers, P. J.; Vreeken, R. J.; Kezic, S.; Lavrijsen, A. P.; Bouwstra, J. A., Lamellar lipid organization and ceramide composition in the stratum corneum of patients with atopic eczema. *The Journal of investigative dermatology* **2011,** *131* (10), 2136-8.
16. White, S. H.; Mirejovsky, D.; King, G. I., Structure of lamellar lipid domains and corneocyte envelopes of murine stratum corneum. An X-ray diffraction study. *Biochemistry* **1988,** *27* (10), 3725-32.
17. Groen, D.; Poole, D. S.; Gooris, G. S.; Bouwstra, J. A., Is an orthorhombic lateral packing and a proper lamellar organization important for the skin barrier function? *Biochimica et biophysica acta* **2011,** *1808* (6), 1529-37.
18. Boncheva, M., The physical chemistry of the stratum corneum lipids

Int J Cosmet Sci **2014**, 505-15.
19. Damien, F.; Boncheva, M., The extent of orthorhombic lipid phases in the stratum corneum determines the barrier efficiency of human skin in vivo. *The Journal of investigative dermatology* **2010,** *130* (2), 611-4.
20. Bouwstra, J.; Pilgram, G.; Gooris, G.; Koerten, H.; Ponec, M., New aspects of the skin barrier organization. *Skin pharmacology and applied skin physiology* **2001,** *14 Suppl 1*, 52-62.
21. Lademann, J.; Richter, H.; Teichmann, A.; Otberg, N.; Blume-Peytavi, U.; Luengo, J.; Weiß, B.; Schaefer, U. F.; Lehr, C.-M.; Wepf, R.; Sterry, W., Nanoparticles – An efficient carrier for drug delivery into the hair follicles. *European Journal of Pharmaceutics and Biopharmaceutics* **2007,** *66* (2), 159-164.
22. Knorr, F.; Lademann, J.; Patzelt, A.; Sterry, W.; Blume-Peytavi, U.; Vogt, A., Follicular transport route – Research progress and future perspectives. *European Journal of Pharmaceutics and Biopharmaceutics* **2009,** *71* (2), 173-180.
23. Gonzalez, H., Percutaneous absorption with emphasis on sunscreens. *Photochem. Photobiol. Sci.* **2010,** *9* (4), 482-488.
24. Lademann, J.; Otberg, N.; Richter, H.; Weigmann, H. J.; Lindemann, U.; Schaefer, H.; Sterry, W., Investigation of follicular penetration of topically applied substances. *Skin pharmacology and applied skin physiology* **2001,** *14 Suppl 1*, 17-22.
25. Kasting, G. B.; Bhatt, V. D.; Speaker, T. J., Microencapsulation decreases the skin absorption of N,N-diethyl-m-toluamide (DEET). *Toxicology in Vitro* **2008,** *22* (2), 548-552.
26. Ross, J. S.; Shah, J. C., Reduction in skin permeation of N,N-diethyl-m-toluamide (DEET) by altering the skin/vehicle partition coefficient. *Journal of Controlled Release* **2000,** *67* (2–3), 211-221.
27. Santhanam, A.; Miller, M. A.; Kasting, G. B., Absorption and evaporation of N,N-diethyl-m-toluamide from human skin in vitro. *Toxicology and Applied Pharmacology* **2005,** *204* (1), 81-90.
28. Pot, L. M.; Coenraads, P. J.; Blomeke, B.; Puppels, G. J.; Caspers, P. J., Real-time detection of p-phenylenediamine penetration into human skin by in vivo Raman spectroscopy. *Contact Dermatitis* **2016,** *74* (3), 152-158.
29. Bashir, S. J.; Chew, A. L.; Anigbogu, A.; Dreher, F.; Maibach, H. I., Physical and physiological effects of stratum corneum tape stripping. *Skin research and technology : official journal of International Society for Bioengineering and the Skin (ISBS) [and] International Society for Digital Imaging of Skin (ISDIS) [and] International Society for Skin Imaging (ISSI)* **2001,** *7* (1), 40-8.
30. Jacobi, U.; Weigmann, H. J.; Ulrich, J.; Sterry, W.; Lademann, J., Estimation of the relative stratum corneum amount removed by tape stripping. *Skin research and technology : official journal of International Society for Bioengineering and the Skin (ISBS) [and] International Society for Digital Imaging of Skin (ISDIS) [and] International Society for Skin Imaging (ISSI)* **2005,** *11* (2), 91-6.
31. Lademann, J.; Meinke, M. C.; Schanzer, S.; Richter, H.; Darvin, M. E.; Haag, S. F.; Fluhr, J. W.; Weigmann, H. J.; Sterry, W.; Patzelt, A., In vivo methods for the analysis of the penetration of topically applied substances in and through the skin barrier. *Int J Cosmet Sci* **2012,** *34* (6), 551-9.
32. Caspers, P. J.; Bruining, H. A.; Puppels, G. J.; Lucassen, G. W.; Carter, E. A., In Vivo Confocal Raman Microspectroscopy of the Skin: Noninvasive Determination of Molecular Concentration Profiles. *Journal of Investigative Dermatology* **2001,** *116* (3), 434-442.
33. Nakagawa, N.; Matsumoto, M.; Sakai, S., In vivo measurement of the water content in the dermis by confocal Raman spectroscopy. *Skin research and technology : official journal of*

International Society for Bioengineering and the Skin (ISBS) [and] International Society for Digital Imaging of Skin (ISDIS) [and] International Society for Skin Imaging (ISSI) **2010,** *16* (2), 137-41.
34. Young, A. R.; Chadwick, C. A.; Harrison, G. I.; Nikaido, O.; Ramsden, J.; Potten, C. S., The similarity of action spectra for thymine dimers in human epidermis and erythema suggests that DNA is the chromophore for erythema. *The Journal of investigative dermatology* **1998,** *111* (6), 982-8.
35. Hacham, H.; Freeman, S. E.; Gange, R. W.; Maytum, D. J.; Sutherland, J. C.; Sutherland, B. M., Do pyrimidine dimer yields correlate with erythema induction in human skin irradiated in situ with ultraviolet light (275-365 nm)? *Photochemistry and photobiology* **1991,** *53* (4), 559-63.
36. Watson, M.; Holman, D. M.; Maguire-Eisen, M., Ultraviolet Radiation Exposure and Its Impact on Skin Cancer Risk. *Seminars in Oncology Nursing* **2016,** *32* (3), 241-254.
37. Wang, S. Q.; Lim, H. W., Current status of the sunscreen regulation in the United States: 2011 Food and Drug Administration's final rule on labeling and effectiveness testing. *Journal of the American Academy of Dermatology* **2011,** *65* (4), 863-869.
38. Sambandan, D. R.; Ratner, D., Sunscreens: An overview and update. *Journal of the American Academy of Dermatology* **2011,** *64* (4), 748-758.
39. ISO, Cosmetics - Sun protection test methods - Review and evaluation of methods to assess the photoprotection of sun protection products. *ISO/TR 26369*.
40. Young, A. R.; Chadwick, C. A.; Harrison, G. I.; Hawk, J. L. M.; Nikaido, O.; Potten, C. S., The in situ repair kinetics of epidermal thymine dimers and 6-4 photoproducts in human skin types I and II. *J. Invest. Dermatol.* **1996,** *106* (6), 1307-1313.
41. Harrison, G. I.; Young, A. R., Ultraviolet radiation-induced erythema in human skin. *Methods (San Diego, CA, U. S.)* **2002,** *28* (1), 14-19.
42. Binks, B. P.; Fletcher, P. D. I.; Johnson, A. J.; Marinopoulos, I.; Crowther, J.; Thompson, M. A., How the sun protection factor (SPF) of sunscreen films change during solar irradiation. *Journal of Photochemistry and Photobiology A: Chemistry* **2017,** *333*, 186-199.
43. Wang, S. Q.; Stanfield, J. W.; Osterwalder, U., In vitro assessments of UVA protection by popular sunscreens available in the United States. *Journal of the American Academy of Dermatology* **2008,** *59* (6), 934-942.
44. Kockler, J.; Oelgemöller, M.; Robertson, S.; Glass, B. D., Photostability of sunscreens. *Journal of Photochemistry and Photobiology C: Photochemistry Reviews* **2012,** *13* (1), 91-110.
45. Schulz, J.; Hohenberg, H.; Pflücker, F.; Gärtner, E.; Will, T.; Pfeiffer, S.; Wepf, R.; Wendel, V.; Gers-Barlag, H.; Wittern, K. P., Distribution of sunscreens on skin. *Advanced Drug Delivery Reviews* **2002,** *54, Supplement*, S157-S163.
46. Osterwalder, U.; Sohn, M.; Herzog, B., Global state of sunscreens. *Photodermatology, photoimmunology & photomedicine* **2014,** *30* (2-3), 62-80.
47. 17166, I., Erythema reference action spectrum and standard erythema dose.
48. Anders, A.; Altheide, H.-J.; Knaelmann, M.; Tronnier, H., Action spectrum for erythema in humans investigated with dye lasers. *Photochem. Photobiol.* **1995,** *61* (2), 200-1.
49. Young, A. R.; Chadwick, C. A.; Harrison, G. I.; Nikaido, O.; Ramsden, J.; Potten, C. S., The similarity of action spectra for thymine dimers in human epidermis and erythema suggests that DNA is the chromophore for erythema. *J. Invest. Dermatol.* **1998,** *111* (6), 982-988.
50. Harrison, G. I.; Young, A. R.; McMahon, S. B., Ultraviolet radiation-induced inflammation as a model for cutaneous hyperalgesia. *J. Invest. Dermatol.* **2004,** *122* (1), 183-189.
51. Frackowiak, D., The Jablonski diagram. *Journal of Photochemistry and Photobiology B: Biology* **1988,** *2* (3), 399.

52. Cukier, R. I.; Nocera, D. G., Proton-coupled electron transfer. *Annual review of physical chemistry* **1998,** *49*, 337-69.
53. Mayer, J. M.; Rhile, I. J., Thermodynamics and kinetics of proton-coupled electron transfer: stepwise vs. concerted pathways. *Biochimica et Biophysica Acta (BBA) - Bioenergetics* **2004,** *1655*, 51-58.
54. Kretchmer, J. S.; Miller, T. F., Tipping the Balance between Concerted versus Sequential Proton-Coupled Electron Transfer. *Inorg. Chem.* **2016,** *55* (3), 1022-1031.
55. Soudackov, A.; Hammes-Schiffer, S., Theoretical Study of Photoinduced Proton-Coupled Electron Transfer through Asymmetric Salt Bridges. *J. Am. Chem. Soc.* **1999,** *121* (45), 10598-10607.
56. Soudackov, A.; Hammes-Schiffer, S., Multistate continuum theory for multiple charge transfer reactions in solution. *J. Chem. Phys.* **1999,** *111* (10), 4672-4687.
57. Hammes-Schiffer, S.; Soudackov, A. V., Proton-Coupled Electron Transfer in Solution, Proteins, and Electrochemistry. *J. Phys. Chem. B* **2008,** *112* (45), 14108-14123.
58. Opilik, L.; Schmid, T.; Zenobi, R., Modern Raman imaging: vibrational spectroscopy on the micrometer and nanometer scales. *Annual review of analytical chemistry (Palo Alto, Calif.)* **2013,** *6*, 379-98.
59. Raman, C. V.; Krishnan, K. S., A new type of secondary radiation. *Nature (London, U. K.)* **1928,** *121*, 501-2.
60. Reprinted from Advanced Drug Delivery Reviews, 89, Franzen, L.; Windbergs, M.,; Applications of Raman spectroscopy in skin research - From skin physiology and diagnosis up to risk assessment and dermal drug delivery, 91-104., 2015, with permission from Elsevier
61. Everall, N. J., Confocal Raman microscopy: performance, pitfalls, and best practice. *Appl. Spectrosc.* **2009,** *63* (9), 245A-262A.
62. Pudney, P. D. A.; Melot, M.; Caspers, P. J.; Van Der Pol, A.; Puppels, G. J., An in vivo confocal Raman study of the delivery of Trans-retinol to the skin. *Appl. Spectrosc.* **2007,** *61* (8), 804-811.
63. Forster, M.; Bolzinger, M.-A.; Ach, D.; Montagnac, G.; Briancon, S., Ingredients tracking of cosmetic formulations in the skin: a confocal Raman microscopy investigation. *Pharm Res* **2011,** *28* (4), 858-72.
64. Stokes, R.; Diffey, B., How well are sunscreen users protected? *Photodermatology, photoimmunology & photomedicine* **1997,** *13* (5-6), 186-8.
65. Osterwalder, U.; He, Q.; Sohn, M.; Herzog, B., Sustainable sun protection with sunscreens requires the right technology and good compliance. *SOFW J.* **2012,** *138* (7), 2,4-6,8,10-12,14-16,18.
66. Lademann, J.; Rudolph, A.; Jacobi, U.; Weigmann, H. J.; Schaefer, H.; Sterry, W.; Meinke, M., Influence of nonhomogeneous distribution of topically applied UV filters on sun protection factors. *Journal of biomedical optics* **2004,** *9* (6), 1358-62.
67. Sayre, R. M.; Dowdy, J. C.; Gerwig, A. J.; Shields, W. J.; Lloyd, R. V., Unexpected photolysis of the sunscreen octinoxate in the presence of the sunscreen avobenzone. *Photochem. Photobiol.* **2005,** *81* (Mar./Apr.), 452-456.
68. Lhiaubet-Vallet, V.; Marin, M.; Jimenez, O.; Gorchs, O.; Trullas, C.; Miranda, M. A., Filter-filter interactions. Photostabilization, triplet quenching and reactivity with singlet oxygen. *Photochem. Photobiol. Sci.* **2010,** *9* (4), 552-558.
69. Paris, C.; Lhiaubet-Vallet, V.; Jimenez, O.; Trullas, C.; Miranda, M. A., A blocked diketo form of avobenzone: photostability, photosensitizing properties and triplet quenching by a triazine-derived UVB-filter. *Photochem. Photobiol.* **2009,** *85* (1), 178-184.

70. Rigano, L., 'Very' water-resistant sunscreens. *Cosmet. Toiletries* **2014,** *129* (3), 66, 68-73.
71. Zeng, F.; Schwartz, C. In *Polymer technologies in sunscreens*, American Chemical Society: 2016; pp POLY-214.

Chapter 2 Materials and Methods

2.1 Materials

Bemotrizinol (Escalol S), Lauryl Lactate (Ceraphyl 41), Ashland 980 Carbomer and phenethyl benzoate (X-Tend 226) and the following polymers, S2000 (Ganex Sensory - VP/acrylates/lauryl methacrylate copolymer), ES425 (Gantrez ES 425 - Butyl ester of PVM/MA copolymer), G904 (Ganex P-904 LC - Butylated PVP), P100 (Ultrathix P-100 - Acrylic Acid/VP Crosspolymer) were supplied by Ashland. OFF! Deep Woods by SC Johnson was purchased over the counter. DEET was purchased from Vertellus. Ethanol, ethanol d-6, n-hexane, n-hexadecane and acetonitrile were spectroscopic grade solvents purchased from Aldrich. A Crodafos CES-PA (Cetearyl alcohol, decetyl phosphate and ceteth-10-phosphate) sample was supplied by CRODA. Human abdominal skin from plastic surgery was obtained from a dermatological office with patient consent and ethics board approval. Skin sections were stored at -20 ^{o}C for no more than six months. HelioScreen HD6 PMMA plates were purchased from Labsphere.

2.2 Sample preparation

UV-vis absorption spectroscopy; Time-resolved absorption spectroscopy - Bemotrizinol was added to the desired solvents at a concentration of 50 μM, then mixed until completely dissolved prior to measurement. For hydrogen-deuterium exchange experiments, deuterated bemotrizinol was prepared by first dissolving in ethanol d-6. The mixture was then dried under vacuum to remove ethanol d-

6, after which the sample was placed in a glove box under nitrogen gas and n-hexadecane was added.

Confocal Raman measurements - Frozen skin samples were cut and defrosted prior to each experiment. The skin surface was cleaned with a cotton swab to remove excess sebum. For the non-incubated samples, 20 µl of OFF was applied to the surface (size of surface area 0.64 cm^2) and rubbed into the skin using a finger cot for 30 seconds. The skin surface was dry after rubbing. For the incubation part of this study, skin samples were mounted in a Franz diffusion cell (Figure 2-1) and the reservoir was filled with phosphate buffer. The surface of the skin was then treated with 20 µl of the desired product. The cell was then sealed and incubated at 32 °C for 24 hours for the Bemotrizinol experiments. For the DEET permeation experiments, the skin samples were incubated at 32 °C for 2 hours or 4 hours in separate experiments. After incubation, the skin sample was removed from the Franz diffusion cell and the surface was blotted dry with filter paper to remove any excess liquid. The skin was then cut into a 0.25 cm^2 piece and placed in a custom-built sample holder with the SC facing up. A cross section of the sample cell is shown in Figure 2-2. It is made from a brass block milled to accommodate full thickness skin with a hydration chamber underneath. The chamber was filled with distilled water. The skin was placed on a metal mesh that sits on top of the chamber. Double sided 3M tape was placed on both sides around the skin to support a glass cover slip and clay was used to provide a seal around the cover slip.

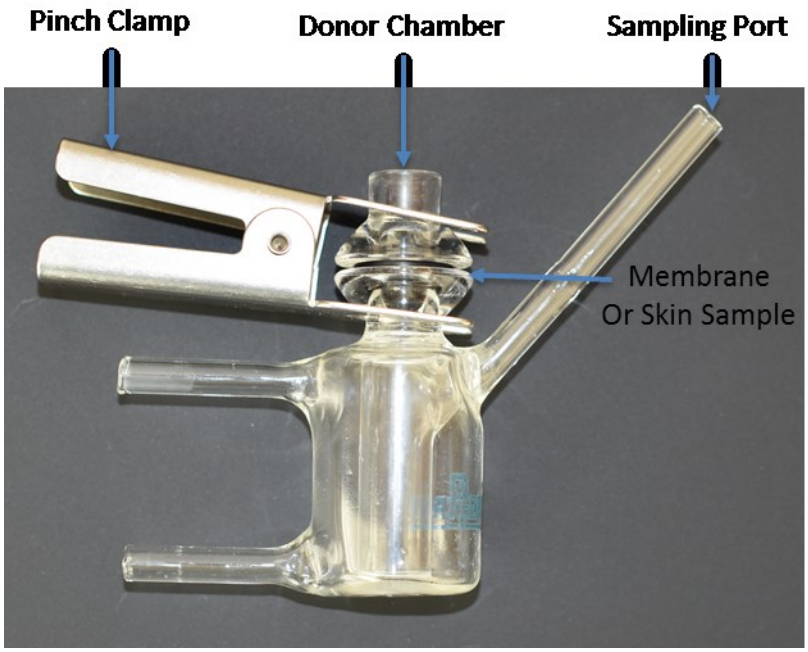

Figure 2-1. Franz diffusion cell system for in-vitro DEET permeation studies.

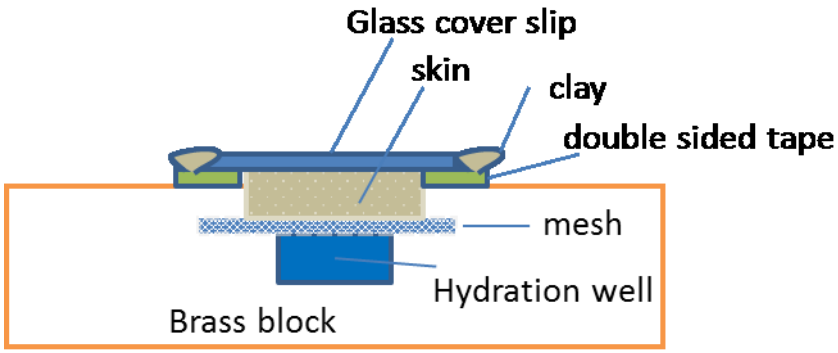

Figure 2-2. Cross section schematic of the sample holder setup to maintain the skin hydration during the Raman measurement.

Preparation of sunscreen emulsion – The sunscreen formulations are shown in Table 2-1 to Table 2-3. To prepare phase A in the main beaker, DI water is added to carbomer with mixing. The ingredients in phase B are combined in a separate beaker. Phase A and phase B are heated on a hot plate to 75 ºC with mixing until all ingredients are dissolved. The ingredients from phase B are added to the main beaker with high shear mixing until uniform. The heat is turned off and the mixture is cooled to 60 ºC. The ingredient in phase C is added while mixing and cooling to room temperature.

Table 2-1. Composition of the sunscreen formula with 3% Bemotrizinol.

Phase	Ingredient	% w/w
A	Water	88.80
	Carbomer (polyacrylic acid)	0.30
B	Bemotrizinol	3.00
	Phenethyl Benzoate	4.00
	Cetearyl alcohol, dicetyl phosphate , ceteth-10 phosphate	3.00
C	Sodium hydroxide 10% solution	0.90
	Total	100.00

Table 2-2. Composition of the sunscreen formula with 3% Bemotrizinol and 1% polymer

Phase	Ingredient	% w/w
A	Water	87.80
	Carbomer (polyacrylic acid)	0.30
B	Bemotrizinol	3.00
	Phenethyl Benzoate	4.00
	Cetearyl alcohol, dicetyl phosphate , ceteth-10 phosphate	3.00
	Vinylpyrrolidone/Eicosene copolymer	1.00
C	Sodium hydroxide 10% solution	0.90
	Total	100.00

Table 2-3. Composition of the sunscreen formula with 6% Bemotrizinol.

Phase	Ingredient	% w/w
A	Water	81.80
	Carbomer (polyacrylic acid)	0.30
B	Bemotrizinol	6.00
	Phenethyl Benzoate	8.00
	Cetearyl alcohol, dicetyl phosphate , ceteth-10 phosphate	3.00
C	Sodium hydroxide 10% solution	0.90
	Total	100.00

Sample preparation for SPF measurement – 32 mg (1.28 mg/cm^2) of sunscreen material was applied to the roughened side of a PMMA plate using a micro balance to monitor the weight. First, the product was evenly distributed as a large number of small droplets of approximately equal volume over the surface of the plate. Next, the sunscreen product was spread immediately over the whole surface using light strokes with a finger-cot. Spreading was completed in two phases: (a) the product was first distributed over the entire plate using light pressure and small circular motion in <15 s and (b) the distributed sample was then rubbed with larger circular motion until 14 ± 0.5 mg of product is left on plate. Finished plates were then allowed to equilibrate in the dark, at ambient temperature, for at least 30 min to set up the product film before measurement.

Sample preparation for DEET measurement

The following polymers were added to the OFF! Deep Woods product by SC Johnson: S2000 (Ganex Sensory - VP/acrylates/lauryl methacrylate copolymer), ES425 (Gantrez ES 425 - Butyl ester of PVM/MA copolymer), G904 (Ganex P-904 LC - Butylated PVP), and P100 (Ultrathix P-100 - Acrylic Acid/VP Crosspolymer). Each polymer was added at 1% (w/w) to the OFF product and mixed until completely dissolved.

2.3 Methods

UV-vis absorption and fluorescence spectroscopy

Absorbance measurements were recorded with a double beam Varian UV-vis Spectrophotometer using a 1 cm pathlength quartz cuvette. Fluorescence data were acquired with a Varian Cary Eclipse Fluorescence Spectrophotometer.

Time-resolved absorption spectroscopy

The laser system consists of a Spectra-Physics Tsunami oscillator and a home built Ti:sapphire amplifier producing 70 fs pulses at 795 nm. The amplifier output was split to generate two independently tunable pump and probe pulses. The pump beam (~3.5 mW, 350 nm) was produced by a noncollinear optical parametric amplifier (Topas White Light Conversion) and modulated at 17 Hz by a mechanical chopper. The probe beam was delayed with respect to the pump beam by a computer controlled stage. The polarization of the pump to probe beam was set at the “magic angle”. The sample was placed in 1 cm quartz cuvette. The probe light was detected with a Si photodiode detector. The configuration of the experiment is shown in Figure 2-3.

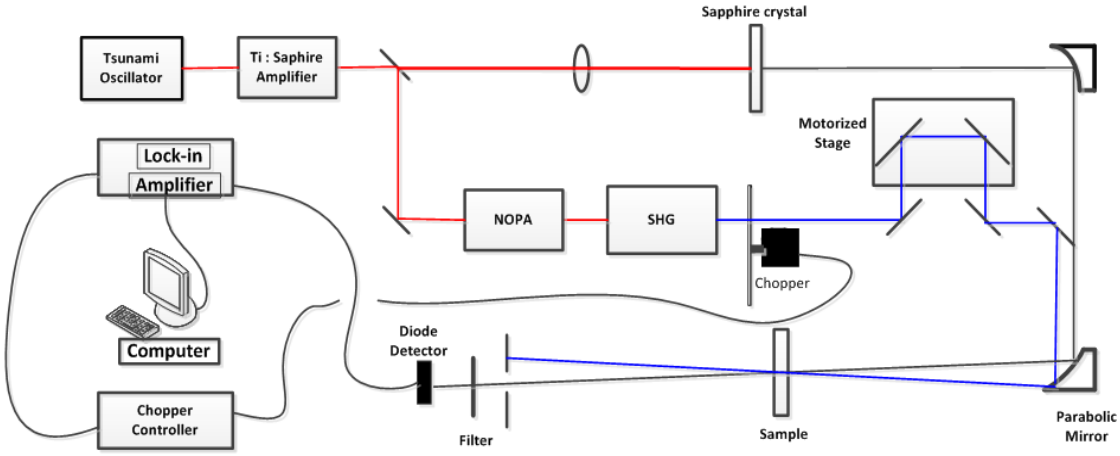

Figure 2-3. Configuration of the time-resolved experiment set up.

Confocal Raman Measurement

(A) Instrumentation

Confocal Raman microscopy was done using a WITec Alpha-300R Plus confocal Raman microscope (Ulm, Germany) equipped with a 532 nm laser. A 100X oil immersion objective (NA 1.25) was used to create a tight focus to achieve good spatial resolution. All measurements were performed at room temperature. For the DEET permeation experiment, each skin sample section was imaged as a rectangular section (50 x 40 μm^2 in the XZ plane), using 2 μm steps and a 7s integration time with the laser power set at 15 mW. For the bemotrizinol permeation experiment, each skin sample was imaged as a rectangular section (100 x 60 μm^2 in the XZ plane), using 2 μm steps and a 10s integration time with a laser power of 20 mW.

(B) Data Analysis

Data analysis was accomplished using WITec Project Plus 4.1 software. The software offers various tools to extract the information of interest. The data were first treated to remove cosmic rays and smoothed (Project Plus software option with a filter size of 3 and 8 for dynamic factor) followed by baseline subtraction (Project Plus software option with shape size of 120 and noise factor of 1). During confocal Raman image scans, a full Raman spectrum is recorded at each image point or pixel; therefore, images can be generated for any spectral marker or ratios.

Multivariate data analysis was also used for image generation in the confocal Raman studies. The Cluster Analysis option (k-means without background, Euclidean normalization and distance) was applied. In cluster analysis, spectra in the data set are grouped according to their similarities. An average spectrum of each cluster is generated along with an image of color-coded clusters.

Images of the distribution of DEET within the SC were generated from the ratio of the signal intensity of each marker band to the endogenous Amide I intensity in skin. Signature skin bands such as the Amide I (peptide bond C=O stretch, at ~1650 cm^{-1} in the SC), CH_2 and CH_3 stretch (2800-3000 cm^{-1}) and OH stretch (3100-3600 cm^{-1}) are often used as marker band for protein, lipids or water, respectively, in the skin. Specifically, 2880/2930 cm^{-1} is used to delineate SC from the viable epidermis (VE). In Raman spectra of the skin, the 2880 cm^{-1} peak arises predominantly from the asymmetric methylene stretching mode of

the lipid acyl chains and the methyl band (2930 cm^{-1}) from the SC protein[1]. Since the lipid content is reduced going from the SC to the VE, this parameter is used to determine the boundary[2-3] as outlined in Figure 2-4.

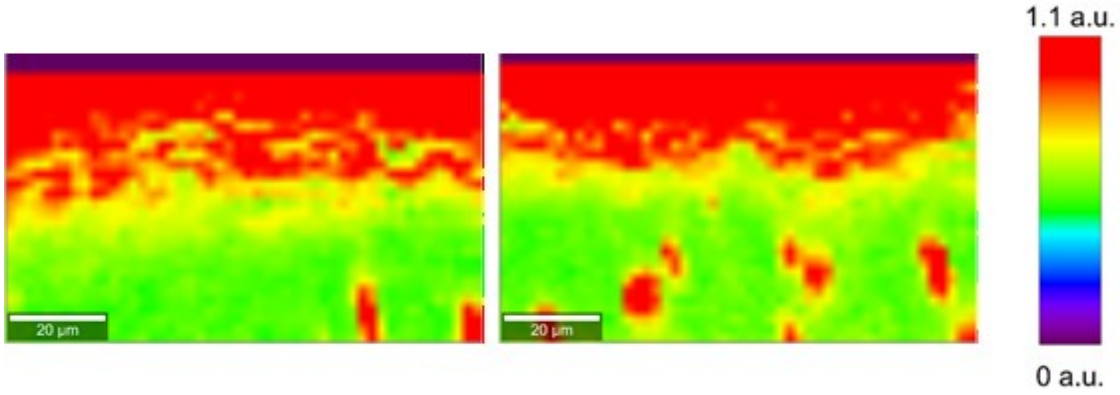

Figure 2-4. Ratio of the 2880/2930 bands of untreated skin to show SC/VE boundary.

The bands at 1048 cm^{-1} and 1505 cm^{-1} were used as marker bands for Bemotrizinol since they did not overlap with endogenous skin bands. Images of the distribution of Bemotrizinol within the SC were generated from the ratio of the signal intensity of each marker band cited above to the Amide I intensity within the SC. The bands at 522 cm^{-1} and 687 cm^{-1} served as marker bands for DEET. Similarly, images of the distribution of DEET within the SC were generated from the ratio of the signal intensity of each marker band cited above to the Amide I intensity within the SC.

The images generated from the above protocols were also manipulated to remove pixels that had a low signal to noise ratio (S/N). The software allows us

to specify any S/N level creating binary images (masks). One can specify the S/N in the mask which can be used to exclude pixels in the final image. This was done by evaluating the noise intensity level in a wavenumber region where there are no Raman bands. A ratio is then generated using a known Raman band of the skin, such as, the protein Amide I band having a fairly homogeneous spatial distribution over the noise intensity. For our noise filter, we used the ratio of the Amide I intensity to the maximum peak height in the 2000 cm^{-1} to 2300 cm^{-1} region with a signal-to-noise factor greater than 10 to mask out the pixels with a high noise level from the final image.

SPF measurement

SPF measurements were done using the Labsphere UV-2000S instrument. The UV-2000S instrument is the industry standard for measuring in-vitro SPF/UVA analysis of sunscreen samples. The UV-2000S measures the diffuse transmittance of sunscreen samples in the ultraviolet wavelength region from 250 nm – 450 nm [4]. The instrument comes with license-controlled UV-2000S Software that allows the user to choose different in-vitro measurement methods for UVA/UVB protection factors of sunscreen including the COLIPA, Boots Star and FDA methods[5].

2.4 References II

1. Pyatski, Y.; Zhang, Q.; Mendelsohn, R.; Flach, C. R., Effects of permeation enhancers on flufenamic acid delivery in Ex vivo human skin by confocal Raman microscopy. *International Journal of Pharmaceutics* **2016,** *505* (1–2), 319-328.
2. Choe, C.; Lademann, J.; Darvin, M. E., Lipid organization and stratum corneum thickness determined in vivo in human skin analyzing lipid-keratin peak (2820-3030 cm-1) using confocal Raman microscopy. *J. Raman Spectrosc.* **2016,** *47* (11), 1327-1331.
3. Janssens, M.; van Smeden, J.; Puppels, G. J.; Lavrijsen, A. P. M.; Caspers, P. J.; Bouwstra, J. A., Lipid to protein ratio plays an important role in the skin barrier function in patients with atopic eczema. *Br. J. Dermatol.* **2014,** *170* (6), 1248-1255.
4. Springsteen, A.; Yurek, R.; Frazier, M.; Carr, K. F., In vitro measurement of sun protection factor of sunscreens by diffuse transmittance1. *Analytica Chimica Acta* **1999,** *380* (2–3), 155-164.
5. ISO, Cosmetics - Sun protection test methods - Review and evaluation of methods to assess the photoprotection of sun protection products. *ISO/TR 26369*.

Chapter 3 Coupled Ultrafast Electron and Proton Transfer studies in a Commercial Sunscreen, Bemotrizinol.

3.1 Introduction

Sunscreen products are formulated with ingredients that either absorb or block UV radiation. These ingredients typically referred to as UV filters work by either absorbing or scattering electromagnetic radiation. The light energy absorbed by UV filters can be deactivated by a simple vibrational relaxation back to the ground state, through fluorescence or by undergoing photochemical reactions. A typical sunscreen formulation normally contains two or more sunscreen filters, the reason being that each filter has λ_{max} either in the UVA or UVB region. In order to have a continuous coverage across UVA and UVB regions, a blend of two or more filters are used to give a uniform coverage[1]. There are many UV filters available to choose from when formulating sunscreen products[2]. However, each region of the world has different requirements for the approval process and these stipulate why the use of a particular UV filter is not universal. Generally, UV filters are classified into two categories, organic and inorganic. Organic molecules are usually synthetic aromatic molecules that absorb UV radiation and release it by various mechanisms, whereas inorganic molecules are limited to titanium dioxide and zinc oxide, and these work by absorption and scattering the UV radiation.

Given the importance of these molecules to protect us from damaging UV radiation, their stability and safety are constantly being investigated[3-4]. Photostability is important for sunscreen molecules since these molecules work in cycles of constant absorption and deactivation processes. Degradation not only reduces the effectiveness of UV protection, but the product can cause other problems such as phototoxicity and photoallergy[5-6]. Therefore, by understanding the photophysical and photochemical aspects of a sunscreen molecule, these can help in the design of more photostable and efficient ones. Measurements of steady state properties, such as absorption and fluorescence are common and can help predict the efficiency of the sunscreen molecule, but understanding the photo-deactivation mechanism is also important. Until recently, the literature on ultrafast photochemistry of sunscreen molecules was limited because this event occurs on the picosecond timescale. However, the development of femotosecond laser technology now allows researchers to focus on such studies, as shown in recent work by Baker et al[7-11].

This study will focus on one UV filter, Bemotrizinol whose molecular structure is shown in Figure 3-1. Bemotrizinol is a synthetic organic molecule that absorbs in the UV region. It has two absorbance maximum peaks, one in the UV-B and one in the UV-A range, shown in Figure 3-2. The molecule has two phenolic rings connected to a central triazine ring and it is fully conjugated across the triazine center. The molecule also has two hydrophobic ethylhexyl groups connected to the phenolic rings which make it soluble in common cosmetic esters

such as phenethyl benzoate and diisopropyl adipate. The OH groups on the phenolic rings are strategically located so they can form intramolecular hydrogen bonds with the nitrogen from the center triazine ring which allows the molecule to co-exist in any one of the keto-enol configurations during excitation, Figure 3-3. The IR spectra of Bemotrizinol is shown in Figure 3-4. Since there is no carbonyl stretch peak in the 1670 – 1820 cm-1 region, it is suggested that the molecule is in the enol form in the ground state. This is further supported in the literature. Since this molecule has proton donor (-OH) and proton acceptor (-N=) groups in close proximity to each other, its electron ground state is expected to exist exclusively in the enol form because it is better stabilized by the intramolecular H-bond[12]. Such molecules undergo an intramolecular proton transfer reaction in the excited states[13]. From the data shown below, it is suggested that during photoexcitation, Bemotrizinol is deactivated by a proton-coupled electron transfer (PCET) process[14].

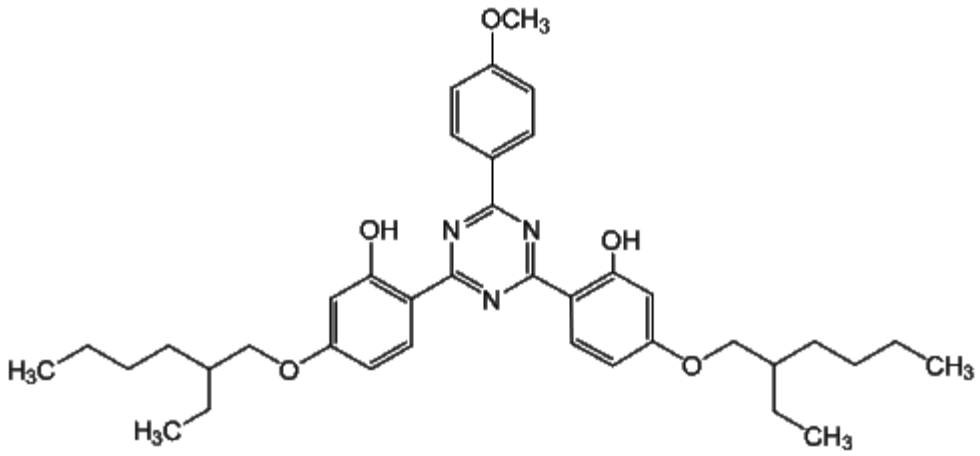

Figure 3-1. Structure of Bemotrizinol.

PCET reactions play a central role in many energy conversion processes in chemical and biological systems. Some well known examples of PCET that occur in nature are photosynthesis and respiration[15-16]. Similar reactions also take place in other man-made electrochemical processes such as fuel cells and solar cells[17-18]. During the process of PCET, an electron and a proton are transferred from a donor to an acceptor. The process can be either sequential in which the electron transfers first followed by the proton or the proton transfers first followed by the electron or, it can be concerted, where the electron and proton transfer simultaneously[19]. These processes have been reviewed as noted below and are pictured in Figure 3-5.

Over the years, numerous theoretical studies of the PCET mechanism have appeared, including many publications by Hammes-Schiffer, Soudackov, and Cukier and others on the rate constant for PCET reactions [14, 16, 20-22]. Deriving these rate expressions are challenging because of the wide range of timescales

among the solutes, protons and solvents involved, and because of the quantum behavior of the electrons, and protons. In addition, the coupling among the electron, proton and solvent must be considered. Therefore, it is difficult to provide one set rate expression because of all the different variables and diabatic states. Marcus addressed this issue of the nuclear motion and the importance of the crossing-point of the reactants' surface with the products' surface in determining the electron transfer probability by comparing the different treatments in deriving the rate constant and depending upon whether it is addressed classically or quantum mechanically[23]. Deriving the rate expression is built on the principle of a single electron transfer involving one-dimensional parabolic reaction from Marcus theory[23-24]. Single electron transfer (ET) reactions are often described in terms of two diabatic states. Similarly, a single proton (PT) reaction is described by two diabatic states. Therefore, the most basic form of a PCET reaction involving the transfer of one proton and one electron would require four diabatic states, as depicted in Figure 3-6[15, 21]. Since PCET processes involve multiple charge-transfer reactions in polar solvents[15], the free energy surface is assumed to be in the form of a two-dimensional paraboloid as demonstrated by Hammes-Schiffer et al, Figure 3-7[21].

During the process of PCET in solution triggered by photoexcitation, the two competing reactions are excited-state intramolecular proton transfer (ESIPT) and excited-state intramolecular electron transfer (ESIET)[25-26]. Depending on which reaction occurs faster, two paths for the sequential mechanism are

possible as depicted in Figure 3-5. These include one around the perimeter, and, if both processes take place simultaneously, you have the concerted process diagonally across the center[19, 27-28]. Molecules that are capable of ESIPT usually exist mostly in the enol form[29-30] and as stated earlier, Bemotrizinol is in the enol configuration in its ground state.

A closer observation of the structure of Bemotrizinol suggests the presence of pronounced charge-transfer character of the excited state. Therefore, the deactivation pathways should depend strongly on the immediate environment of the molecule[31]. We believe the molecule is in the enol configuration in the ground state and that the keto-enol tautomerization occurs during excitation, transforming the enol-excited state form to the keto-excited state form[12, 30]. The proton transfer process should be affected by the different energies of the two tautomers, which are sensitive to the polarity of the solvent[31]. Therefore, the solvent polarity should influence the dynamic of the excited state processes.

As the molecule undergoes PCET reaction, the hydroxyl proton is translocated to the triazine nitrogen as shown in Figure 3-3; the rate can lead to isotope effects on the emission yield and lifetime[32]. In the PCET reaction, the magnitude of the kinetic isotope effect (KIE) is strongly influenced by vibronic coupling. For the electronically nonadiabatic limit, the vibronic coupling is the product of the electronic coupling and the overlap between the reactant and product proton vibrational wave functions. Since the rate constant for a given pair

of vibronic states is proportional to the square of the hydrogen vibrational overlap for that pair of states at the equilibrium proton donor-acceptor distance, then it is proportional to S_H^2 and the KIE is expressed as proportional to (S_H^2/ S_D^2)[33]. This is significant to the KIE value because the mass of hydrogen is smaller than deuterium, resulting in different overlap values of their vibronic states which affect the KIE value.

A typical ESIPT molecule most often exists in the enol form because it is stabilized by intramolecular H-bonds. During photoexcitation, redistribution of the electronic charge occurs causing an increase of the acidity of the proton donor and the basicity of the proton acceptor[30]. This process generally leads to a fast proton transfer along the excited-state potential energy surface via the intramolecular H-bond. As a result, the ESIPT process leads to a tautomeric transformation from the excited enol form to the excited keto form in the sub picosecond time scale[12]. The ESIPT reaction is of particular interest since it is a very fast photophysical process and often ensures the nonradiative deactivation mechanism via a conical intersection (CI) between the excited S_1 and the ground S_0 electronic states[34].

In this study, we used ultrafast spectroscopy to study the excited state dynamics of the sunscreen molecule, Bemotrizinol, in different solvents. We focused on the rates in different media and use theoretical concepts to interpret our results. To complement our results from the femtosecond time-resolved spectroscopy, we used computational methods to further characterize the

potential energy surface (PES). The Jablonski diagram[35] typically shows the different energy reduction pathways that excited molecules can return to the ground state, but high level electronic structure calculations now allow us to understand and interpret detailed nuclear dynamics, such as IC, of these molecules. For example, conical intersections between potential energy surfaces allow us to understand population transfer between different electronic states[34, 36-38].

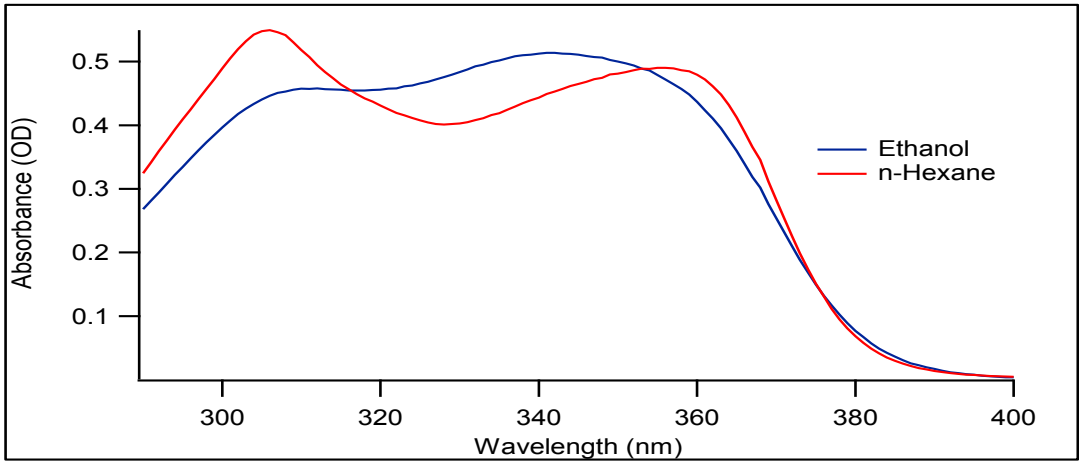

Figure 3-2. Absorbance spectra of Bemotrizinol in ethanol (blue) and n-hexane (red).

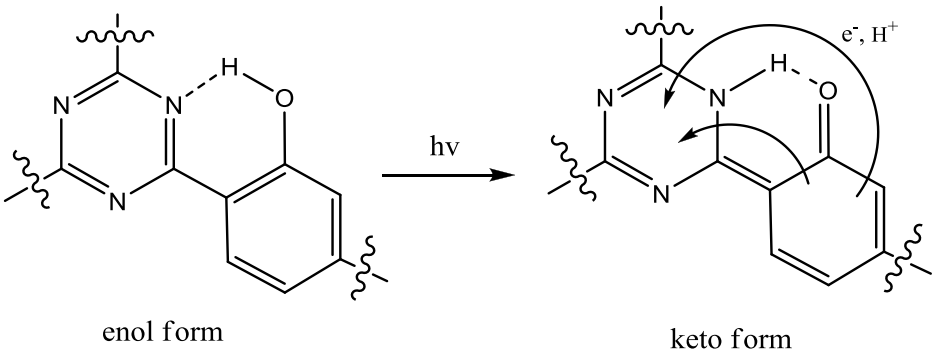

Figure 3-3. Intramolecular proton transfer reaction of Bemotrizinol that occurs in the photoexcited state.

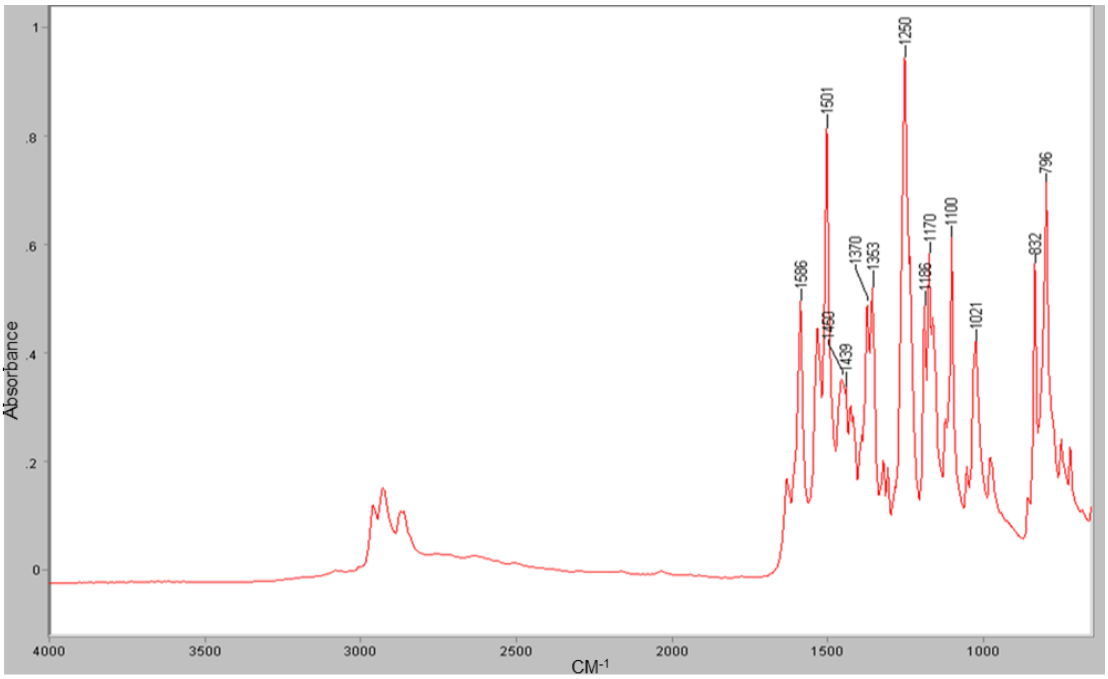

Figure 3-4. IR spectrum of Bemotrizinol.

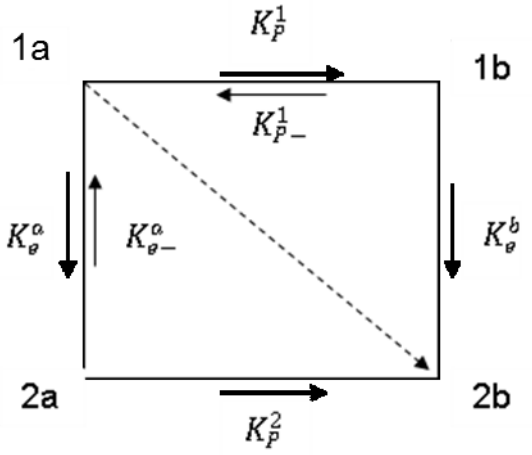

Figure 3-5. Schematic representation showing the sequential and concerted process.

(1*a*) $D_{e-}^{-} \longrightarrow {}^{+}D_P\,H \ldots\ldots A_P^{-} \longrightarrow A_e$

(1*b*) $D_{e-}^{-} \longrightarrow D_P \ldots\ldots HA_P \longrightarrow A_e$

(2*a*) $D_{e-} \longrightarrow {}^{+}D_P\,H \ldots\ldots A_P^{-} \longrightarrow A_e^{-}$

(2*b*) $D_{e-} \longrightarrow D_P \ldots\ldots HA_P \longrightarrow A_e^{-}$

Figure 3-6. General Scheme of a PCET.

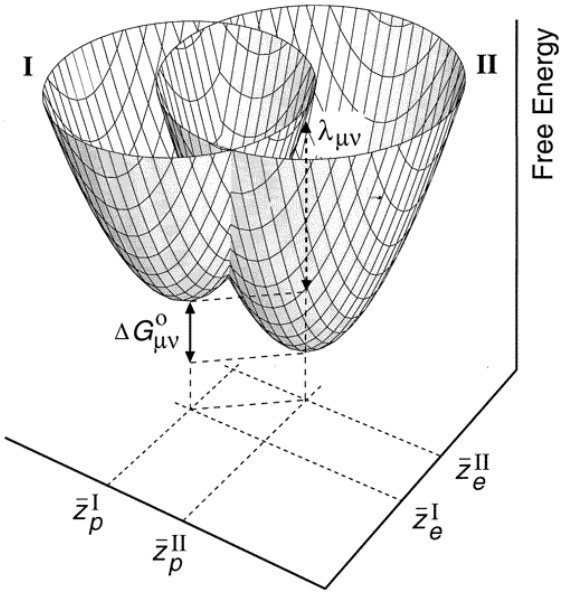

Figure 3-7. Schematic illustration of two-dimensional paraboloid system as a function of the solvent coordinates Z_p and Z_e [21].

3.2 Results and Discussion

3.2-1. Ultrafast Spectroscopy. Bemotrizinol is an extremely stable molecule and remains stable throughout the photophysical experiments. Absorbance spectra in ethanol and n-hexane are shown in Figure 3-2. Bemotrizinol absorbs uniformly across the UVA/UVB region in both solvents with broad peaks at 306 nm and 341 nm in ethanol. The peaks in n-hexane were more defined and slightly higher at 306 nm with a red shift of the 341 nm peak to 356 nm. During the ultrafast spectroscopy study, Bemotrizinol was excited with 350 nm ~25 fs pulses to form the S_1 excited state shown in Figure 3-8A and 3-8B for Bemotrizinol in ethanol and n-hexane, respectively. The spectra in ethanol, which is a polar

solvent with dielectric constant ~25, and n-hexane, which is non-polar with dielectric constant ~2, are almost identical. Since the differences between these spectra are indistinguishable, one can assume that the solvation effect is weak because the influence of the solvents' polarity is minimal.

The transient absorbance spectra of Bemotrizinol, Figure 3-8, display absorbance of the probe pulse in the range of 475-650 nm with an absorbance maximum centered at 596 nm. Displacement of the transient absorbance was observed with variation in life times, which suggests the molecule goes through a process of vibrational cooling during depopulation at the ground state. Vibrational cooling is the process by which the molecule, after photoexcitation, relaxes to the ground state vibrational manifold while transferring the excess energy to the solvent[39].

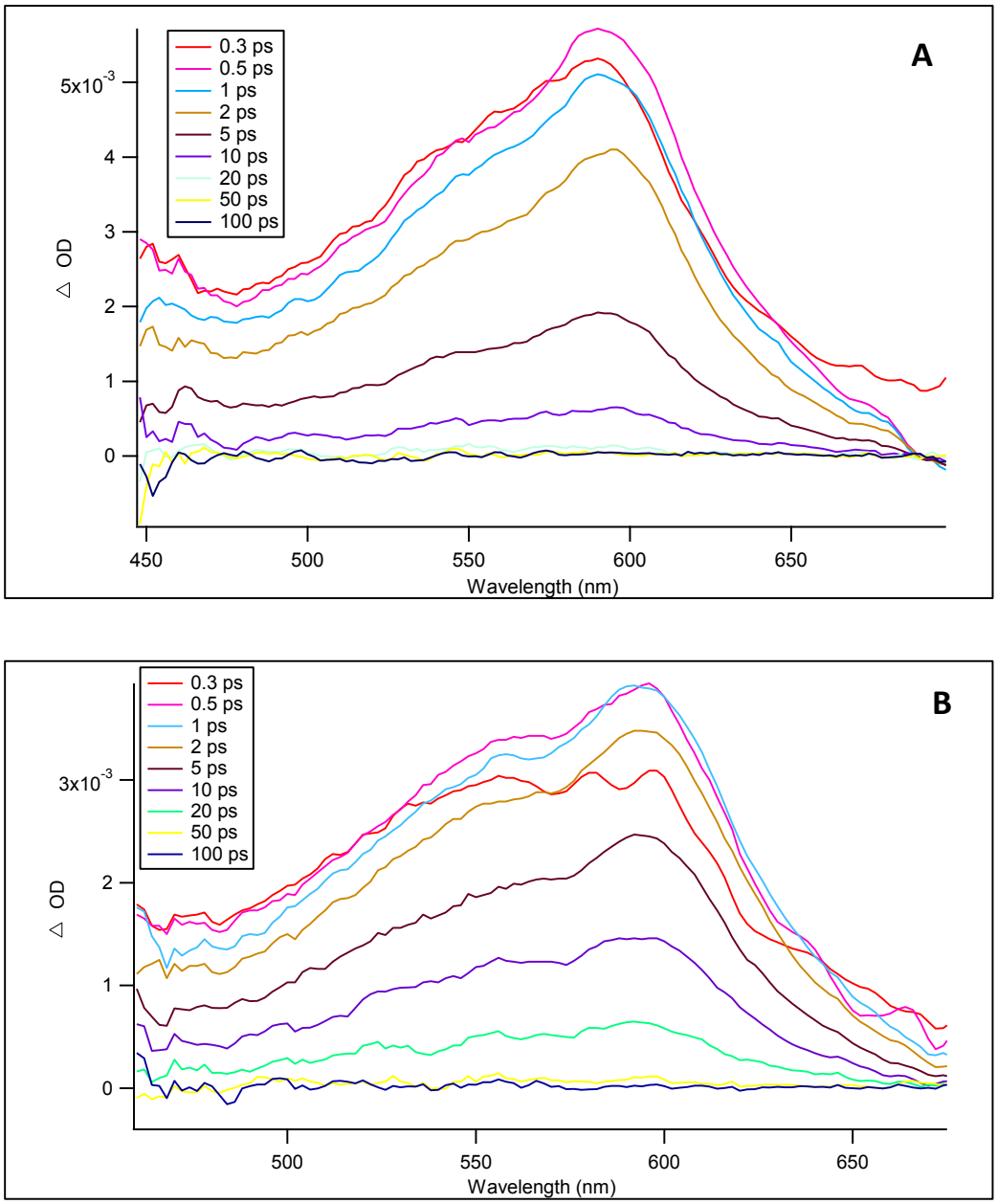

Figure 3-8. Femotsecond pump-probe transient absorption spectra of Bemotrizinol excited state in (A) ethanol, (B) n-hexane.

Dynamic measurements of Bemotrizinol were carried out in ethanol, ethanol-d_6, n-hexane, n-hexadecane, lauryl lactate and acetonitrile solutions. The transient of the decay profiles of Bemotrizinol in ethanol and ethanol d_{-6} are shown in Figure 3-9, whereas the decay profile in n-hexane and in n-hexadecane are shown in Figure 3-10. The dynamics of deuterated Bemotrizinol were also measured in n-hexadecane. The transient of the decay profile is compared with the non-deuterated form of the molecule as shown in Figure 3-11. Bemotrizinol has a short excited lifetime in the solvents investigated. We also found that the excited states decay is double exponential. The raw data were fitted with double exponentials and τ_1, A_1 and τ_2, A_2 values were extracted for the various solvents investigated. These are shown in Table 3-1. A plot of the results for the excited state decay in ethanol along with the double exponential function is shown in Figure 3-12. The decay profile of ethanol is plotted in red while the double exponential function is shown in black. The experimental data for Bemotrizinol aligned almost perfectly with the double exponential function. A similar exponential fit was observed for Bemotrizinol in the other solvents investigated.

Interpretation of the results from the decay profile in different solvents provides a better understanding of the photochemistry of Bemotrizinol. First, the isotope effect can be readily observed from the different transient decay profiles between ethanol and ethanol-d_6 as shown in Figure 3-9. Analysis revealed that τ_1 increased from 3.6 ps in ethanol to 4.6 ps in ethanol-d_6 while τ_2 changed from 10.4 ps to 16 ps. This is in agreement with what one would expect for a concerted

PCET reaction exhibiting KIE because such reaction involves an atom tunneling event and, because of the reduced tunneling probability of the heavier deuteron[40], we expect to see a difference in the τ_1 and τ_2 values in ethanol and ethanol-d_6. The results so far indicate that the reaction followed a PCET process.

We evaluated the effect of the viscosity of the solvent on the lifetimes by measuring the dynamics in n-hexane and n-hexadecane as shown in Figure 3-10. We observed $\tau 1$ goes from 6.4 ps to 8.3 ps and τ_2 goes from 15.6 ps to 20.3 ps when measured in n-hexane to n-hexadecane, respectively. Our results showed small changes in the τ_1 and τ_2 values going from n-hexane to n-hexadecane; however, these changes are consistent with what one would expect for a process where the micro environment of the molecule can affect its movement. This ultimately affects the solvent organization energy (λ), the electron exchange matrix element (V) and ΔG^o which contribute to the rate expression[16, 41-42]. Differences in the lifetimes values for n-hexane and n-hexadecane are clearly the effect of the viscosity differences between the solvents. This is further supported in that the ratios of τ_1 and τ_2 are the same in both solvents and both solvents are non polar with similar dielectric constants.

In addition, Decornez et al provided theoretical calculations showing that if solvent polarity is reduced, the decrease in the reorganization energies lead to a lower barrier along the solvent coordinates, which increases the rate[14]. Since the corresponding rate constant $k_1 = 1/\tau_1$, our experimental results are consistent

with the theoretical description in that increasing τ_1 and τ_2 values are observed from ethanol to n-hexane.

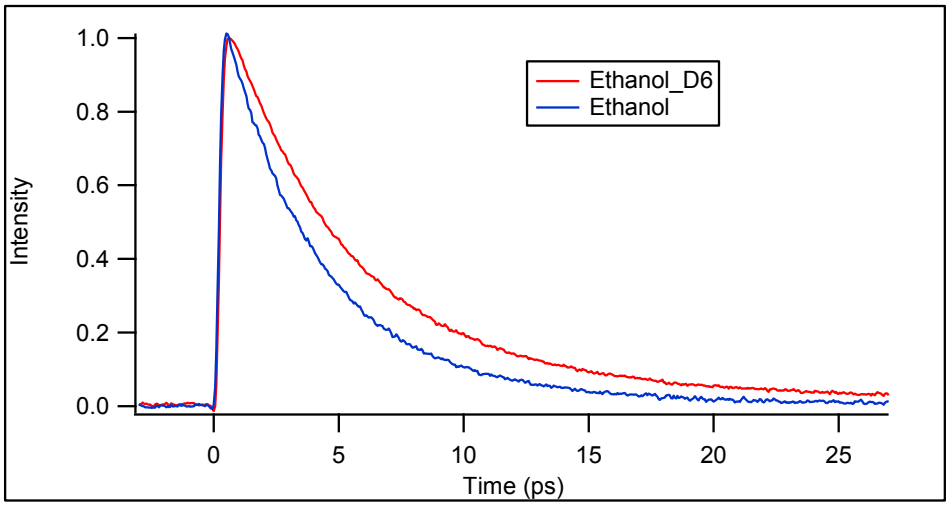

Figure 3-9. Decay profiles of Bemotrizinol in ethanol d-6 (blue line) and ethanol (red line).

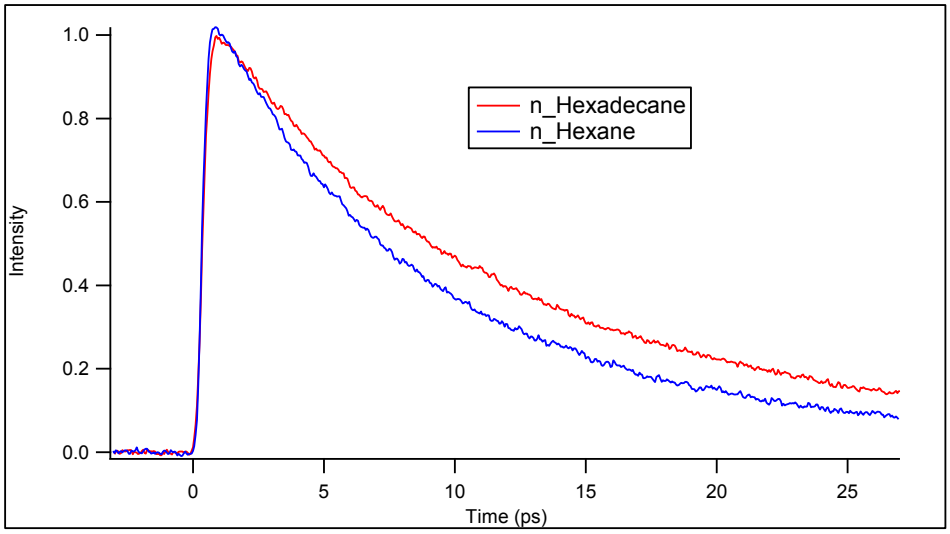

Figure 3-10. Decay profile of Bemotrizinol in n-hexadecane (red line) and n-hexane (blue line).

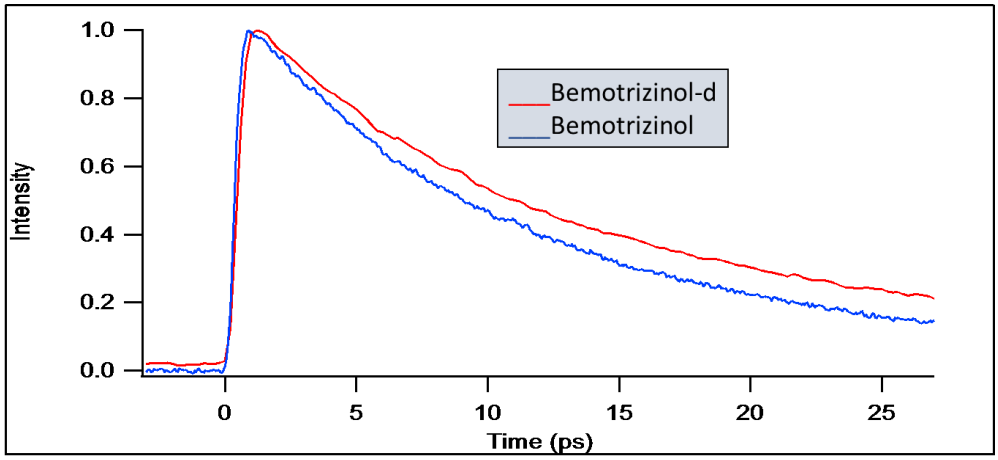

Figure 3-11. Decay profile of deuterated Bemotrizinol (red line) compared to Bemotrizinol (blue line) in n-hexadecane.

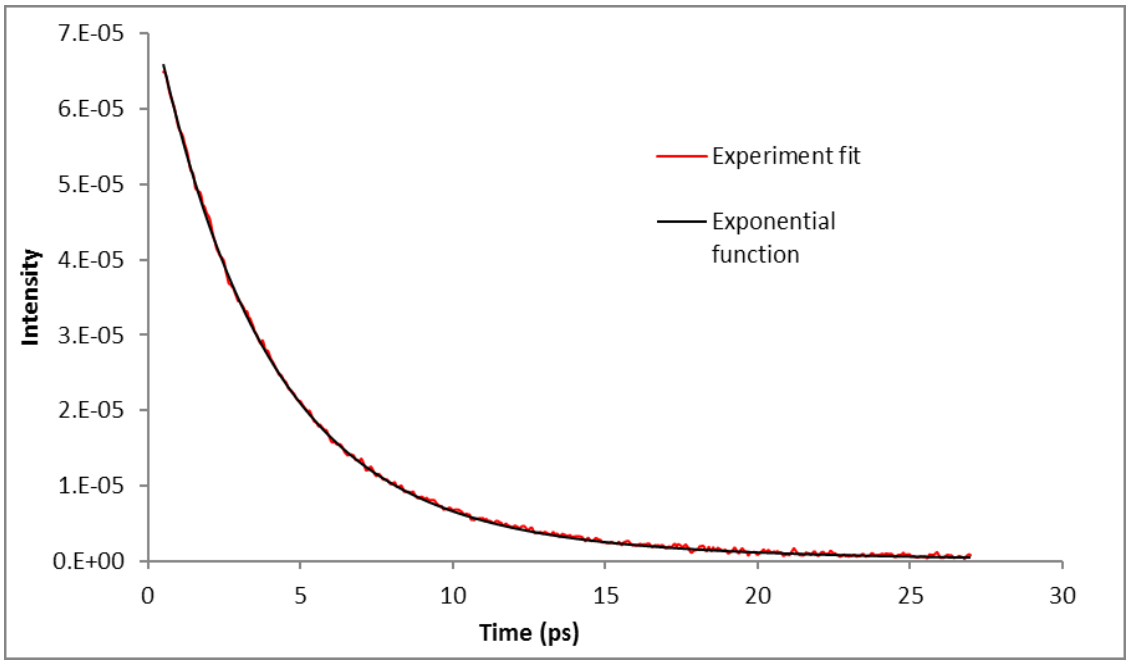

Figure 3-12. Experimental results for the excited state decay in ethanol (red) along with the double exponential function (black).

To further probe the isotope and viscosity effects from the molecular perspective, Bemotrizinol was deuterated and its dynamics in n-hexadecane was measured. The data are compared with the non-deuterated form of the molecule in Figure 3-11. The τ_1 and τ_2 values both increased for deuterated Bemotrizinol when compared to Bemotrizinol in n-hexadecane. These are among the highest τ_1 and τ_2 values observed for these experiments. The data agreed with the results obtained from the two prior experiments. The latter values increase from ethanol to ethanol d6 and from n-hexane to n-hexadecane. Therefore, these values, being amongst the highest τ_1 and τ_2 values observed in these experiments, arise because you have both the isotope and the viscosity effects in the same experiment.

It is important to understand whether the reaction for Bemotrizinol proceeds by a sequential or concerted pathway. In principle, the KIE can be used to probe whether the mechanism is concerted or sequential. Also Mayer et al[19] referred to PCET as a single chemical reaction step involving a concerted transfer of both a proton and an electron. For Bemotrizinol, we observed the KIE in ethanol and ethanol d_6 and the KIE of deuterated Bemotrizinol in n-hexadecane; therefore, we can conclude that the reaction proceeds through the concerted pathway.

Table 3-1. Summary of the different lifetime values of Bemotrizinol in various solvents

Solvent	**τ_1(ps)**	**A_1**	**τ_2 (ps)**	**A_2**
Ethanol	3.57±0.03	0.91	10.40±0.55	0.09
Ethanol D-6	4.59±0.05	0.88	16.02±0.00	0.12
n-Hexane	6.38±0.22	0.63	15.65±0.88	0.37
n-Hexadecane	8.27±0.41	0.60	20.31±1.69	0.40
Deuterated Bemotrizinol in n-Hexadecane	8.97±0.55	0.61	31.42±4.15	0.39
Acetonitrile	1.51±0.00	0.95	56.26±5.57	0.05
Lauryl Lactate	5.62±0.24	0.60	45.48±4.87	0.40

Table 3-2. Viscosity and dielectric constant of various solvents

Solvent	**Viscosity (cP) at 25$^{\upsilon}$C**	**Dielectric constant**
Ethanol	1.26	25.04
n-Hexane	0.30	1.89
n-Hexadecane	3.04	2.09
Acetonitrile	0.37	36.7

3.2-2. Computational Calculations. In the second part of this study, we utilized Hartree-Fock UH/UHF 6-31G* calculations to obtain the potential energy surfaces for the excited S_1 and the ground S_0 electronic states. The potential energy profiles for these states are shown in Figure 3-13. Bemotrizinol, structure shown in Figure 3-1, was too large for the method to converge; therefore, the size

of the molecule was reduced and calculations were based on the main fragment of the molecule containing a central triazine ring with only one methoxyphenol group as shown in Figure 3-14.

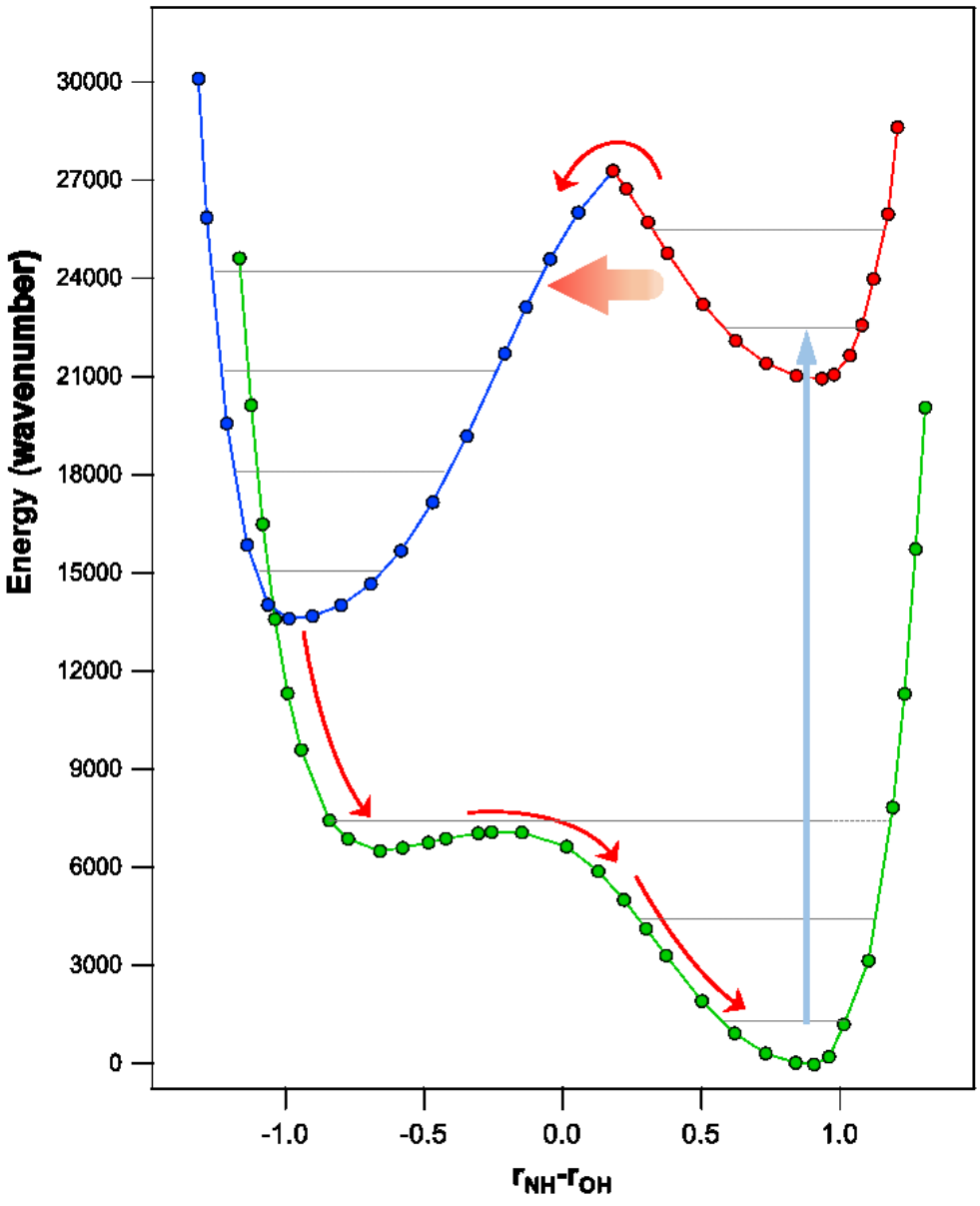

Figure 3-13. Potential energy profiles of the S_0 and S_1 states from the Hartree-Fock UH/UHF 6-31G* calculations for structure shown in Figure 3-14.

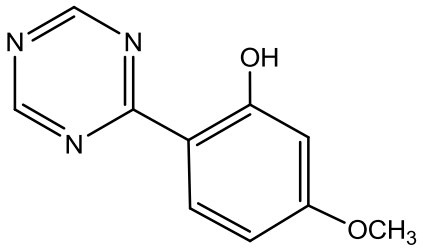

Figure 3-14. Structure used for Hartree-Fock UH/UHF 6-31G* calculations.

The potential energy profiles shown in Figure 3-13, along with results from transient absorption spectroscopy, provide valuable information to unravel the excited states' energy dissipation mechanism of Bemotrizinol. The x-axis indicates the position of the proton at r_{NH} and r_{OH} to ~1 Å and the y-axis is the energy expressed in cm^{-1}. The ground state PES (S_0) is shown in green circles and the excited state PES (S_1) is shown in red and blue circles. Following photoexcitation, the molecule is promoted to the excited states. This electronic excitation is then transferred into vibrations which involves successive ultrafast steps beginning with IC to the $1\pi\pi^*$ S_1 excited state potential energy surface, red circles. The path then follows the red arrow toward the S_1 and S_0 conical intersection undergoing ultrafast enol → keto tautomerization (ESIPT and ESIET) on the S_1 potential energy surface (PES), blue circles. After this intramolecular electron-driven hydrogen atom transfer, which drives enol → keto tautomerization, a slower rotation about the C–C bond may occur which facilitates IC back to the S_0 state through the S_1/S_0 conical intersection, blue and green circles. We associate this process with the lifetime τ_1 value obtained from the

decay profile in ultrafast spectroscopy. Similar studies can be found for comparable systems undergoing enol →keto tautomerization in the literature[43-46]

After passing through the S_1/S_0 CI, the keto molecule is now in a vibrational excited S_0 state. At this point, ground state hydrogen transfer takes place to restore the enol tautomer. The enol tautomer subsequently cools via vibrational energy transfer (VET) with the surrounding solvent and this process is attributed to the τ_2 life time value obtained from the pump probe experiments following the same convention as the τ_1 above. The absorption feature from the transient absorbance spectra of Bemotrizinol, Figure 3-8, centered at 596 nm reflects this last step, as vibrational excited molecules in the S_0 state absorb the white light probe[10].

So far, we looked at the PES profiles and broke down the energy deactivation mechanism of Bemotrizinol by *ab initio* calculations and previous ultrafast measurements. We assigned the τ_1 and τ_2 rates to the mechanism. We will use this assignment to account for the difference in the lifetime τ_1 between solvents. Firstly, we try to understand through differences in the solvent viscosity by focusing mainly on the S_1 PES. n-Hexadecane has higher viscosity compared to n-hexane (3.04 and 0.30 cP, respectively) and is therefore likely to have more friction to the geometry change required before Bemotrizinol can couple to its S_0 state thus returning a higher τ_1 value than n-hexadecane. Secondly, let us focus on the effect of deuteration. It is expected that deuterated Bemotrizinol will have a higher barrier to overcome at the conical intersection on the red and blue circles

on the S_1 PES, therefore reflecting higher τ_1 values in ethanol-d-6 than in ethanol and also for deuterated Bemotrizinol in n-hexadecane. The main reason for this KIE effect is because deuterated Bemotrizinol will have a higher activation energy to overcome because of its lower zero-point energy, thus returning a longer τ_1 value. The lifetime values also display solvent dependence. The τ_2 value is shorter in more polar solvents such as ethanol compared to n-hexadecane. This agrees with the VET-driven cooling process where τ_2 is assigned. A more polar solvent has a greater degree of hydrogen bonding therefore enhancing VET.

3.3 Conclusion

Bemotrizinol has a short excited lifetime in the picosecond range. This helps to explain why the molecule is extremely stable under UV conditions. Our results also show strong dependence of the excited states on solvent polarity as you go from ethanol to n-hexadecane and solvent viscosity as in n-hexane and n-hexadecane. Most important is the H/D isotope effect confirming the reaction followed the concerted pathway between the OH group of the phenol and the central triazine ring. Using the ultrafast spectroscopy results coupled with computational calculations further allowed us to fully understand the energy dissipation mechanism. Following excitation, involves successive ultrafast steps beginning with IC and a series of ultrafast enol-keto tautomerization. Then a CI aids the transfer to the ground electronic state. Subsequent collisions with the solvent bath then reforms the original enol-tautomer. This dominant mechanism is responsible for its stability and the efficient photoprotection it offers. Going

forward with the challenge to make a perfect UV filter, the concept of a multifunctional UV filter has already been anticipated, such as a photostabilizer with antioxidant functionality[47-51]. Our findings also have important practical implications for the design of superior sunscreens, which must combine high UV absorptivity with the ability to rapidly dissipate the absorbed energy via reversible, nonreactive channels.

3.4 References III

1. Lhiaubet-Vallet, V.; Marin, M.; Jimenez, O.; Gorchs, O.; Trullas, C.; Miranda, M. A., Filter-filter interactions. Photostabilization, triplet quenching and reactivity with singlet oxygen. *Photochem. Photobiol. Sci.* **2010,** *9* (4), 552-558.
2. Shaath, N. A., Ultraviolet filters. *Photochem. Photobiol. Sci.* **2010,** *9* (4), 464-469.
3. Sayre, R. M.; Dowdy, J. C.; Gerwig, A. J.; Shields, W. J.; Lloyd, R. V., Unexpected photolysis of the sunscreen octinoxate in the presence of the sunscreen avobenzone. *Photochem. Photobiol.* **2005,** *81* (Mar./Apr.), 452-456.
4. Kockler, J.; Oelgemöller, M.; Robertson, S.; Glass, B. D., Photostability of sunscreens. *Journal of Photochemistry and Photobiology C: Photochemistry Reviews* **2012,** *13* (1), 91-110.
5. Naylor, M. F.; Farmer, K. C., The case for sunscreens. A review of their use in preventing actinic damage and neoplasia. *Arch Dermatol* **1997,** *133* (9), 1146-54.
6. Darvay, A.; White, I. R.; Rycroft, R. J.; Jones, A. B.; Hawk, J. L.; McFadden, J. P., Photoallergic contact dermatitis is uncommon. *Br J Dermatol* **2001,** *145* (4), 597-601.
7. Baker, L. A.; Clark, S. L.; Habershon, S.; Stavros, V. G., Ultrafast Transient Absorption Spectroscopy of the Sunscreen Constituent Ethylhexyl Triazone. *J. Phys. Chem. Lett.* **2017,** *8* (10), 2113-2118.
8. Baker, L. A.; Greenough, S. E.; Stavros, V. G., A Perspective on the Ultrafast Photochemistry of Solution-Phase Sunscreen Molecules. *J. Phys. Chem. Lett.* **2016,** *7* (22), 4655-4665.
9. Baker, L. A.; Horbury, M. D.; Greenough, S. E.; Allais, F.; Walsh, P. S.; Habershon, S.; Stavros, V. G., Ultrafast Photoprotecting Sunscreens in Natural Plants. *J. Phys. Chem. Lett.* **2016,** *7* (1), 56-61.
10. Baker, L. A.; Horbury, M. D.; Greenough, S. E.; Coulter, P. M.; Karsili, T. N. V.; Roberts, G. M.; Orr-Ewing, A. J.; Ashfold, M. N. R.; Stavros, V. G., Probing the Ultrafast Energy Dissipation Mechanism of the Sunscreen Oxybenzone after UVA Irradiation. *J. Phys. Chem. Lett.* **2015,** *6* (8), 1363-1368.

11. Baker, L. A.; Grosvenor, L. C.; Ashfold, M. N. R.; Stavros, V. G., Ultrafast photophysical studies of a multicomponent sunscreen: Oxybenzone–titanium dioxide mixtures. *Chemical Physics Letters* **2016,** *664* (Supplement C), 39-43.
12. Kwon, J. E.; Park, S. Y., Advanced Organic Optoelectronic Materials: Harnessing Excited-State Intramolecular Proton Transfer (ESIPT) Process. *Adv. Mater. (Weinheim, Ger.)* **2011,** *23* (32), 3615-3642.
13. Chou, P. T.; Martinez, M. L.; Clements, J. H., Reversal of excitation behavior of proton-transfer vs. charge-transfer by dielectric perturbation of electronic manifolds. *J. Phys. Chem.* **1993,** *97* (11), 2618-22.
14. Decornez, H.; Hammes-Schiffer, S., Model Proton-Coupled Electron Transfer Reactions in Solution: Predictions of Rates, Mechanisms, and Kinetic Isotope Effects. *J. Phys. Chem. A* **2000,** *104* (41), 9370-9384.
15. Soudackov, A.; Hammes-Schiffer, S., Multistate continuum theory for multiple charge transfer reactions in solution. *J. Chem. Phys.* **1999,** *111* (10), 4672-4687.
16. Cukier, R. I.; Nocera, D. G., Proton-coupled electron transfer. *Annual review of physical chemistry* **1998,** *49*, 337-69.
17. Gratzel, M., Photoelectrochemical cells. *Nature* **2001,** *414* (6861), 338-44.
18. Lewis, N. S.; Nocera, D. G., Powering the planet: chemical challenges in solar energy utilization. *Proceedings of the National Academy of Sciences of the United States of America* **2006,** *103* (43), 15729-35.
19. Mayer, J. M.; Rhile, I. J., Thermodynamics and kinetics of proton-coupled electron transfer: stepwise vs. concerted pathways. *Biochimica et Biophysica Acta (BBA) - Bioenergetics* **2004,** *1655*, 51-58.
20. Soudackov, A.; Hammes-Schiffer, S., Derivation of rate expressions for nonadiabatic proton-coupled electron transfer reactions in solution. *J. Chem. Phys.* **2000,** *113* (6), 2385-2396.
21. Hammes-Schiffer, S., Theoretical Perspectives on Proton-Coupled Electron Transfer Reactions. *Acc. Chem. Res.* **2001,** *34* (4), 273-281.
22. Hammes-Schiffer, S.; Soudackov, A. V., Proton-Coupled Electron Transfer in Solution, Proteins, and Electrochemistry. *J. Phys. Chem. B* **2008,** *112* (45), 14108-14123.
23. Marcus, R. A.; Eyring, H., Chemical and electrochemical electron-transfer theory. *Annu. Rev. Phys. Chem.* **1964,** *15*, 155-96.
24. Marcus, R. A.; Sutin, N., Electron transfers in chemistry and biology. *Biochim. Biophys. Acta, Rev. Bioenerg.* **1985,** *811* (3), 265-322.
25. Hsieh, C.-C.; Jiang, C.-M.; Chou, P.-T., Recent Experimental Advances on Excited-State Intramolecular Proton Coupled Electron Transfer Reaction. *Acc. Chem. Res.* **2010,** *43* (10), 1364-1374.
26. Kretchmer, J. S.; Miller, T. F., Tipping the Balance between Concerted versus Sequential Proton-Coupled Electron Transfer. *Inorg. Chem.* **2016,** *55* (3), 1022-1031.
27. Savarese, M.; Bremond, E.; Adamo, C.; Rega, N.; Ciofini, I., Excited-State Proton Transfer and Intramolecular Charge Transfer in 1,3-Diketone Molecules. *ChemPhysChem* **2016,** *17* (10), 1530-1538.
28. Luber, S.; Adamczyk, K.; Nibbering, E. T. J.; Batista, V. S., Photoinduced Proton Coupled Electron Transfer in 2-(2'-Hydroxyphenyl)-Benzothiazole. *J. Phys. Chem. A* **2013,** *117* (25), 5269-5279.

29. Wilbraham, L.; Savarese, M.; Rega, N.; Adamo, C.; Ciofini, I., Describing Excited State Intramolecular Proton Transfer in Dual Emissive Systems: A Density Functional Theory Based Analysis. *J. Phys. Chem. B* **2015,** *119* (6), 2459-2466.
30. Goodman, J.; Brus, L. E., Proton transfer and tautomerism in an excited state of methyl salicylate. *J. Am. Chem. Soc.* **1978,** *100* (24), 7472-4.
31. Ghosh, R.; Palit, D. K., Dynamics of solvent controlled excited state intramolecular proton transfer coupled charge transfer reactions. *Photochem. Photobiol. Sci.* **2013,** *12* (6), 987-995.
32. Hazra, A.; Soudackov, A. V.; Hammes-Schiffer, S., Isotope Effects on the Nonequilibrium Dynamics of Ultrafast Photoinduced Proton-Coupled Electron Transfer Reactions in Solution. *J. Phys. Chem. Lett.* **2011,** *2* (1), 36-40.
33. Hammes-Schiffer, S.; Stuchebrukhov, A. A., Theory of Coupled Electron and Proton Transfer Reactions. *Chem. Rev. (Washington, DC, U. S.)* **2010,** *110* (12), 6939-6960.
34. Rode, M. F.; Sobolewski, A. L., Ab initio study on the excited state proton transfer mediated photophysics of 3-hydroxy-picolinic acid. *Chemical Physics* **2012,** *409*, 41-48.
35. Jablonski, A., Efficiency of anti-Stokes fluorescence in dyes. *Nature (London, U. K.)* **1933,** *131*, 839-40.
36. Fletcher, K.; Dreuw, A.; Faraji, S., Potential energy surfaces and approximate kinetic model for the excited state dynamics of Pigment Yellow 101. *Computational and Theoretical Chemistry* **2014,** *1040-1041*, 177-185.
37. Sobolewski, A. L.; Domcke, W., Photophysics of intramolecularly hydrogen-bonded aromatic systems: ab initio exploration of the excited-state deactivation mechanisms of salicylic acid. *Phys. Chem. Chem. Phys.* **2006,** *8* (29), 3410-3417.
38. Karsili, T. N. V.; Marchetti, B.; Ashfold, M. N. R.; Domcke, W., Ab Initio Study of Potential Ultrafast Internal Conversion Routes in Oxybenzone, Caffeic Acid, and Ferulic Acid: Implications for Sunscreens. *J. Phys. Chem. A* **2014,** *118* (51), 11999-12010.
39. Abid, A. R.; Marciniak, B.; Pedzinski, T.; Shahid, M., Photo-stability and photo-sensitizing characterization of selected sunscreens' ingredients. *J. Photochem. Photobiol., A* **2017,** *332*, 241-250.
40. Zhang, W.; Burgess, I. J., Kinetic isotope effects in proton coupled electron transfer. *J. Electroanal. Chem.* **2012,** *668*, 66-72.
41. Shafirovich, V. Y.; Courtney, S. H.; Ya, N.; Geacintov, N. E., Proton-Coupled Photoinduced Electron Transfer, Deuterium Isotope Effects, and Fluorescence Quenching in Noncovalent Benzo[a]pyrenetetraol-Nucleoside Complexes in Aqueous Solutions. *J. Am. Chem. Soc.* **1995,** *117* (17), 4920-9.
42. O'Connor, D.; Shafirovich, V. Y.; Geacintov, N. E., Influence of Adduct Stereochemistry and Hydrogen-Bonding Solvents on Photoinduced Charge Transfer in a Covalent Benzo[a]pyrene Diol Epoxide-Nucleoside Adduct on Picosecond Time Scales. *J. Phys. Chem.* **1994,** *98* (39), 9831-9.
43. Verma, P. K.; Koch, F.; Steinbacher, A.; Nuernberger, P.; Brixner, T., Ultrafast UV-Induced Photoisomerization of Intramolecularly H-Bonded Symmetric β-Diketones. *J. Am. Chem. Soc.* **2014,** *136* (42), 14981-14989.
44. Barbatti, M.; Aquino, A. J. A.; Lischka, H.; Schriever, C.; Lochbrunner, S.; Riedle, E., Ultrafast internal conversion pathway and mechanism in 2-(2'-hydroxyphenyl)benzothiazole: a case study for excited-state intramolecular proton transfer systems. *Phys. Chem. Chem. Phys.* **2009,** *11* (9), 1406-1415.

45. Baker, L. A.; Horbury, M. D.; Greenough, S. E.; Ashfold, M. N. R.; Stavros, V. G., Broadband ultrafast photoprotection by oxybenzone across the UVB and UVC spectral regions. *Photochem. Photobiol. Sci.* **2015,** *14* (10), 1814-1820.
46. Baker, L. A.; Grosvenor, L. C.; Ashfold, M. N. R.; Stavros, V. G., Ultrafast photophysical studies of a multicomponent sunscreen: Oxybenzone-titanium dioxide mixtures. *Chem. Phys. Lett.* **2016,** *664*, 39-43.
47. Shaath, N. A., Ultraviolet filters. *Photochemical & photobiological sciences : Official journal of the European Photochemistry Association and the European Society for Photobiology* **2010,** *9* (4), 464-9.
48. Shaath, N. A.; Fares, H. M.; Klein, K., Photodegradation of sunscreen chemicals: Solvent considerations. *Cosmet. Toiletries* **1990,** *105* (12), 41-4.
49. Fang, J.-Y.; Hammes-Schiffer, S., Proton-coupled electron transfer reactions in solution: molecular dynamics with quantum transitions for model systems. *J. Chem. Phys.* **1997,** *106* (20), 8442-8454.
50. Smith, T. P.; Zaklika, K. A.; Thakur, K.; Walker, G. C.; Tominaga, K.; Barbara, P. F., Spectroscopic studies of excited-state intramolecular proton transfer in 1-(acylamino)anthraquinones. *J. Phys. Chem.* **1991,** *95* (25), 10465-75.
51. Chaudhuri, R. K.; Lascu, Z.; Puccetti, G.; Deshpande, A. A.; Paknikar, S. K., Design of a photostabilizer having built-in antioxidant functionality and its utility in obtaining broad-spectrum sunscreen formulations. *Photochemistry and photobiology* **2006,** *82* (3), 823-8.

CHAPTER 4 Confocal Raman Microscopy of a Sunscreen Cream Containing Bemotrizinol Permeation into the Stratum Corneum

4.1 Introduction

Exposure of the human skin to ultraviolet (UV) radiation is known to induce damage in the DNA and can lead to skin cancer[1-2]. Some skin cancers are linked to genetic factors, but the most common risk factor for skin cancer is exposure to UV radiation[3]. To protect the skin from such damage, a variety of sunscreen products have been developed[4-5]. Sunscreen products are formulated with ingredients that either absorb or block UV radiation. To achieve adequate protection, international standards specify that the sunscreen must be evenly applied at a level of 2mg/cm^2 over the surface of the skin[6-7]. However, the skin itself presents a major challenge for application of a uniform film because its surface appears undulating with peaks and valleys[8]. Because of these contours, sunscreen filters may not be distributed evenly during application. Creams will fill the valleys and glyphs first while leaving the peaks with a thinner film, so that overall the skin will not be evenly protected from UV radiation[7, 9]. Other than film distribution, it is also necessary to have proper dispersion and solubilization of the UV filters in the formulation to provide optimum performance. Also, some degree of the film inhomogeneity depends on the inherent physical properties of formulation including viscosity, rheology, and the film-forming ingredient used[10].

The performance of sunscreen products is rated by the labelled SPF (sun protection factor) value which reflects the protection one receives from UV radiation[11-12]. For example, an SPF of 10 indicates that if someone takes 5 minutes to develop erythema or sunburn with un-protected skin when exposed to UV radiation, then they will now take 50 minutes to develop erythema with an SPF 10 sunscreen under the same intensity of UV radiation. The types of ingredients used to formulate a sunscreen product are also important in leading to the resulting SPF value for the product. Most sunscreen emulsions are classified as either oil in water (o/w) or water in oil (w/o). A basic o/w sunscreen cream is made up of ingredients that are sunscreen actives which absorb the UV radiation, esters that are used to solubilize the actives and emulsifiers to stabilize the oil droplets in the water environment. Therefore, the o/w emulsion contains oil droplets distributed in a continuous water phase; likewise, a w/o emulsion is made up of water droplets dispersed in a continuous oil phase. If one measures the SPF of two sunscreen formulations which have identical sunscreen filters but different emulsifiers, they will get different SPF values. The different SPF values arise because the different emulsifiers affect the spreading and distribution of the sunscreen active during application, resulting in different SPF values[9, 13-16]. Similar results may arise from adding polymers to the formulations[17]. Polymers may also provide benefits such as water and rub resistance[18]. Some polymers also give an increase in the SPF value[17]. Others are added for sensory and rheological properties[19-20].

The performance of a sunscreen product is not only related to the spreading and distribution of the film upon application, but also to the photostability of the sunscreen actives[21-23]. The photochemistry of the sunscreen ingredient, Bemotrizinol, with different solvents has been reported in this thesis. The goal of the current chapter is to evaluate permeation of Bemotrizinol in a typical sunscreen formulation.

The ability to measure the molecular, structural and compositional information of a sample non-invasively is very important. Since confocal Raman microscopy (CRM) has the capability to non-invasively map the chemical properties of a sample by providing depth profiles along with molecular structure information from both the skin and the exogenous formulation, this approach was utilized to investigate film properties of a sunscreen formulation when applied to ex-vivo human skin. A simple o/w sunscreen emulsion containing one sunscreen active, Bemotrizinol, was created for this study, Table 2-1. The main ingredients are water present at ~ 90% (w/w), oil in water emulsifiers (cetearyl alcohol, dicetyl phosphate, ceteth-10 phosphate), phenethyl benzoate (solubilizer for Bemotrizinol) and polyacrylic acid for thickening. Then we evaluated the same emulsion upon the addition of a sunscreen polymer (Ganex V220, structure in Figure 4-2) that provides water resistance and SPF boosting. Since this is a non-invasive method, it was planned to map the sunscreen distribution on the skin after application and also to investigate the integrity of the sunscreen film over time. CRM has been used in several studies to investigate the molecular

composition of the skin[24-25], to study the penetration of drugs or active ingredients[26-29], to investigate skin hydration[24, 30], and also to investigate skin penetration enhancers[27, 31-32].

Bemotrizinol, whose structure is repeated in Figure 4-1 for convenience, is a synthetic organic molecule with molecular weight of 627.80 g/mole that absorbs in the UV region. It has two phenolic rings connected to a central triazine ring which are expected to have signature Raman bands near 1048 cm^{-1}, 1232 cm^{-1}, 1320 cm^{-1} and 1505 cm^{-1}. This molecule also has two hydrophobic ethylhexyl groups connected to the phenolic rings which render it soluble in common cosmetic solvents.

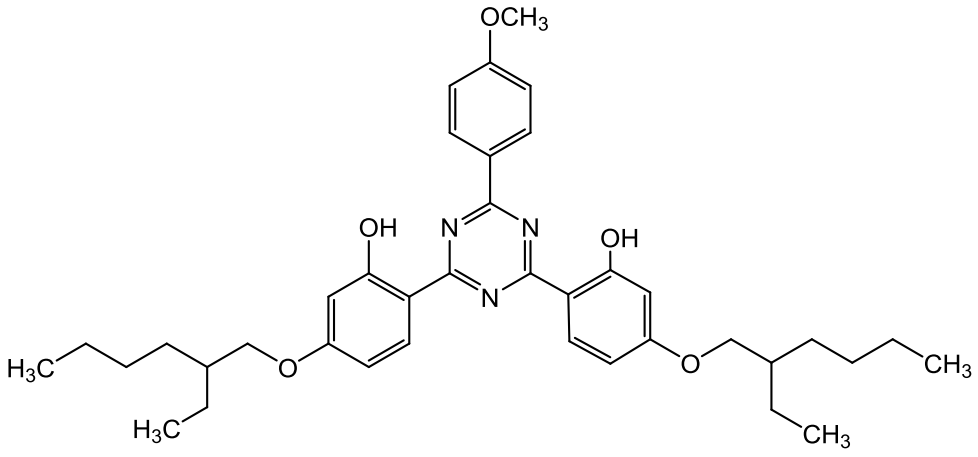

Figure 4-1. Structure of Bemotrizinol.

4.2 Results and Discussion

As noted above, a basic sunscreen o/w cream was used for this research. Raman spectra for typical emulsifiers, thickeners and esters along with Bemotrizinol were obtained and searched for signature bands that do not overlap with the Amide I band of the skin. The stoichiometric details for the formula used here are shown in Table 2-1 (Refer to Chapter 2 for formulation). The pH of the cream was adjusted to around 5.75, which is close to the pH of the SC[33-34].

Table 2-2 shows the formulation containing the film forming polymer Ganex V220. The polymer was used at 1% in this sunscreen formula. The structure of the polymer is shown in Figure 4-2, where the R group is C-20 and the ratio of the VP/alkyl is 30/70. In addition to the 3% Bemotrizinol, another formula containing 6% Bemotrizinol was evaluated. However, the formula had to be modified because Bemotrizinol was not completely soluble. The concentration of phenethyl benzoate was increased to 8% to solve the solubility issue. The optimized formula is shown in Table 2-3. Each formula was evaluated for SPF following the COLIPA (European Cosmetic Trade Association) guideline[12, 35]. The in-vitro SPF measurement was done in our lab following the COLIPA guideline and the values are shown in Table 4-1. The SPF result for the base formula containing 3% Bemotrizinol is 8.63 and this value increased to 9.66 upon the addition of the polymer to the formulation, whereas the composition with 6% Bemotrizinol gave an SPF value of 11.41. The increased SPF upon the addition

of the polymer is in agreement with one normally observed with polymers that claim SPF boosting.

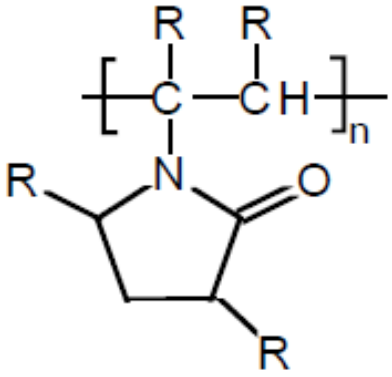

Figure 4-2. Structure of film-forming polymer: Vinylpyrrolidone/Eicosene copolymer (R=C20).

Table 4-1. In-vitro SPF value of sunscreen formulations.

Description	**In-vitro SPF**
Sunscreen cream – 3% Bemotrizinol	8.63
Sunscreen cream – 3% Bemotrizinol, 1% VP/Eicosene copolymer	9.66
Sunscreen cream – 6% Bemotrizinol	11.41

The Raman spectrum of Bemotrizinol is shown in Figure 4-3A; the Raman spectra of the cream base and the cream base with Bemotrizinol is shown in

Figure 4-3B. The spectrum has many strong bands to serve as markers for Bemotrizinol, and we had to establish that these marker bands do not overlap with major skin bands. In addition, K-Means cluster analysis (see experimental section) was used to find similar regions in the data set by generating a binary image and average the spectra for each cluster. This was done for untreated skin, cream control on skin, and cream with Bemotrizinol

Figure 4-4A shows the spectra of the untreated SC, and the SC treated with the cream base, and the cream containing Bemotrizinol. Major skin bands, such as Amide I 1650 cm^{-1}, CH_2, CH_3 stretch (2800 – 3000) cm^{-1} and the OH stretch (3100 – 3600 cm^{-1}) are noted. A zoom-in into the 800-1800 cm^{-1} region is shown in Figure 4-4B. The bands at 1048 cm^{-1} and 1505 cm^{-1} are Bemotrizinol bands (see Figure 4-3A) which will be used as marker bands to monitor Bemotrizinol distribution on the skin.

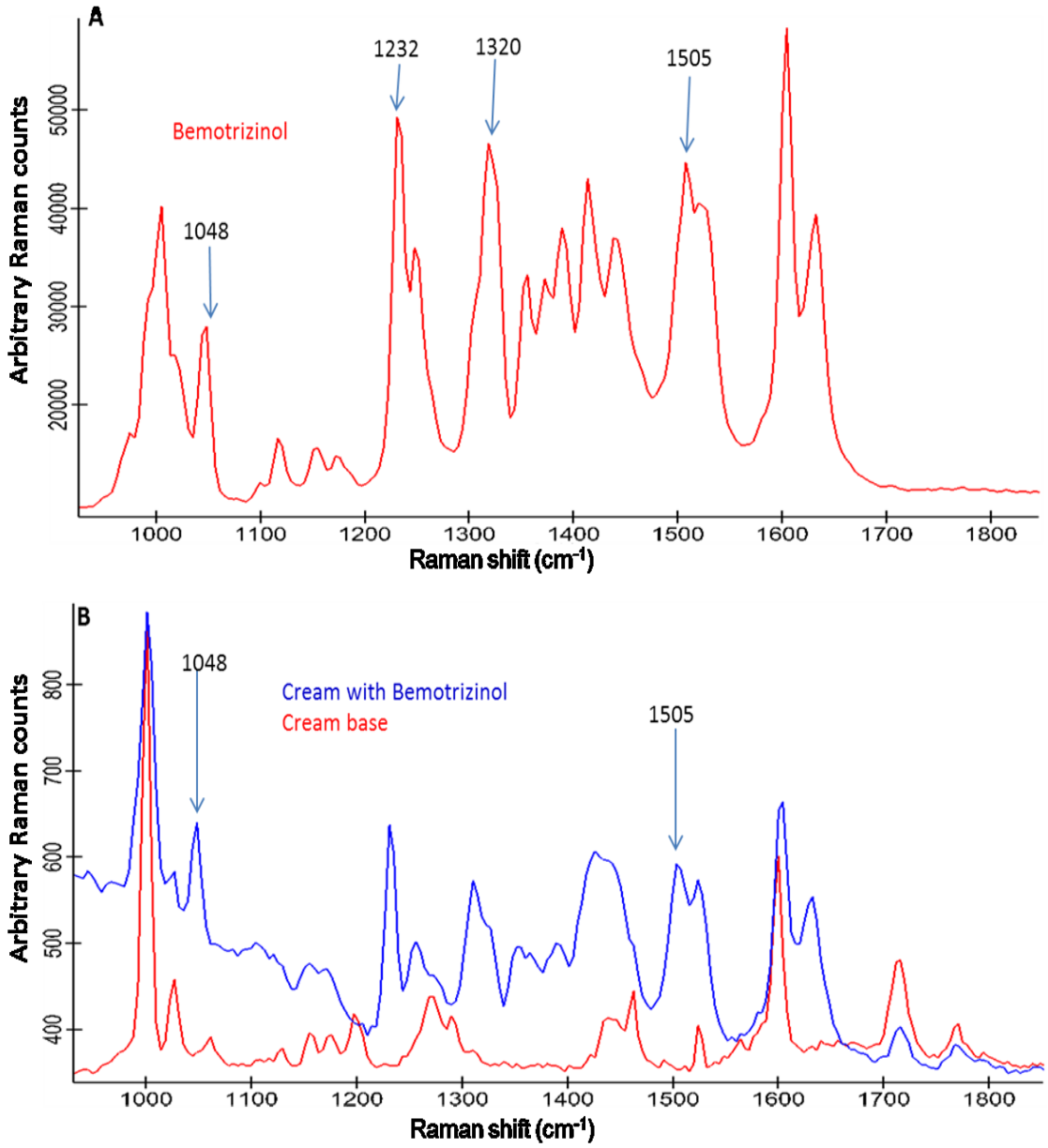

Figure 4-3. (A) Raman Spectra of Bemotrizinol. (B) Raman spectra of cream base (red) and Bemotrizinol in cream base (blue) showing marker bands 1048 cm^{-1} and 1505 cm^{-1}.

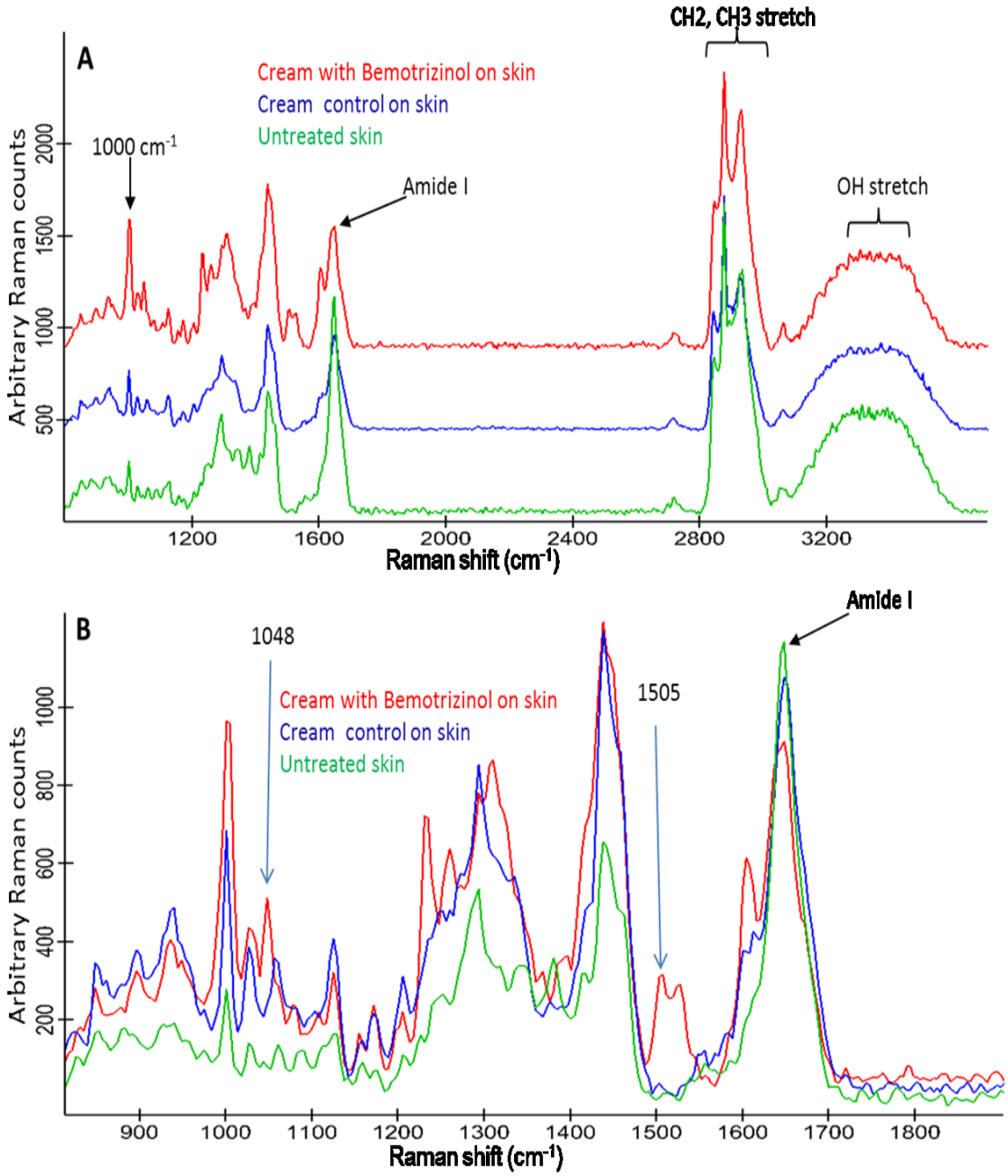

Figure 4-4. (A) Raman spectra of untreated SC (green), SC treated with cream control (blue) and SC treated with cream containing Bemotrizinol (red). (B) Zoom into the 800-1800 cm^{-1} region from (A).

Images of the distribution of Bemotrizinol within the SC were generated from the ratio of the signal intensity of each marker band cited above to the endogenous Amide I intensity of the skin. Images of a section 100 μm in the x-y plane and 60 μm in the z direction were generated using a step size of 2 microns for each experiment. Untreated and treated skin were incubated at 32 ºC for 24 hrs. before spectra were acquired. Two images were generated for each skin sample. The first one was initiated immediately after incubation and a second image from a different location (labeled 4.5 hrs.) was examined starting 4.5 hrs. after incubation.

Figure 4-5 (A,B) show the images of the intensity of the ratio of 1048 cm^{-1} and 1505 cm^{-1} bands to Amide I band in a control experiment involving untreated SC incubated for 24 hrs. To compensate for any changes that occur during incubation, we subjected untreated skin to equivalent conditions. A range of ratio values, 0.2 to 1 arbitrary units (au) for the 1048 cm^{-1} marker band and 0.1 to 1 arbitrary units (au) for the 1505 cm^{-1} marker band, was used for the color bar for all the images within that group of experiments. The resultant images are color coded with purple being no detection and red the highest relative concentration. The color bar range was chosen so that the untreated skin shows no detection of Bemotrizinol, (since the material was absent from the sample) and the same setting was used to generate the images for the treated SC. The surface of each image was also masked for glass since a glass cover slip was placed on the surface of the SC during measurement. The images for the 1048 cm^{-1} and 1505

cm^{-1} marker bands shown in Figure 4-5A and 4-5B, respectively, show no indication of Bemotrizinol for the untreated SC samples, as expected. Similar images were generated for the SC treated with the cream base, Figure 4-6. Since the cream base does not contain bemotrizinol, the images also show no detection of the 1048 cm^{-1} and 1505 cm^{-1} marker bands. The results are the same for the sample measured immediately after incubation and the one taken 4.5 hrs. after incubation.

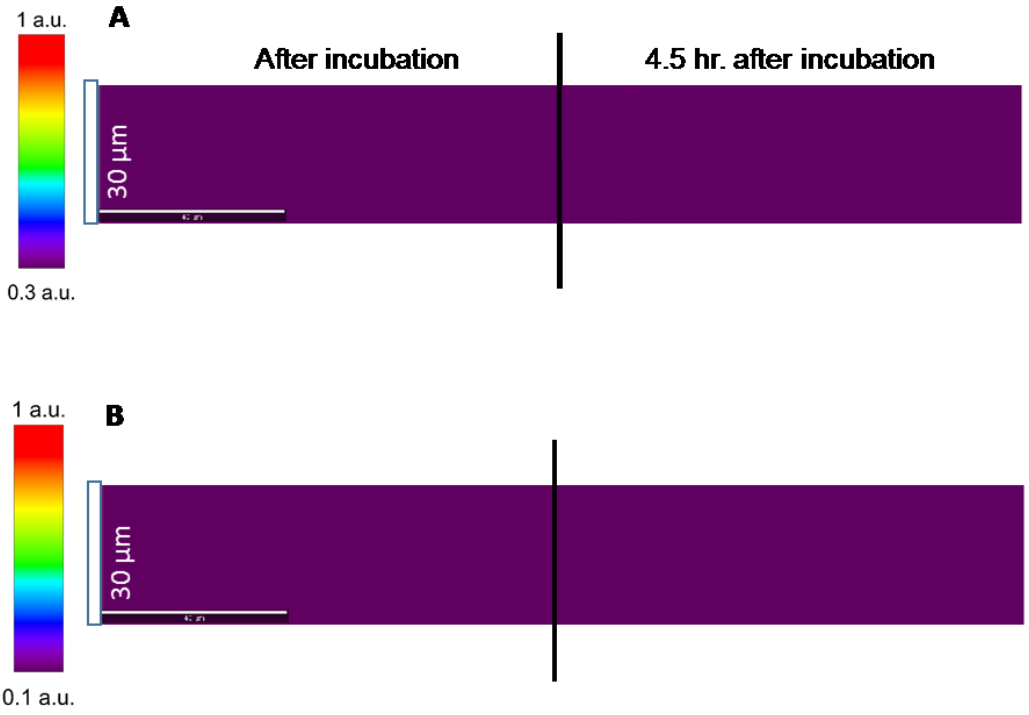

Figure 4-5. Control Experiments. Confocal Raman images of untreated skin samples incubated for 24 hrs. (A) Image (left to right) intensity of 1048 cm^{-1}/Amide I for untreated SC after incubation and 4.5 hrs. after incubation; (B) Image (left to right) intensity of 1505 cm^{-1}/Amide I for untreated SC after incubation and 4.5 hrs. after incubation.

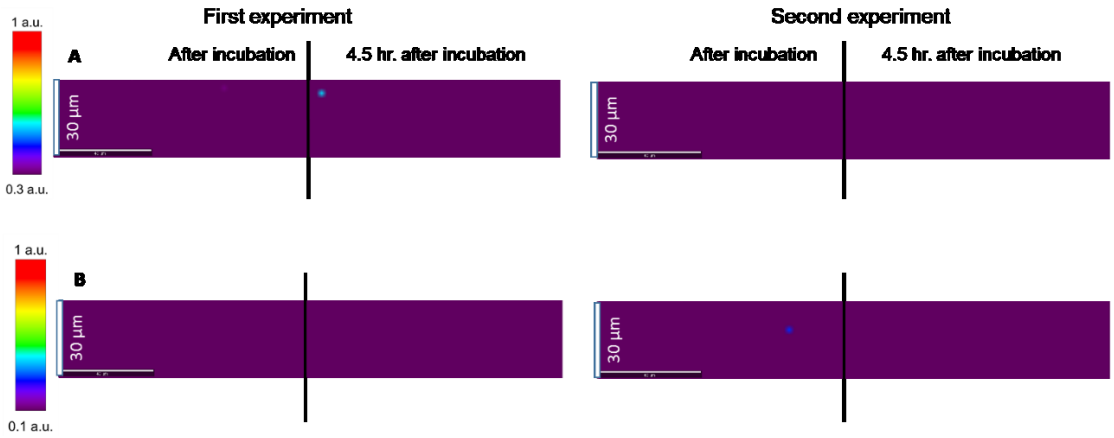

Figure 4-6. Confocal Raman images of skin treated with cream base and incubated for 24 hrs (duplicate experiments). (A) Image intensity of 1048 cm^{-1}/Amide I after incubation and 4.5 hrs. after incubation; (B) Image intensity of 1505 cm^{-1}/Amide I after incubation and 4.5 hrs. after incubation.

Images for the ratios of the 1048 and 1505 cm^{-1} bands to Amide I band for skin treated with the cream containing 3% Bemotrizinol are shown in Figure 4-7A and 4-7B, respectively. The results clearly indicate that Bemotrizinol is present on the surface and does not permeate into the SC (within the detection limits of the Raman experiment). The surface of each image was also masked for glass since a glass cover slip was placed on the surface of the SC to maintain hydration during the measurement. A similar image generated for the cream with 3% Bemotrizinol and 1% film forming polymer is shown in Figure 4-8. The signal intensity for the 1048 cm^{-1} and 1505 cm^{-1} bands appear slightly stronger on the surface and more uniform in these images than in the images without the

polymer. This result tends to suggest that the polymer helps to maintain a uniform distribution of the Bemotrizinol on the skin. Also, if the polymer helps to disperse Bemotrizinol, this could explain why we see a higher SPF value when the polymer is present in the formulation. In another study, we increased the concentration of Bemotrizinol to 6%, but a problem was encountered with solubility; therefore, we increased the phenethyl benzoate to 8% to maintain solubility. The image from this study is shown in Figure 4-9. The results did not show a more uniform or higher concentration of Bemotrizinol on the surface when compared to the image from the formulation containing 3% Bemotrizinol. The indentation in the surface of the skin for the image acquired 4.5 hrs. after incubation in the first experiment is a result of a hair shaft, as marked in Figure 4-9.

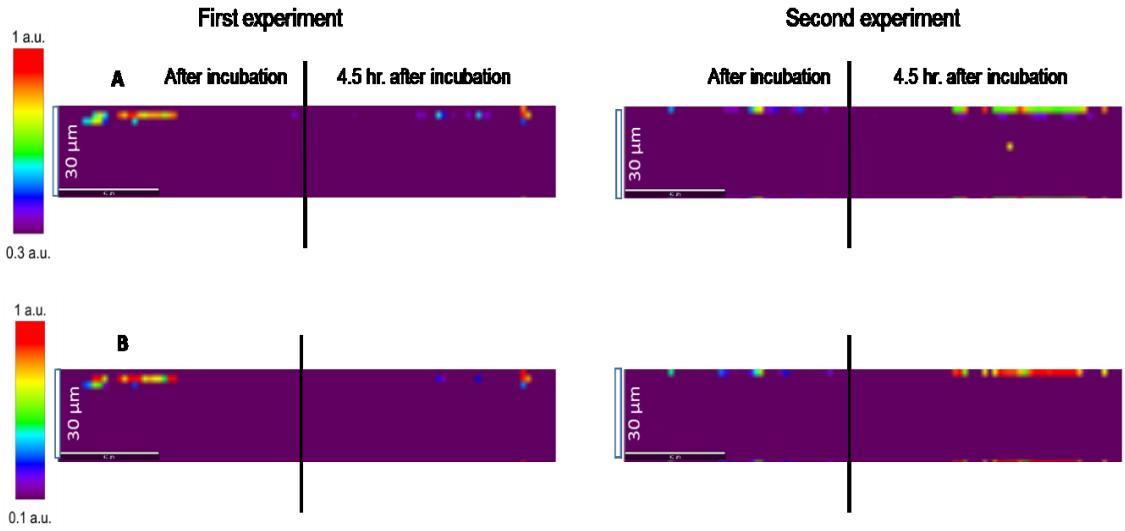

Figure 4-7. Confocal Raman images of skin treated with cream containing 3% Bemotrizinol and incubated for 24 hrs (duplicate experiments). (A) Image intensity of 1048 cm^{-1}/Amide I after incubation and 4.5 hrs. after incubation; (B)

Image intensity of 1505 cm^{-1}/Amide I after incubation and 4.5 hrs. after incubation.

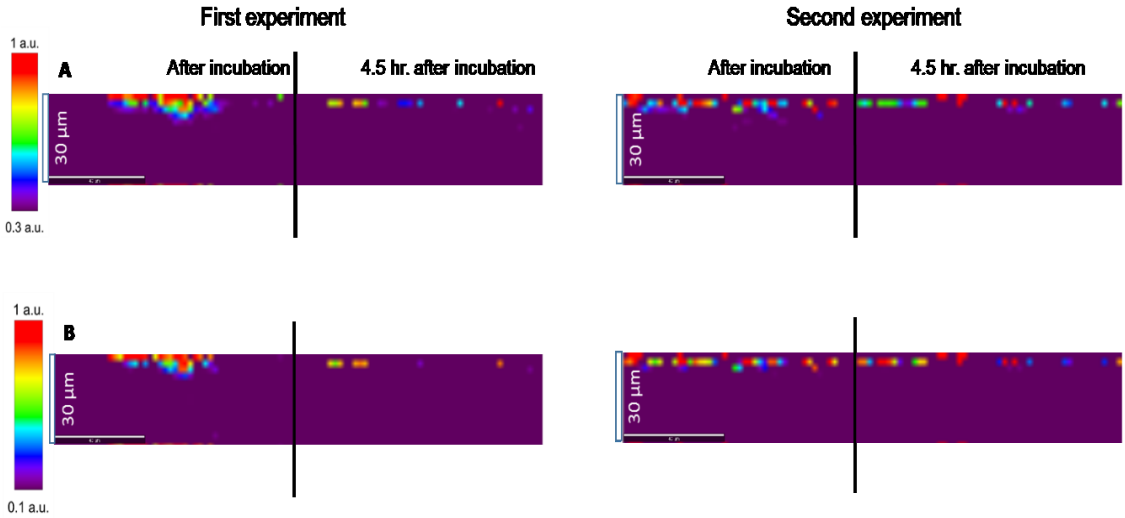

Figure 4-8. Confocal Raman images of skin treated with cream containing 3% Bemotrizinol and 1% polymer after incubation for 24 hrs. (duplicate experiments). (A) Image intensity of 1048 cm^{-1}/Amide I after incubation and 4.5 hrs. following incubation; (B) Image intensity of 1505 cm^{-1}/Amide I after incubation and 4.5 hrs. following incubation.

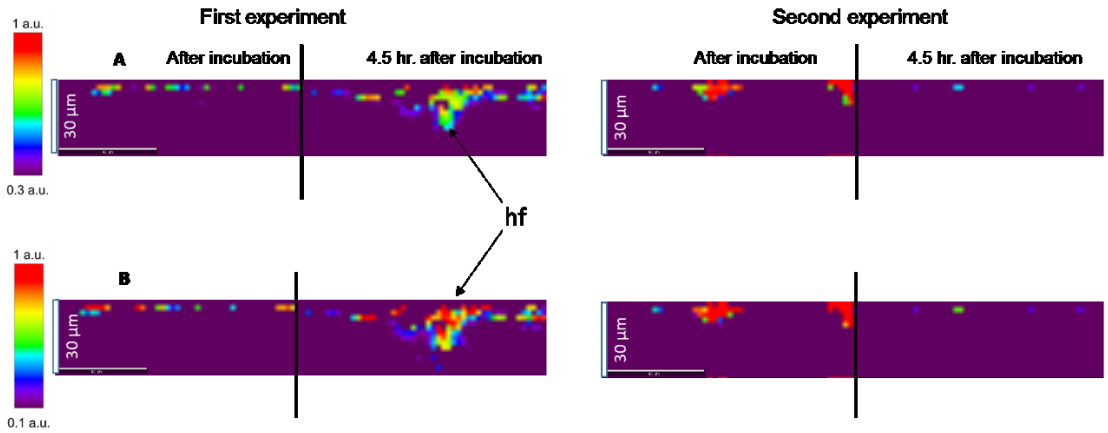

Figure 4-9. Confocal Raman image of the skin treated with cream containing 6% Bemotrizinol after incubation for 24 hrs (duplicate experiments). (A) Image intensity of 1048 cm^{-1}/Amide I after incubation and 4.5 hrs. after incubation; (B) Image intensity of 1505 cm^{-1}/Amide I after incubation and 4.5 hrs. after incubation. Note the presence of the hair follicle as marked (hf) in the first experiment.

4.3 Conclusion

Confocal Raman microscopy provides the ability to measure, in a spatially resolved fashion, the molecular, structural and compositional information of a sample in vivo and in vitro in a non-destructive manner. CRM was used to study the distribution and permeation behavior of the sunscreen material, Bemotrizinol, when formulated into a sunscreen emulsion, and applied to ex-vivo human skin. For any new formulation, it is important to be able to optimize the distribution or penetration (or lack of penetration) of the active ingredient on the substrate while the formula is being developed. Typical final formulas are very complex; each ingredient may influence the barrier of the skin. Therefore, it is important to use

a tool that confers the ability to map the distribution or transport across the skin while optimizing the formula. In the current study, we were able to monitor the distribution of Bemotrizinol on the surface of the SC when delivered from a typical sunscreen o/w emulsion using CRM. Our results showed that the sunscreen active is distributed on the surface of the SC as expected. We also investigated the effect of a film forming polymer on the distribution of the filter on the SC. The results indicate that when the polymer is present, the sunscreen appears to be distributed more homogeneously on the SC which may suggest why the SPF value may be higher when the polymer is included in the formula. Our results also indicate that Bemotrizinol remained on the surface of the SC during the 24 hr. incubation period. This is a very important finding because an emulsion formulation contains ingredients such as surfactant or solubilizer which may affect the lipid structure of the skin thus disrupting the barrier function and affecting transport of exogenous material across the SC. The current finding demonstrates that CRM is an invaluable tool in skin research designing new formulas because the approach provides the opportunity for optimizing formulations in-vitro during product development. This is also a cost saving approach because in-vivo studies are expensive, and the turn-around time of the Raman approach is relatively fast compared to in-vivo studies.

4.4 References IV

1. Young, A. R.; Chadwick, C. A.; Harrison, G. I.; Nikaido, O.; Ramsden, J.; Potten, C. S., The similarity of action spectra for thymine dimers in human epidermis and erythema suggests that DNA is the chromophore for erythema. *The Journal of investigative dermatology* **1998,** *111* (6), 982-8.
2. Hacham, H.; Freeman, S. E.; Gange, R. W.; Maytum, D. J.; Sutherland, J. C.; Sutherland, B. M., Do pyrimidine dimer yields correlate with erythema induction in human skin irradiated in situ with ultraviolet light (275-365 nm)? *Photochemistry and photobiology* **1991,** *53* (4), 559-63.
3. Watson, M.; Holman, D. M.; Maguire-Eisen, M., Ultraviolet Radiation Exposure and Its Impact on Skin Cancer Risk. *Seminars in Oncology Nursing* **2016,** *32* (3), 241-254.
4. Shaath, N. A., Ultraviolet filters. *Photochem. Photobiol. Sci.* **2010,** *9* (4), 464-469.
5. Bennett, R. G.; Robins, P., On the selection of a sunscreen. *J Dermatol Surg Oncol* **1977,** *3* (2), 205-9.
6. ISO, Cosmetics - Sun protection test methods - Review and evaluation of methods to assess the photoprotection of sun protection products. *ISO/TR 26369*.
7. Stokes, R.; Diffey, B., How well are sunscreen users protected? *Photodermatology, photoimmunology & photomedicine* **1997,** *13* (5-6), 186-8.
8. Osterwalder, U.; He, Q.; Sohn, M.; Herzog, B., Sustainable sun protection with sunscreens requires the right technology and good compliance. *SOFW J.* **2012,** *138* (7), 2,4-6,8,10-12,14-16,18.
9. Lademann, J.; Rudolph, A.; Jacobi, U.; Weigmann, H. J.; Schaefer, H.; Sterry, W.; Meinke, M., Influence of nonhomogeneous distribution of topically applied UV filters on sun protection factors. *Journal of biomedical optics* **2004,** *9* (6), 1358-62.
10. Pissavini, M.; Diffey, B.; Marguerie, S.; Carayol, T.; Doucet, O., Predicting the efficacy of sunscreens in vivo veritas. *Int J Cosmet Sci* **2012,** *34* (1), 44-8.
11. Schulz, J.; Hohenberg, H.; Pflücker, F.; Gärtner, E.; Will, T.; Pfeiffer, S.; Wepf, R.; Wendel, V.; Gers-Barlag, H.; Wittern, K. P., Distribution of sunscreens on skin. *Advanced Drug Delivery Reviews* **2002,** *54, Supplement*, S157-S163.
12. Springsteen, A.; Yurek, R.; Frazier, M.; Carr, K. F., In vitro measurement of sun protection factor of sunscreens by diffuse transmittance1. *Analytica Chimica Acta* **1999,** *380* (2–3), 155-164.
13. Binks, B. P.; Fletcher, P. D. I.; Johnson, A. J.; Marinopoulos, I.; Crowther, J.; Thompson, M. A., How the sun protection factor (SPF) of sunscreen films change during solar irradiation. *Journal of Photochemistry and Photobiology A: Chemistry* **2017,** *333*, 186-199.
14. Sohn, M.; Herzog, B.; Osterwalder, U.; Imanidis, G., Calculation of the sun protection factor of sunscreens with different vehicles using measured film thickness distribution — Comparison with the SPF in vitro. *Journal of Photochemistry and Photobiology B: Biology* **2016,** *159*, 74-81.
15. Giacomoni, P. U.; Teta, L.; Najdek, L., Sunscreens: the impervious path from theory to practice. *Photochem. Photobiol. Sci.* **2010,** *9* (4), 524-529.
16. Jacobi, U.; Weigmann, H. J.; Baumann, M.; Reiche, A. I.; Sterry, W.; Lademann, J., Lateral spreading of topically applied UV filter substances investigated by tape stripping. *Skin Pharmacol Physiol* **2004,** *17* (1), 17-22.
17. Prettypaul, D.; Fares, H., Microscopic evaluation of polymeric film properties of anhydrous sunscreen compositions and their relation to absorption and water resistance. *J. Cosmet. Sci.* **2012,** *63* (3), 213-221.

18. Rigano, L., 'Very' water-resistant sunscreens. *Cosmet. Toiletries* **2014,** *129* (3), 66, 68-73.
19. Rigon, R. B.; Piffer, A. R.; Lima, A. A. S.; Bighetti, A. E.; Chorilli, M., Influence of natural polymer derived from starch as a sensory modifier in sunscreen formulations. *Int. J. Pharm. Pharm. Sci.* **2013,** *5* (1), 306-309.
20. Van Reeth, I.; Bao, X. R.; Dib, K.; Haller, R., A hydrophilic silicone elastomer for broader formulating flexibility. *Cosmet. Toiletries* **2012,** *127* (11), 802-806.
21. Sayre, R. M.; Dowdy, J. C.; Gerwig, A. J.; Shields, W. J.; Lloyd, R. V., Unexpected photolysis of the sunscreen octinoxate in the presence of the sunscreen avobenzone. *Photochem. Photobiol.* **2005,** *81* (Mar./Apr.), 452-456.
22. Lhiaubet-Vallet, V.; Marin, M.; Jimenez, O.; Gorchs, O.; Trullas, C.; Miranda, M. A., Filter-filter interactions. Photostabilization, triplet quenching and reactivity with singlet oxygen. *Photochem. Photobiol. Sci.* **2010,** *9* (4), 552-558.
23. Paris, C.; Lhiaubet-Vallet, V.; Jimenez, O.; Trullas, C.; Miranda, M. A., A blocked diketo form of avobenzone: photostability, photosensitizing properties and triplet quenching by a triazine-derived UVB-filter. *Photochem. Photobiol.* **2009,** *85* (1), 178-184.
24. Caspers, P. J.; Bruining, H. A.; Puppels, G. J.; Lucassen, G. W.; Carter, E. A., In Vivo Confocal Raman Microspectroscopy of the Skin: Noninvasive Determination of Molecular Concentration Profiles. *Journal of Investigative Dermatology* **2001,** *116* (3), 434-442.
25. Klossek, A.; Thierbach, S.; Rancan, F.; Vogt, A.; Blume-Peytavi, U.; Rühl, E., Studies for improved understanding of lipid distributions in human skin by combining stimulated and spontaneous Raman microscopy. *European Journal of Pharmaceutics and Biopharmaceutics*.
26. Pudney, P. D. A.; Melot, M.; Caspers, P. J.; Van Der Pol, A.; Puppels, G. J., An in vivo confocal Raman study of the delivery of Trans-retinol to the skin. *Appl. Spectrosc.* **2007,** *61* (8), 804-811.
27. Mélot, M.; Pudney, P. D. A.; Williamson, A.-M.; Caspers, P. J.; Van Der Pol, A.; Puppels, G. J., Studying the effectiveness of penetration enhancers to deliver retinol through the stratum cornum by in vivo confocal Raman spectroscopy. *Journal of Controlled Release* **2009,** *138* (1), 32-39.
28. Forster, M.; Bolzinger, M.-A.; Ach, D.; Montagnac, G.; Briancon, S., Ingredients tracking of cosmetic formulations in the skin: a confocal Raman microscopy investigation. *Pharm Res* **2011,** *28* (4), 858-72.
29. Zhang, G.; Moore, D. J.; Sloan, K. B.; Flach, C. R.; Mendelsohn, R., Imaging the Prodrug-to-Drug Transformation of a 5-Fluorouracil Derivative in Skin by Confocal Raman Microscopy. *Journal of Investigative Dermatology* **2007,** *127* (5), 1205-1209.
30. Nakagawa, N.; Matsumoto, M.; Sakai, S., In vivo measurement of the water content in the dermis by confocal Raman spectroscopy. *Skin research and technology : official journal of International Society for Bioengineering and the Skin (ISBS) [and] International Society for Digital Imaging of Skin (ISDIS) [and] International Society for Skin Imaging (ISSI)* **2010,** *16* (2), 137-41.
31. Pyatski, Y.; Zhang, Q.; Mendelsohn, R.; Flach, C. R., Effects of permeation enhancers on flufenamic acid delivery in Ex vivo human skin by confocal Raman microscopy. *International Journal of Pharmaceutics* **2016,** *505* (1–2), 319-328.
32. Mujica Ascencio, S.; Choe, C.; Meinke, M. C.; Mueller, R. H.; Maksimov, G. V.; Wigger-Alberti, W.; Lademann, J.; Darvin, M. E., Confocal Raman microscopy and multivariate statistical analysis for determination of different penetration abilities of caffeine and propylene glycol applied simultaneously in a mixture on porcine skin ex vivo. *Eur. J. Pharm. Biopharm.* **2016,** *104*, 51-58.

33. Fluhr, J. W.; Elias, P. M., Stratum corneum pH: Formation and Function of the 'Acid Mantle'. *Exog. Dermatol.* **2002,** *1* (4), 163-175.
34. Hachem, J.-P.; Crumrine, D.; Fluhr, J.; Brown, B. E.; Feingold, K. R.; Elias, P. M., pH directly regulates epidermal permeability barrier homeostasis, and stratum corneum integrity/cohesion. *J. Invest. Dermatol.* **2003,** *121* (2), 345-353.
35. Diffey, B. L.; Tanner, P. R.; Matts, P. J.; Nash, J. F., In vitro assessment of the broad-spectrum ultraviolet protection of sunscreen products. *Journal of the American Academy of Dermatology* **2000,** *43* (6), 1024-1035.

CHAPTER 5 Confocal Raman Microscopy of DEET Permeation into the Stratum Corneum and the Effect of Polymers on the Process

5.1 Introduction

DEET (N,N-diethyl-m-toluamide) is the most efficacious and widely used active ingredient formulated into insect repellent for the past six decades.[1] It is present in many commercial products such as creams, lotions, gels, sticks and sprays at concentration typically less than ~ 40%. A concentration of 10% to 35% DEET will provide adequate protection for routine outdoor activities[1]. Even at such relatively high concentrations, DEET manages to maintain a strong safety record with proper application, even though its absorption through the skin is well documented[2-4]. The molecular structure of DEET is shown in Figure 5-1A.

Human skin is well studied with many publications concerning its function[5-7] and structural properties[8-10]. Although skin is generally perceived as the outer layer of the human body, it possesses many layers with the stratum corneum (SC) forming the outermost one. As such, the SC basically provides a protective barrier from the environment and prevents water loss from the body. The SC is often portrayed in the context of “brick and mortar” model composed of keratin-filled corneocytes embedded in a lipid matrix [11]. There are many published reports investigating the effect of environmental factors, such as temperature, humidity[12-13], and formulation types[2, 14-16] on the permeation rate of DEET through the skin. The major limitation to these studies is that most of them relied on the Franz diffusion cell method to track permeation through the skin.

The Franz diffusion cell (see Figure 2-1) method uses either human or pig skin. The skin sample is mounted on the cell that has been previously filled with a buffer solution in which the bottom of the skin section is in physical contact with the buffer. The surface of the skin is then treated with the product of interest. The cell is sealed and incubated at a fixed temperature for the selected time interval. The receptor solution is exchanged at particular times and analyzed for the active material with an analytical technique such as HPLC. The major disadvantage of this experimental design is that the results measure simply what passes through the skin under the conditions of the measurements. The approach doesn't provide information about the mechanism of permeation, e.g. whether the DEET pools in particular sections of the skin or whether it permeates continuously through the skin.

Confocal Raman Microscopy (CRM) has been used in related work to study the penetration of drugs or other active ingredients,[17-19] skin hydration[20-21], lipid distribution in the skin[22-23] and, more recently, the mechanism of permeation enhancers[24]. In the current chapter, two examples of the utility of confocal Raman CRM are presented. First, CRM was used to investigate the penetration of DEET into skin. CRM offers many advantages over conventional microscopy mainly because it is a noninvasive optical method. The approach also allows us to obtain detailed information concerning the sample being investigated, while preserving the skin sample in a state as close as possible to its native state. CRM can provide a spectroscopic fingerprint of the exogenous molecule being studied

along with the environment of the molecule. With CRM, it is now easier and more efficient than previously possible to track penetration processes of the active ingredient.

In the second approach, we wanted to investigate the effect of polymers on the distribution and permeation of DEET within the SC. Several polymers were added to the commercial OFF! product for this study. The polymers were chosen based on their use in personal care applications and include a film former, a controller of bio-adhesive properties, and a solubility and rheology modifier. The skin is a very important route for the dermal or transdermal delivery of pharmaceutical actives. A great deal of work has been done on understanding the effect of polymers in this type of application[25-27]. The use of polymeric films in tablet coatings for drug delivery is well documented[28]. Similarly, film-forming polymers are used in cosmetic products to improve the water resistance of sunscreen product[29-30]. Therefore, it is a potentially important advance to understand the effect of polymers on the permeation and distribution of DEET within the SC.

5.2 Results and Discussion

Several spectral features were potentially useful for identification of DEET within the OFF! Deep woods product and after application of OFF! to the SC. The OFF! Deep woods product contains 25% DEET along with 75% other ingredients. Ingredients listed on the Material Safety Data Sheet are shown in Table 5-1 with

ethanol in the range from 30-60%. The Raman spectra of pure DEET, OFF! Deep woods, and ethanol are shown in Figure 5-1A. The spectra for DEET and OFF! Deep woods are very similar with the exception of an additional band at 886 cm^{-1} for the OFF! Deep woods product. We determined that this peak corresponds to the CCO stretching[31-32] from the ethanol present in the OFF! product. Thus, the DEET bands are the main contributor to the Raman spectrum of the commercial product.

Four Raman bands appeared to be potentially useful for characterizing the location of the DEET in the tissue. The intense band at 1003 cm^{-1} band in DEET arises from the breathing mode of the aromatic ring. Another band at 1606 cm^{-1} arises from the aromatic C=C stretching mode. There are two additional bands, 522 cm^{-1} and 687 cm^{-1} which can also serve as marker bands for DEET. Figure 5-1B shows the spectrum of untreated SC and the spectrum of SC treated with the OFF! product. Signature skin bands such as the Amide I (peptide bond C=O stretch,1650 cm^{-1}), CH_2 and CH_3 stretch (2800-3000 cm^{-1}) and OH stretch (3100-3600 cm^{-1}) are also clearly observed. These Raman signature bands (shown in Figure 5-1B) of various constituents of the SC are well characterized[33-34].

After reviewing the results from the SC treated with the OFF! product, it was decided to use the bands at 522 $cm^{-1}$and 687 cm^{-1} as marker bands to track DEET within the SC. The 1003 cm^{-1} band in DEET could not be used as a marker band because the SC also contains keratin and other proteins which have phenylalanine (Phe) side chains possessing an aromatic ring breathing mode that

overlap with the 1003 cm^{-1} band [34]. Similarly, the 1606 cm^{-1} band appears on the shoulder of the Amide I band of the SC.

Table 5-1: OFF! DEEP WOODS® insect repellent composition listed on Material Safety Data Sheet

Chemical Name	CAS-no	Weight Percent
Ethyl alcohol	64-17-5	30.00-60.00
N,N-diethyl-m-toluamide	134-62-3	10.00-30.00

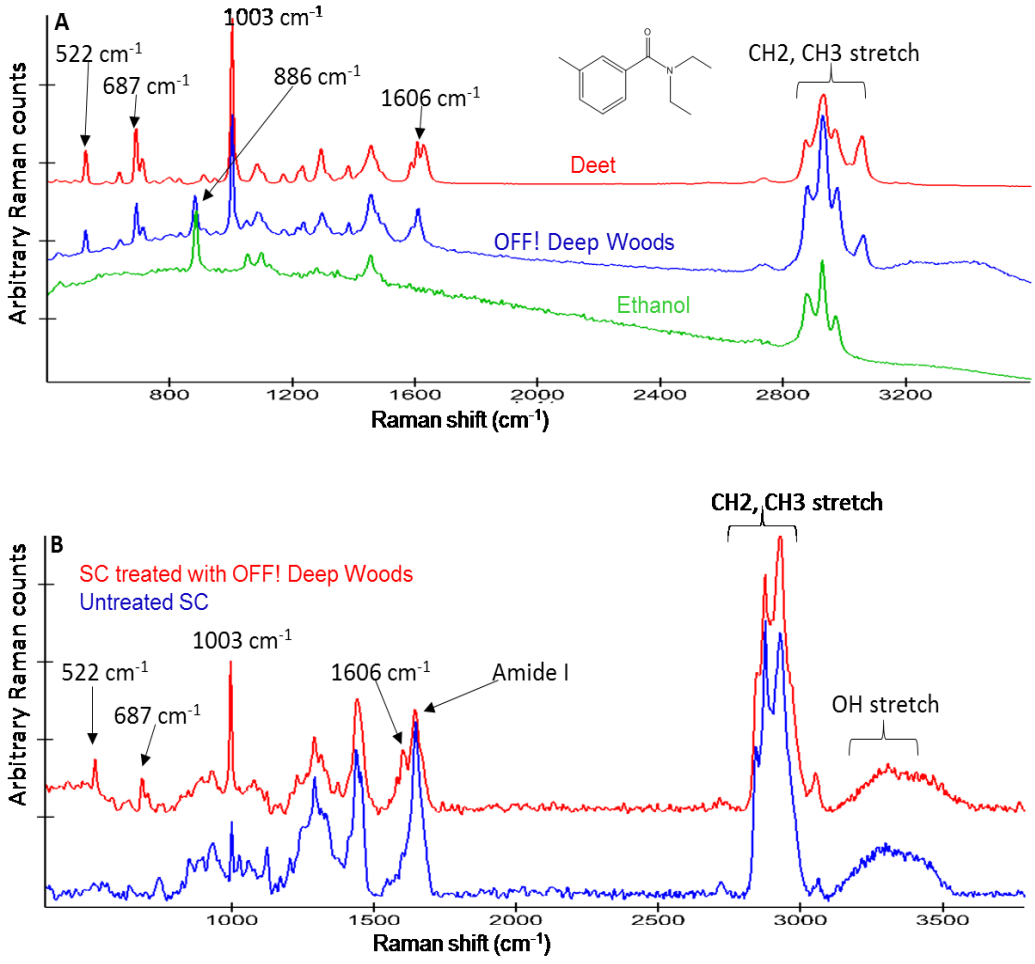

Figure 5-1. (A) Raman spectra of DEET (red), OFF! Deep Woods (blue) and ethanol (green). (B) Raman Spectra of untreated SC (blue) and SC treated with OFF! Deep Woods (red).

Images of the distribution of DEET within the SC were generated from the ratio of the signal intensity of each marker band cited above to the endogenous Amide I intensity in skin. Figure 5-2 shows this approach for the intensity of the 522 cm^{-1} band to Amide I band. Images were generated immediately after application, and at 2hrs. and 4 hrs. after treatment and incubation. Figure 5-2A shows the images for the untreated SC with no incubation and for 2 hrs. and 4 hrs. incubation, respectively. The untreated samples show no detection of DEET, as anticipated, in the range shown.

The range of ratio values shown in this figure was adjusted so that the untreated skin shows no detection of DEET and the same filter setting was used for the 522 cm^{-1}/Amide I intensity ratio to generate the images for the treated SC. To compensate for any changes that occur during incubation, we subjected untreated skin to equivalent conditions. The resultant images are color coded with purple (0.2 au) representing the maximum relative value of nothing in untreated skin and red (≥ 0.6 au) the highest relative concentrations in the presence of DEET. The same source of skin was used for all experiments to minimize variation. The surface of each image was also masked for glass since a glass cover slip was placed on the surface of the SC to maintain hydration during the measurement. This is illustrated in Figure 5-3, showing the spectra as a function of depth from top to bottom, at approximately 2 μm apart. The first two spectra from the top show the presence of the glass cover slip, and the third spectrum

shows the Amide I band clearly indicating where the skin starts. Other signature Raman bands such as CH_2, CH_3 and OH stretch from water are also identified.

The upper and lower SC boundaries are also outlined in the images. In Raman spectra of the skin, the 2880 cm^{-1} peak arises predominantly from the asymmetric methylene modes of the lipid acyl chains and the methyl band (2930 cm^{-1}) from the SC protein[17]. To outline the SC-VE boundary, we used the ratio of the intensities (2880/2930 cm^{-1}). Since the lipid content is reduced going from the SC to the VE, this is an appropriate parameter[35-36].

It is important to note that for the samples incubated for 2 hr. and 4 hr. The product was applied to the surface of the skin through the donor compartment of the Franz diffusion cell whereas the product was applied to the surface and rubbed using a finger cot for the sample that was not incubated. Therefore, most of the volatile ingredients evaporate off during application for the non-incubated SC whereas these ingredients likely remain in contact with the SC for the incubated samples since the Franz diffusion cell is sealed and this may influence the permeation of DEET.

Figure 5-2B shows the images for treated SC immediately after OFF! treatment and at 2 hrs. and 4 hrs. after incubation, left to right, respectively. Figure 5-2C is a repeat of the experiment from Figure 5-2B. The images for the duplicate experiments are similar. This is a good indication of the consistency of the method. The images show that DEET can be detected on the SC surface for the

samples that were not incubated while DEET penetrated approximately 4-6 μm into the SC for the incubated samples. The distribution of DEET on the surface appears to be non-uniform, but this is expected since the surface of the skin follows a natural contour that is undulated. In addition, as the product is applied and allowed to dry, some regions may not have an even distribution of the product. This could be because of the surface properties of the skin such as furrows or wrinkles or differences in surface tension which will prevent homogeneous spreading of the product.

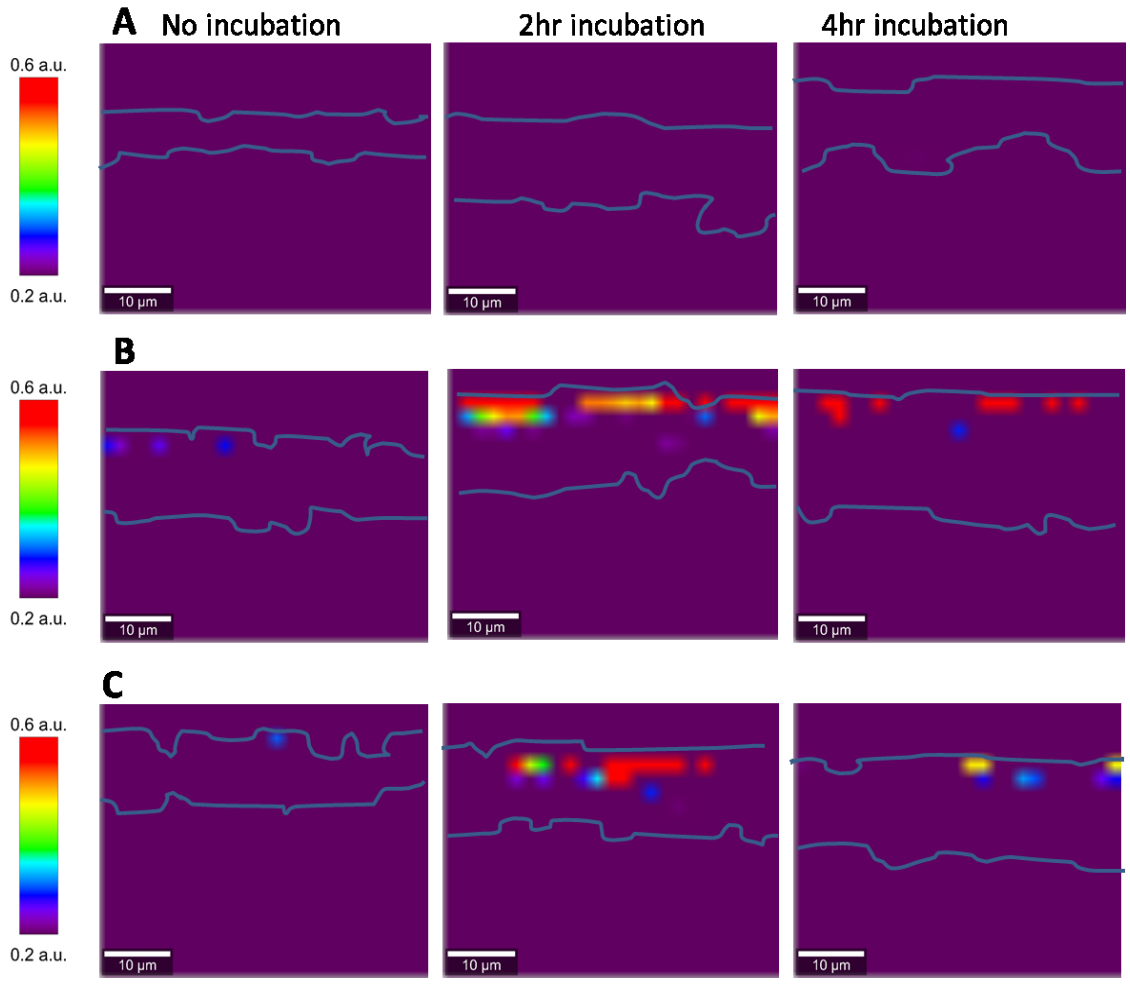

Figure 5-2. Confocal Raman image of the intensity of DEET distribution in skin samples incubated over time using marker band 522 cm^{-1}/amide I intensity. The upper and lower SC boundaries are outlined. (A) from left to right are images for untreated SC with no incubation and at 2 hrs. and 4 hrs. after incubation; (B) Images (left to right) for treated SC with no incubation and at 2 hrs. and 4 hrs. after incubation; (C) Replicate of experiment in (B).

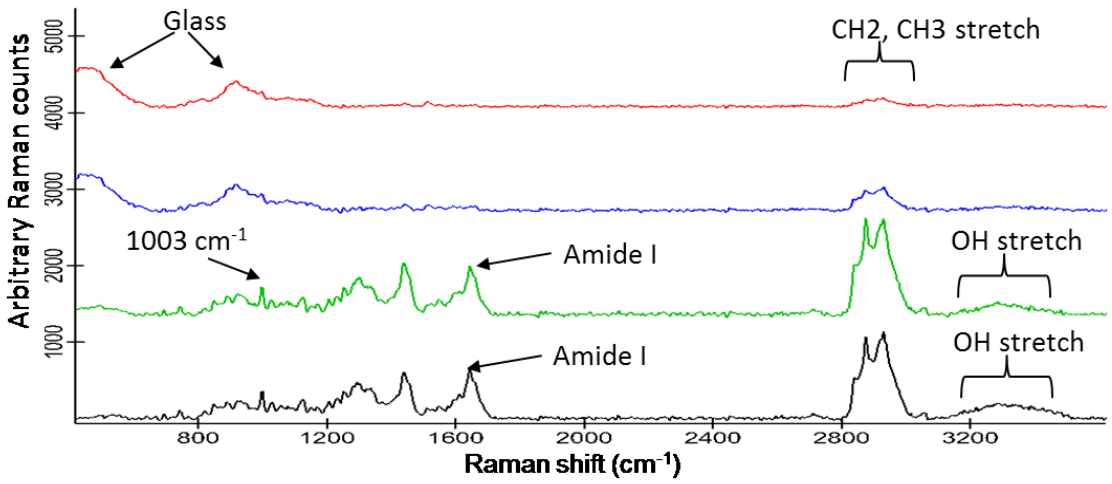

Figure 5-3. Raman spectra of an untreated skin sample acquired during a typical experiment. From top to bottom – the first two spectra show the presence of the glass cover slip, and the third spectrum down shows the Amide I band indicating where the skin region starts.

Images were also generated using the 687 cm^{-1} DEET marker bands (see Figure 5-4) under the same conditions as in Figure 5-2. Figure 5-4A shows the images for the untreated SC with no incubation and at 2 hrs. and 4 hrs. after incubation. Figure 5-4B shows the images for SC after treatment and at 2 hrs. and 4 hrs. after incubation. Figure 5-4C is a repeat of the experiment in Figure 5-4B. The images for the duplicate experiments are similar. The untreated samples show no detection of DEET (as expected). The images show that DEET can be detected on the SC surface for the samples that were not incubated while DEET penetrated approximately 6-8 μm into the SC for the incubated samples. The

distribution of DEET on the surface appears to be non-uniform for reasons that were explained earlier using the 522 cm-1 marker band. Overall, the results using the 522 cm^{-1} and 687 cm^{-1} marker bands are similar to each other.

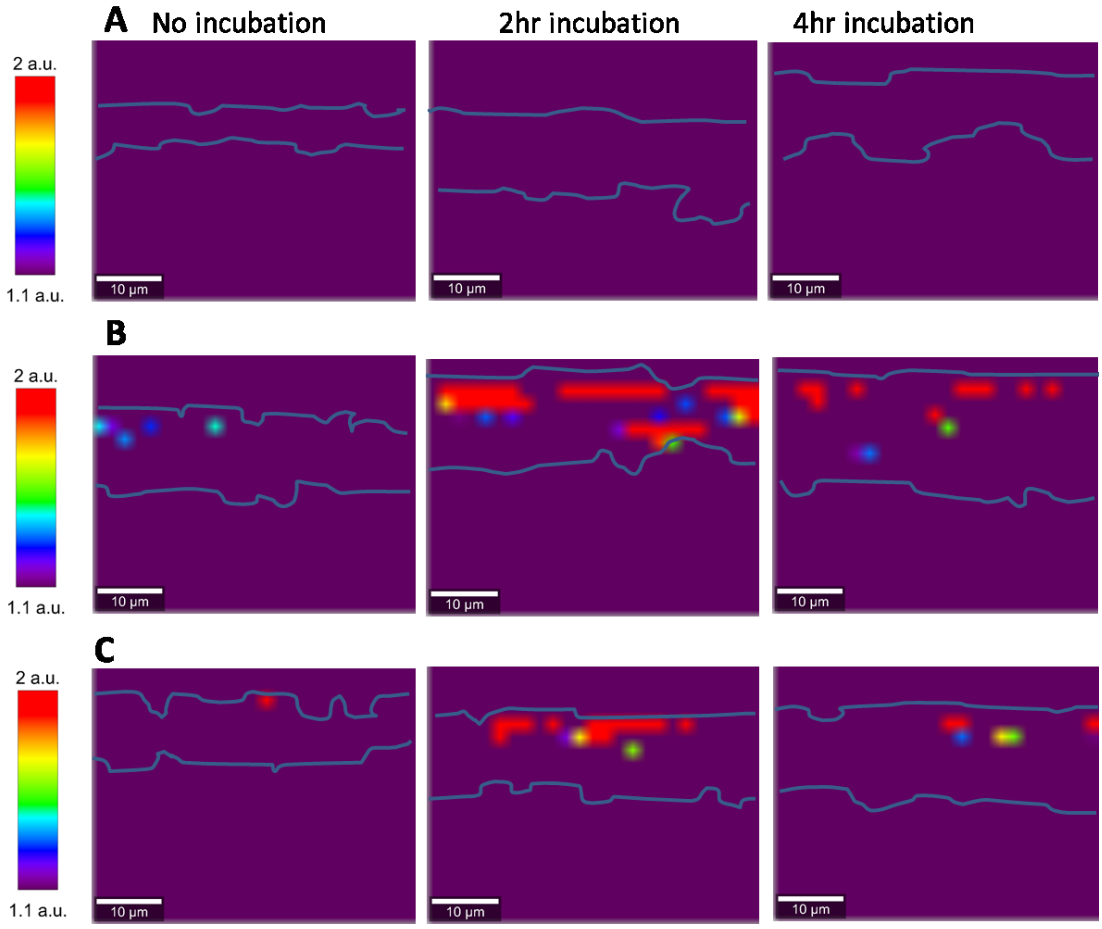

Figure 5-4. Confocal Raman image of the intensity of DEET distribution in skin samples incubated over time using marker band 687 cm^{-1}/Amide I intensity. The upper and lower SC boundaries are outlined. (A) from left to right are images for untreated SC with no incubation and at 2 hrs. and 4 hrs. after incubation; (B) Images (left to right) for treated SC with no incubation and at 2 hrs. and 4 hrs. after incubation; (C) Replicate of experiment in (B).

The current data analysis and the resulting images do not allow us to determine the absolute concentration of DEET. This arises because Raman scattering is a single beam experiment. Nothing equivalent to Beer's Law for IR spectroscopy is available. In addition, the refractive index of skin varies from point to point in the sample affecting the scattering intensity and cannot easily be calibrated for. Thus, we can only show the relative concentration based on the ratio to the Amide I band (or possibly another spectral feature). The samples that were not incubated suggest that DEET concentration is not uniform close to the surface. In addition to the furrows and undulations discussed previously, this may also be due to the swabbing of the skin surface prior to measurements. On the other hand, DEET had time to permeate into the SC for the incubated samples, so swabbing the surface after incubation does not remove the DEET that penetrated.

The results showed good correlation between the two marker bands. The penetration depth ranges from about 2 μm for the non-incubated samples to about 10 μm for the samples incubated for 2 hr. and 4 hr. However, no major penetration differences were noted between the samples incubated for 2hrs. vs 4 hrs. This could be because of the lack of sensitivity from the CRM method since the concentration of DEET decreases as it penetrates deeper into the skin.

5.3 Addition of Polymers to OFF! Deep Woods

To investigate the effect of polymer on the distribution and permeation of DEET within the SC, several polymers were added to the commercial OFF! product. The polymers were chosen based on their use in personal care applications. The first polymer, S2000 (INCI Name: VP/Acrylates/Lauryl Methacrylate Copolymer, Figure 5-5A), is used as a film former in sun care formulations because of its water resistant properties and excellent skin feel. The second polymer, ES425 (INCI Name: Butyl Ester of PVM/MA Copolymer, Figure 5-5B), was chosen for its bio-adhesive properties. The third polymer, G904(INCI Name: Butylated PVP, Figure 5-5C), is also a film forming polymer of polyvinylpyrrolidone (PVP) with C-4 alkyl groups. This polymer is unique because it is soluble in both water and oil. A fourth polymer, P100 (INCI Name: Acrylic Acid/VP Crosspolymer, Figure 5-5D), is used as a rheology modifier to control viscosity in personal care products.

The polymers were added to the DEET product at 1% (w/w) and mixed until completely dissolved. The Raman spectra of all four polymers are overlaid with the spectrum of each polymer in the OFF! Deep woods product (Figure 5-6A, B and 5-7A, B). The spectra of the polymers are very different from each other and each has signature Raman bands. However, when these polymers are added to the OFF! product, their individual bands are below the detection limit and only the Raman bands of the OFF! product are displayed. The polymers are used at 1% (w/w) concentrations in the mixtures; therefore, this level is too low to be detected.

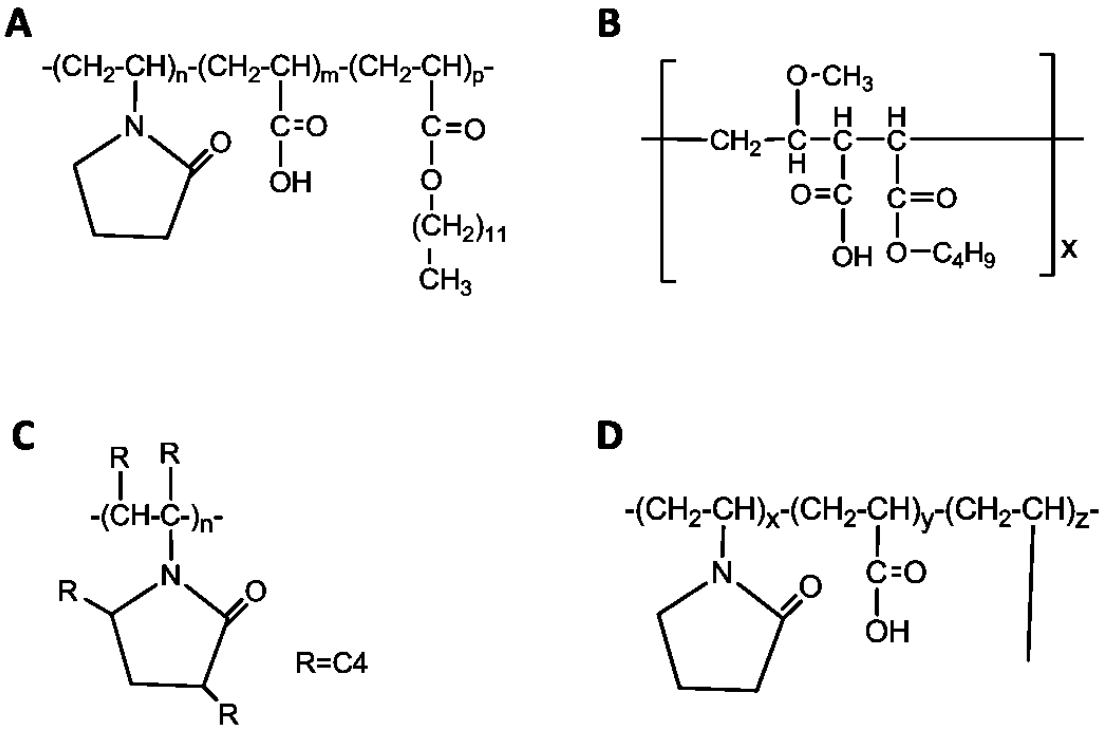

Figure 5-5. Structure of polymers evaluated in the OFF product. (A) S2000 polymer. (B) ES-425 polymer. (C) G904 polymer. (D) P-100 polymer (the long vertical line is a cross linker).

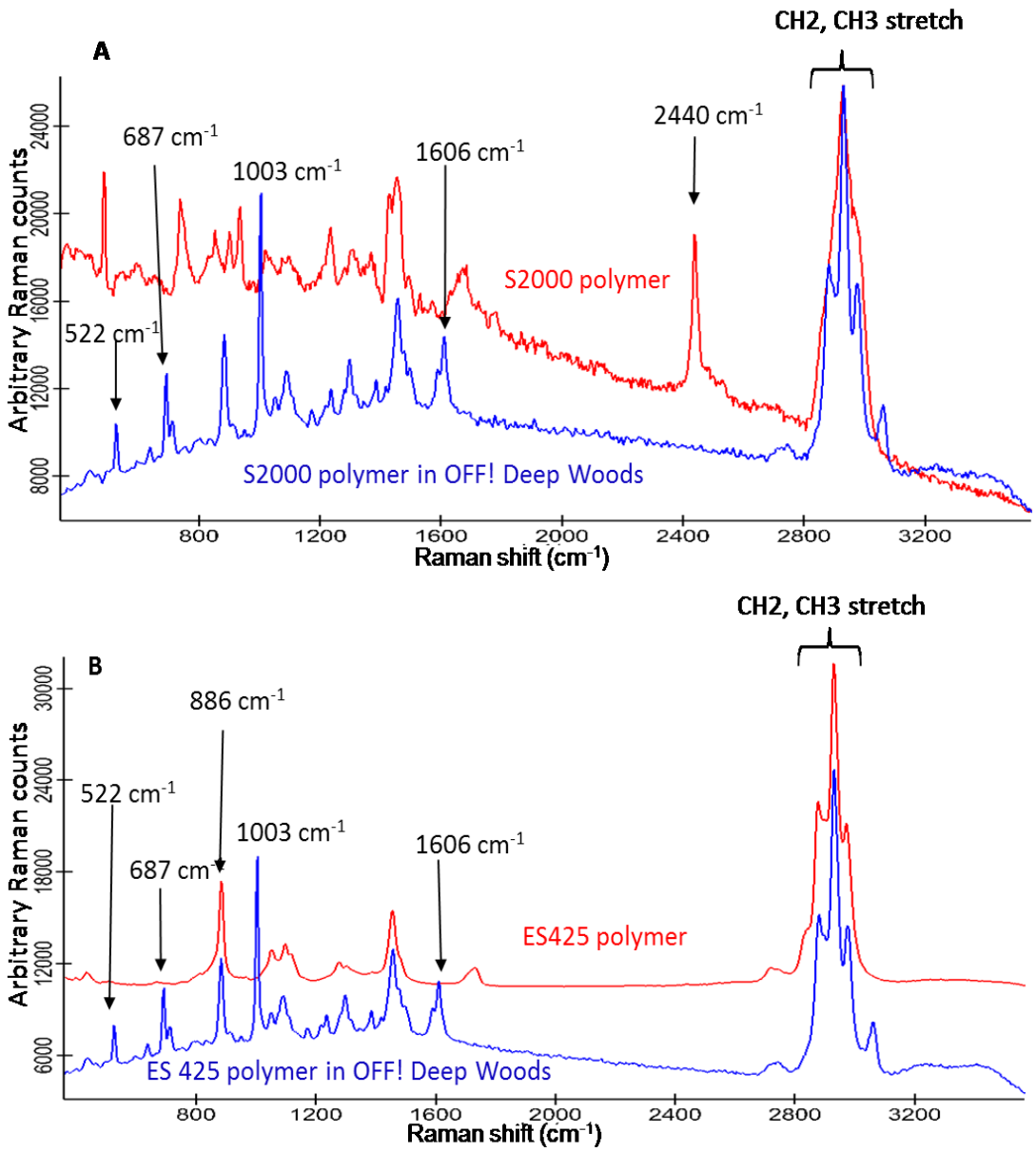

Figure 5-6. (A) Raman spectra of S2000 polymer (red) and 1% (w/w) S2000 polymer in OFF! Deep Woods (blue). (B) Raman Spectra of ES 425 polymer (red) and 1% (w/w) ES 425 polymer in OFF! Deep Woods (blue).

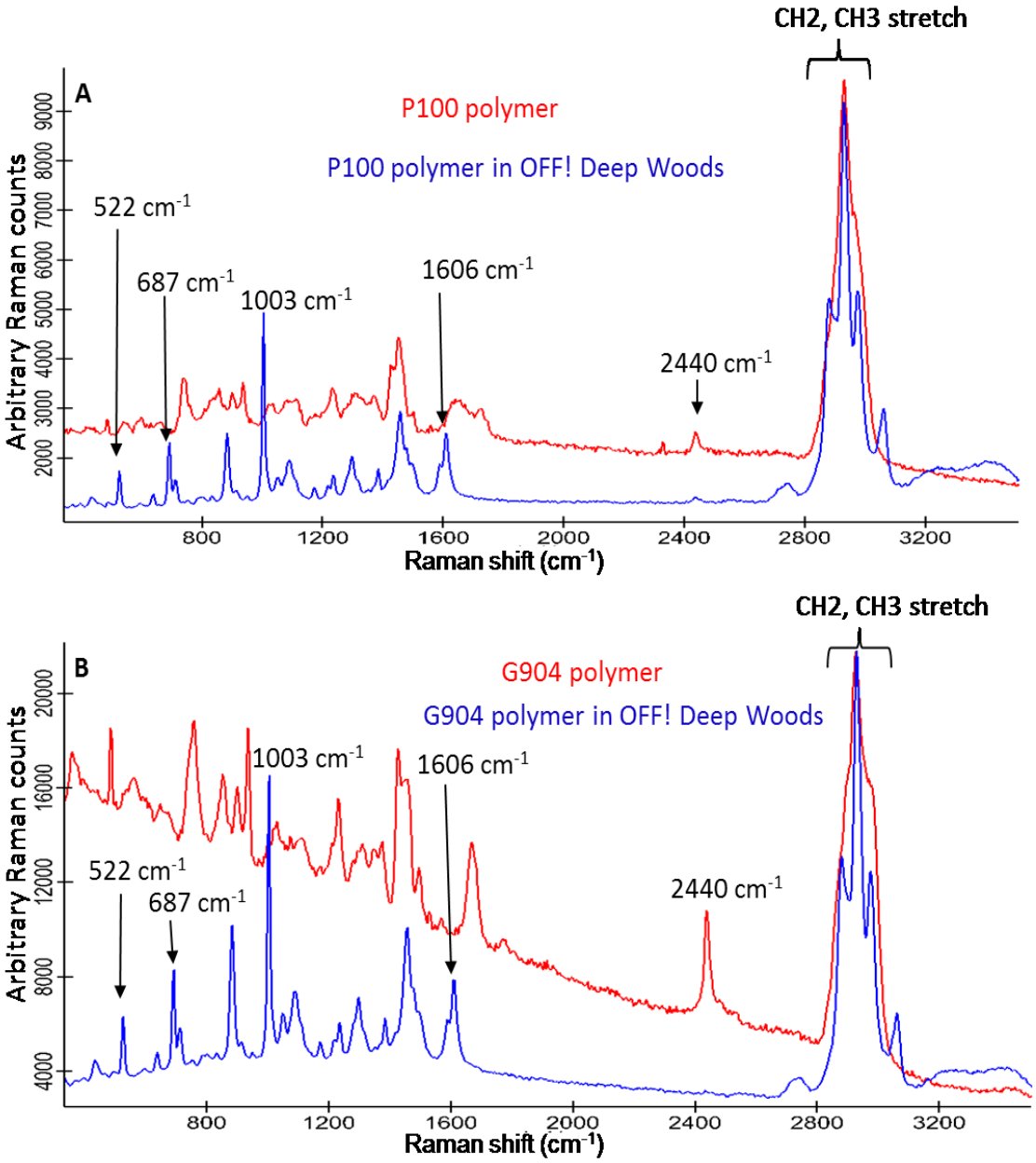

Figure 5-7. (A) Raman Spectra of P-100 polymer (red) and 1% (w/w) P-100 polymer in OFF! Deep Woods (blue). (B) Raman Spectra of G904 polymer (red) and 1% (w/w) G904 polymer in OFF! Deep Woods (blue).

Each mixture was then applied to the SC following the same procedures described previously in this chapter. Figure 5-8 shows the image generated for the various marker bands when the film forming polymer S2000 was incorporated into the OFF! product. Images were generated after application and at 2hrs. and 4 hrs. after treatment and incubation. The images show that a small quantity of DEET can be detected on or near the SC surface for the samples that were not incubated and that DEET penetrated slightly into the SC following 2 hrs. of incubation. The samples incubated for 2 hrs. seem to contain a higher amount of DEET than the those incubated for 4 hrs. Less DEET is shown penetrating in Fig. 5-8A-B (polymer) vs. Fig. 5-2B and C (no polymer). No DEET was observed on or close to the surface for the samples incubated for 4 hrs. This could be because the S2000 polymer formed a film on the surface of the SC preventing any available DEET on the surface from continuously penetrating while the initial DEET that has penetrated is dispersed within the SC so its concentration is below our detection limit.

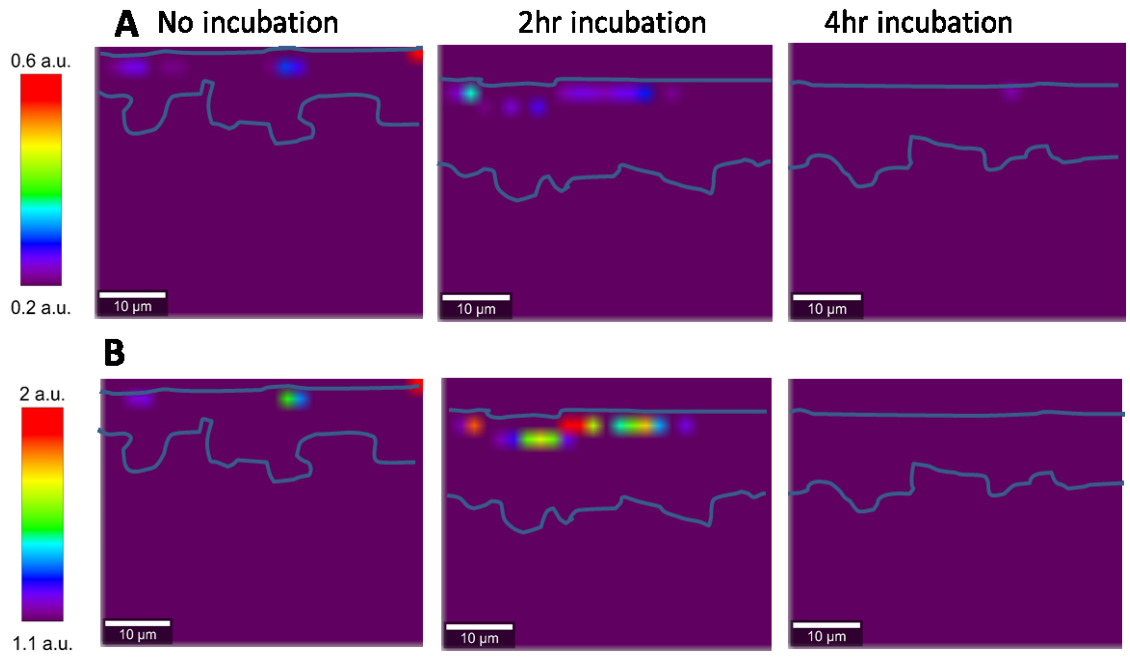

Figure 5-8. Confocal Raman image showing the effect of a film forming polymer, S2000, on the intensity of DEET distribution in skin samples incubated over time using the various marker bands. The upper and lower SC boundaries are outlined. Images (left to right) for treated SC with no incubation and at 2 hrs. and 4 hrs. after incubation (A) 522 cm^{-1} /Amide I intensity; (B) 687 cm^{-1}/Amide I intensity.

Several other polymers were evaluated in the OFF! products for their effects on the spreading of DEET. Figures 5-9 show the images generated for the intensity of the ratios of the 522 cm^{-1}/Amide I and the 687 cm^{-1}/Amide I, respectively, when the film-forming polymer G904 was incorporated into the OFF! product. Images were generated after application and at 2hrs. and 4 hrs. after

treatment. The images show that DEET can be detected close to the SC surface for the sample that was not incubated and DEET penetrated down into the SC for approximately 4 μm for the sample incubated 2 hr. and down to about 10 μm for the 4hr. incubation. The location of DEET in the images for the different marker bands showed good correlation with each other.

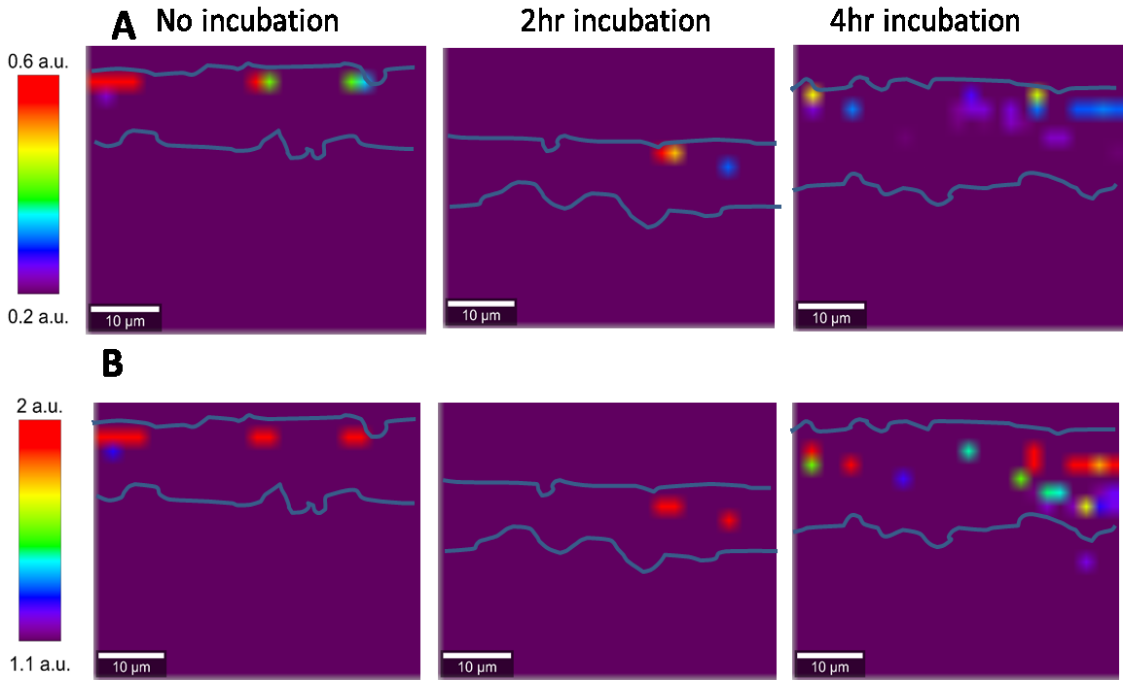

Figure 5-9. Confocal Raman image showing the effect of a film-forming polymer, G904, on the intensity of DEET distribution in skin samples incubated over time using the various marker bands. The upper and lower SC boundaries are outlined. Images (left to right) for treated SC with no incubation and at 2 hrs. and

4 hrs. after incubation (A) 522 cm^{-1}/Amide I intensity; (B) 687 cm^{-1}/Amide I intensity.

Figure 5-10 shows the images generated when the film-forming polymers P-100 and ES425 were incorporated into the OFF! product. Images were generated after application with no incubation. Results indicate that DEET can be detected on or near the SC surface for the P-100 polymer. This is similar to the finding for the S2000 and G904 film-forming polymers; however, the distribution of DEET is more homogeneous for the P-100 polymer. The image showed an increased concentration of DEET that is distributed uniformly on the SC surface (top 6-8 microns) for the P-100 polymer when compared to the S2000 and G904 polymers. This is quite interesting because the OFF! product gelled upon the addition of P-100 polymer. Therefore, changing the rheology of the product also changes the spreading behavior and as a result DEET is distributed more evenly on the SC which can give better protection. On the flip side, most dramatic changes occur by adding the ES425 polymer to OFF! product. DEET is found to permeate throughout the imaged area indicating that the ES 425 polymer is functioning as a permeation enhancer.

The results from this study provide an important method for analyzing how DEET permeates into the SC. The addition of polymers to the OFF! product also gives us insight on how the different polymers interact with the SC and the effect of polymer on permeation of DEET. This information can be used to design polymers for specific application such as to prevent DEET from penetrating the

SC or to keep DEET on the surface of the SC longer to increase the efficacy of insect repellent.

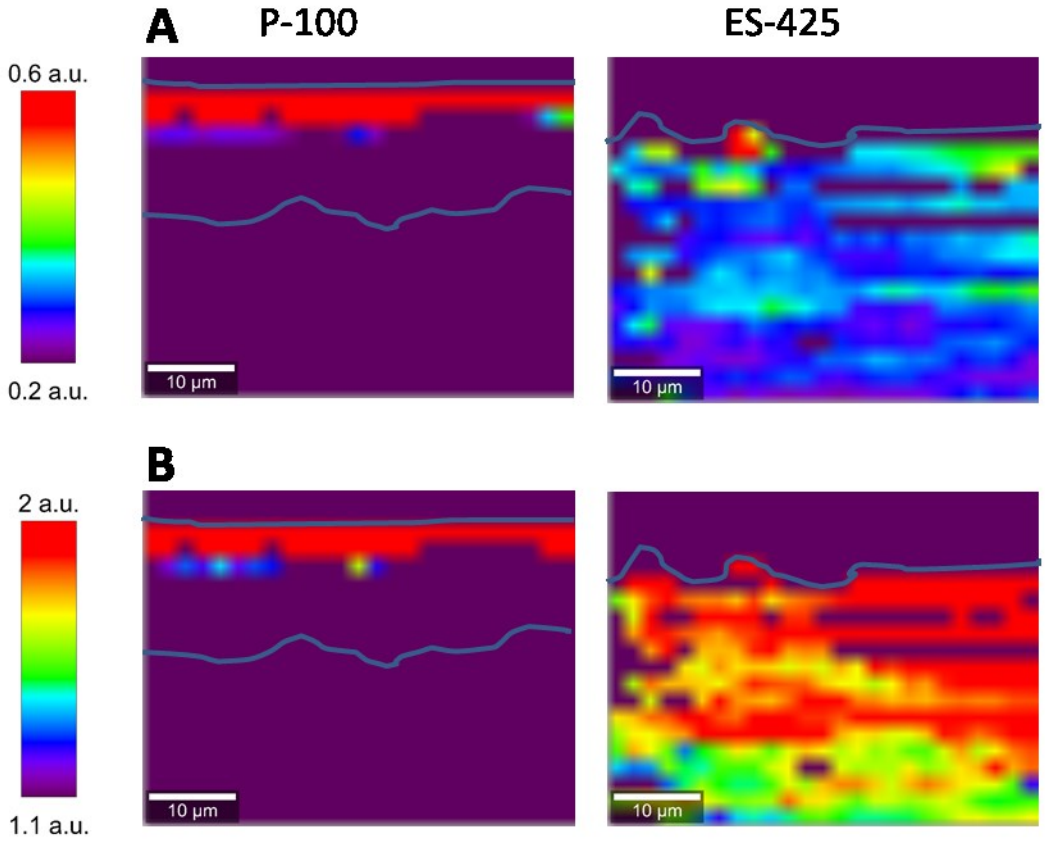

Figure 5-10. Confocal Raman image of the intensity of DEET distribution in skin when the P-100 and ES-425 polymers were each added to the OFF! product and applied to SC. Images were generated with no incubation time (A) Images for 522 cm^{-1}/Amide I band; (B) Images using 687 cm^{-1}/Amide I band.

5.4 Conclusion

In the current chapter, confocal Raman microscopy was used for the first time (to our knowledge) to provide an understanding concerning the penetration properties of DEET, the active ingredient in the insect repellent OFF!, when applied to the SC. We also used the same method to investigate the effect of polymers on the penetration process. The results from this study confirmed that DEET does penetrate into the SC. Results from the samples incubated for 2 hr. and 4 hr. indicate that DEET was detected down to about 6-8 μm. Addition of polymers to the OFF! product also gives us insight as to the effect of various polymers on permeation of DEET. Results showed that the film-forming polymer S2000 prevented DEET from penetrating into the SC after the polymeric film is formed on the SC. On the other hand, the ES-425 polymer dramatically enhanced the penetration of DEET. Information such as this can be used to design polymers for specific applications such as to prevent or slow the penetration of DEET or to have DEET persist on the surface of the SC longer to increase the efficacy of the insect repellent.

5.5 References V

1. Katz, T. M.; Miller, J. H.; Hebert, A. A., Insect repellents: Historical perspectives and new developments. *Journal of the American Academy of Dermatology* **2008,** *58* (5), 865-871.
2. Qiu, H.; McCall, J. W.; Won Jun, H., Formulation of topical insect repellent N,N-diethyl-m-toluamide (DEET): vehicle effects on DEET in vitro skin permeation. *International Journal of Pharmaceutics* **1998,** *163* (1–2), 167-176.
3. Leal, W. S., The enigmatic reception of DEET — the gold standard of insect repellents. *Current Opinion in Insect Science* **2014,** *6*, 93-98.
4. Santhanam, A.; Miller, M. A.; Kasting, G. B., Absorption and evaporation of N,N-diethyl-m-toluamide from human skin in vitro. *Toxicology and Applied Pharmacology* **2005,** *204* (1), 81-90.
5. Groen, D.; Poole, D. S.; Gooris, G. S.; Bouwstra, J. A., Is an orthorhombic lateral packing and a proper lamellar organization important for the skin barrier function? *Biochimica et biophysica acta* **2011,** *1808* (6), 1529-37.
6. Rawlings, A. V.; Harding, C. R., Moisturization and skin barrier function. *Dermatologic therapy* **2004,** *17 Suppl 1*, 43-8.
7. Forslind, B.; Engstrom, S.; Engblom, J.; Norlen, L., A novel approach to the understanding of human skin barrier function. *J Dermatol Sci* **1997,** *14* (2), 115-25.
8. Baroni, A.; Buommino, E.; De Gregorio, V.; Ruocco, E.; Ruocco, V.; Wolf, R., Structure and function of the epidermis related to barrier properties. *Clinics in dermatology* **2012,** *30* (3), 257-62.
9. Thakoersing, V. S.; Gooris, G. S.; Mulder, A.; Rietveld, M.; El Ghalbzouri, A.; Bouwstra, J. A., Unraveling barrier properties of three different in-house human skin equivalents. *Tissue engineering. Part C, Methods* **2012,** *18* (1), 1-11.
10. Proksch, E.; Brandner, J. M.; Jensen, J. M., The skin: an indispensable barrier. *Experimental dermatology* **2008,** *17* (12), 1063-72.
11. Elias, P. M., Structure and function of the stratum corneum permeability barrier. *Drug Dev. Res.* **1988,** *13* (2-3), 97-105.
12. Southwell, D.; Barry, B. W.; Woodford, R., Variations in permeability of human skin within and between specimens. *International Journal of Pharmaceutics* **1984,** *18* (3), 299-309.
13. Hawkins, G. S.; Reifenrath, W. G., Development of an in vitro model for determining the fate of chemicals applied to skin. *Fundamental and Applied Toxicology* **1984,** *4* (2), S133-S144.
14. Kasting, G. B.; Bhatt, V. D.; Speaker, T. J., Microencapsulation decreases the skin absorption of N,N-diethyl-m-toluamide (DEET). *Toxicology in Vitro* **2008,** *22* (2), 548-552.
15. Kaushik, D.; Costache, A.; Michniak-Kohn, B., Percutaneous penetration modifiers and formulation effects. *International Journal of Pharmaceutics* **2010,** *386* (1–2), 42-51.
16. Michniak, B. B.; Player, M. R.; Chapman, J. M., Jr.; Sowell, S. J. W., Azone analogs as penetration enhancers: effect of different vehicles on hydrocortisone acetate skin permeation and retention. *J. Controlled Release* **1994,** *32* (2), 147-54.
17. Pyatski, Y.; Zhang, Q.; Mendelsohn, R.; Flach, C. R., Effects of permeation enhancers on flufenamic acid delivery in Ex vivo human skin by confocal Raman microscopy. *International Journal of Pharmaceutics* **2016,** *505* (1–2), 319-328.
18. Pudney, P. D. A.; Melot, M.; Caspers, P. J.; Van Der Pol, A.; Puppels, G. J., An in vivo confocal Raman study of the delivery of Trans-retinol to the skin. *Appl. Spectrosc.* **2007,** *61* (8), 804-811.

19. Pot, L. M.; Coenraads, P. J.; Blomeke, B.; Puppels, G. J.; Caspers, P. J., Real-time detection of p-phenylenediamine penetration into human skin by in vivo Raman spectroscopy. *Contact Dermatitis* **2016,** *74* (3), 152-158.
20. Caspers, P. J.; Bruining, H. A.; Puppels, G. J.; Lucassen, G. W.; Carter, E. A., In Vivo Confocal Raman Microspectroscopy of the Skin: Noninvasive Determination of Molecular Concentration Profiles. *Journal of Investigative Dermatology* **2001,** *116* (3), 434-442.
21. Nakagawa, N.; Matsumoto, M.; Sakai, S., In vivo measurement of the water content in the dermis by confocal Raman spectroscopy. *Skin research and technology : official journal of International Society for Bioengineering and the Skin (ISBS) [and] International Society for Digital Imaging of Skin (ISDIS) [and] International Society for Skin Imaging (ISSI)* **2010,** *16* (2), 137-41.
22. Klossek, A.; Thierbach, S.; Rancan, F.; Vogt, A.; Blume-Peytavi, U.; Rühl, E., Studies for improved understanding of lipid distributions in human skin by combining stimulated and spontaneous Raman microscopy. *European Journal of Pharmaceutics and Biopharmaceutics* **2017,** *116*, 76-84.
23. Elias, P. M., Structure and Function of the Stratum Corneum Extracellular Matrix. *Journal of Investigative Dermatology* **2012,** *132* (9), 2131-2133.
24. Mélot, M.; Pudney, P. D. A.; Williamson, A.-M.; Caspers, P. J.; Van Der Pol, A.; Puppels, G. J., Studying the effectiveness of penetration enhancers to deliver retinol through the stratum cornum by in vivo confocal Raman spectroscopy. *Journal of Controlled Release* **2009,** *138* (1), 32-39.
25. Zurdo Schroeder, I.; Franke, P.; Schaefer, U. F.; Lehr, C.-M., Development and characterization of film forming polymeric solutions for skin drug delivery. *European Journal of Pharmaceutics and Biopharmaceutics* **2007,** *65* (1), 111-121.
26. Garvie-Cook, H.; Frederiksen, K.; Petersson, K.; Guy, R. H.; Gordeev, S., Characterization of Topical Film-Forming Systems Using Atomic Force Microscopy and Raman Microspectroscopy. *Mol. Pharmaceutics* **2015,** *12* (3), 751-757.
27. Kathe, K.; Kathpalia, H., Film forming systems for topical and transdermal drug delivery. *Asian Journal of Pharmaceutical Sciences* **2017**.
28. Felton, L. A.; Porter, S. C., An update on pharmaceutical film coating for drug delivery. *Expert Opin. Drug Delivery* **2013,** *10* (4), 421-435.
29. Maitra, P.; Brahms, J., Challenges in Cosmetic Formulations: Appearance, Long Wear, and Comfort. *MRS Bulletin* **2011,** *32* (10), 787-792.
30. Prettypaul, D.; Fares, H., Microscopic evaluation of polymeric film properties of anhydrous sunscreen compositions and their relation to absorption and water resistance. *J. Cosmet. Sci.* **2012,** *63* (3), 213-221.
31. Li, F.; Men, Z.; Li, S.; Wang, S.; Li, Z.; Sun, C., Study of hydrogen bonding in ethanol-water binary solutions by Raman spectroscopy. *Spectrochim. Acta, Part A* **2018,** *189*, 621-624.
32. Sivakesava, S.; Irudayaraj, J.; Demirci, A., Monitoring a bioprocess for ethanol production using FT-MIR and FT-Raman spectroscopy. *J. Ind. Microbiol. Biotechnol.* **2001,** *26* (4), 185-190.
33. Barry, B. W.; Edwards, H. G. M.; Williams, A. C., Fourier transfer Raman and infrared vibrational study of human skin: assignment of spectral bands. *J. Raman Spectrosc.* **1992,** *23* (11), 641-5.
34. Flach, C. R.; Moore, D. J., Infrared and Raman imaging spectroscopy of ex vivo skin. *International Journal of Cosmetic Science* **2013,** *35* (2), 125-135.

35. Choe, C.; Lademann, J.; Darvin, M. E., Lipid organization and stratum corneum thickness determined in vivo in human skin analyzing lipid-keratin peak (2820-3030 cm-1) using confocal Raman microscopy. *J. Raman Spectrosc.* **2016,** *47* (11), 1327-1331.
36. Janssens, M.; van Smeden, J.; Puppels, G. J.; Lavrijsen, A. P. M.; Caspers, P. J.; Bouwstra, J. A., Lipid to protein ratio plays an important role in the skin barrier function in patients with atopic eczema. *Br. J. Dermatol.* **2014,** *170* (6), 1248-1255.